SOLAR ABSORPTION SPECTROSCOPY AT THE DALHOUSIE ATMOSPHERIC OBSERVATORY

by

Jonathan E. Franklin

Submitted in partial fulfillment of the
requirements for the degree of
Doctor of Philosophy

at

Dalhousie University
Halifax, Nova Scotia
November 2015

Table of Contents

List of Figures

Abstract

A newly refurbished high-resolution Fourier Transform Spectrometer (FTS) has been installed at the Dalhousie Atmospheric Observatory (DAO) to monitor the outflow of trace gases leaving North America. Regular solar absorption measurements began in June 2011 and trace gas concentrations are determined from the observed spectra via an optimal estimation technique using the standard SFIT4 software package. Significant software development was required to match the FTS output to the software and it was also necessary to tailor the ancillary data inputs to the instrument and location.

The development of a custom-built open-source high-accuracy solar tracker to support the FTS is described. The Community Solar Tracker (CST) can be remotely operated and runs autonomously with a tracking accuracy < 10 arcseconds. Versions of the CST are now operating successfully at a variety of different locations including a high-Arctic research station near Eureka, Nunavut. The high accuracy and comprehensive monitoring possible with this tracker has revealed previously undetected alignment issues with the FTS-tracker combination, but solutions to these issues have been found and are being implemented.

In July 2011, the DAO participated in the Quantifying the impact of **BOR**eal forest fires on **T**ropospheric oxidants over the Atlantic using **A**ircraft and **S**atellites (BORTAS) campaign, and detected biomass burning plumes originating from central Canada. This campaign also involved the Portable Atmospheric Research Interferometric Spectrometer (PARIS), a lower-resolution FTS instrument, which provided a means to validate our trace gas columns. Total column CO differences were $< 4\%$ during the extended BORTAS campaign and a significant pollution plume detected in August 2011 is analysed to show the impact of precipitation history on plume composition.

Finally, three years of measurements of CO, C_2H_6, and CH_4 are presented and analyzed showing the expected seasonal trends, as well as an additional summertime enhancements in CO and C_2H_6 caused by seasonal wildfire emissions being transported across North America and out over the Atlantic Ocean.

List of Abbreviations Used

AEROCAN	Canadian aerosol robotic network
AERONET	Aerosol robotic network
AIRS	Atmospheric infrared sounder
AMF	Airmass factor
AMS	Aerosol mass spectrometer
AOD	Aerosol optical depth
ARCTAS	Arctic research of the composition of the troposphere from aircraft and satellites
BC	Black carbon
BORTAS	Quantifying the impact of boreal forest fires on tropospheric oxidants using aircraft and satellites
CST	Community solar tracker
DAO	Dalhousie atmospheric observatory
DAQ	Data acquisition device
DGS	Dalhousie ground station
DOAS	Differential optical absorption spectroscopy
DOFS	Degrees of freedom for signal
DRL	Dalhousie raman lidar
FAAM	Facility for airborne atmospheric measurements
FIRMS	Fire information for resource management system
FOV	Field of view
FTS	Fourier transform spectrometer
FWHM	Full width at half maximum

GBS	Ground based spectrometer
GDAS	Global data assimilation system
GEOS-Chem	Goddard earth observing system chemical transport model
HITRAN	High-resolution transmission molecular absorption database
HYSPLIT	Hybrid single-particle lagrangian integrated trajectory model
IGM	Interferogram
ILS	Instrument line shape
IRWG	Infrared working group
LN2	Liquid nitrogen
LOS	Line of sight
LRT	Long range transport
MCT	Mercury cadmium telluride
MIR	Mid-infrared
MODIS	Moderate resolution infrared spectrometer
MOPITT	Measurements of pollution in the troposphere
NCEP	National centers for environmental prediction
ND	Neutral density
NDACC	Network for the detection of atmospheric composition change
NIR	Near-infrared
OEM	Optimal estimation method

OPD	Optical path difference
PARIS	Portable atmospheric research interferometric spectrometer
PBL	Planetary boundary layer
PEARL	Polar environment atmospheric research laboratory
ppbv	Parts per billion by volume
SDA	Spectral deconvolution algorithm
SNR	Signal to noise ratio
SZA	Solar zenieth angle
TAO	Toronto atmospheric observatory
TCCON	Total carbon column observing network
TCP	Transmission control protocol
UTC	Coordinated universal time
UV	Ultraviolet
VMR	Volume mixing ratio
WACCM	Whole atmosphere climate chemistry model
ZPD	Zero path difference

Acknowledgements

Over the course of this project I have been privileged to receive the support of many friends and colleagues, some of whom I would like to name here.

I would like to especially thank Jim Drummond who has guided me through this degree and supported me as I faced the many challenges of instrumentation work. Many thanks are due to his entire research group who have collectively encouraged me along the way: Alexey Tikhomirov for his expertise in fixing every piece of equipment that I managed to break; Yan Tsehtik for his help maintaining my entire data set; Stacy Wise for her work upgrading the DAO-DA8 and for training me in its operation; and Lisa LeBlanc and Olga Summers for shielding me from so much of the administrative work required in research.

I would also like to thank Glen Lesins and Thomas Duck for their insights and suggestions during my committee meetings over the years, as well as Rachel Chang and Ian Folkins for their support during my defence.

I was fortunate to have a series of summer and co-op students with whom I could share the burden of regular observations: Kevin Curry, Marc Cormier, and Thomas Baltzer collectively saved me many hours of sleep with their devotion to our measurements.

I would also like to thank my second family of researchers at the University of Toronto. A special thank you goes to Kimberly Strong who has supported me both financially and via her enthusiasm. Without the help of Joseph Mendonca, Stephanie Conway, Debora Griffin, Felicia Kolonjari, Cynthia Whaley, and Camille Viatte I would likely still be struggling to perform my first trace gas retrievals. I have also had the support of the PEARL staff: Pierre Fogal, Mike Maurice, and Peter McGovern.

Financial support for this work was provided by Dalhousie University, Canadian Space Agency, NSERC CREATE, Innovation Nova Scotia, and the Canadian Foundation for Innovation.

Finally, I thank my parents and my sister who have both pushed me to succeed and comforted me when things did not always progress as fast as I wished.

Chapter 1

Introduction

Awareness of the negative effects of airborne pollutants has been steadily growing over the past few decades, and as a global community we are beginning to recognize our atmosphere as the shared resource that it truly is. Many countries are actively investing significant efforts into the development of new policies aimed at limiting the release of harmful compounds into the atmosphere, but the success of any regulatory action is critically dependent on our ability to accurately quantify and assess the emission, transport, and chemical evolution of these pollutants.

Some emissions are not directly anthropogenic in nature. The 2015 wildfire season in North America has been a brutal reminder of the power of natural processes. Increasing temperatures in the western USA and Canada have significantly strained the natural cycles of the forests and recent population explosions of beetles have killed vast stretches of the forest. This dead wood provides the raw fuel for ravaging fires that are often sparked by lightning [1]. Some researchers have also implicated improvements in fire suppression techniques for the stronger blazes in recent years. In the past, regular fires helped to control the build up of tinder on the forest floors. Without this natural regulation, fires that elude initial suppression can quickly grow in size and strength [2]. Emissions from the largest fires can easily escape the local boundary layer of the atmosphere and be transported long distances.

The introduction in the 1970s of satellite-based remote-sensing of the atmosphere quickly demonstrated the truly global nature of pollution transport. Identifiable emissions are often observed thousands of kilometers away from their source [3]. Adding to the complexity of the problem, it has been shown that pollution plumes "age" chemically, and that the newly formed or secondary compounds can have very different effects than that of their precursors [4].

While satellite measurements are able to provide a global view of some of these processes, the interpretation of the signals is difficult and can be attended by

biases that are hard to predict or quantify using solely satellite data. Therefore, ground-based validation of satellite measurements is a critical task within the atmospheric science community. As the satellite instrumentation continues to age in the harsh environment of space, and old instruments are replaced by new with perhaps different biases, this validation work will continue to be an active area of research.

Global transport models (such as GEOS-Chem) can aid in our interpretation of satellite observations, and are continually evolving into more sophisticated analysis and forecasting tools. However, their accuracy is also critically dependent on having spatially and time resolved observations of chemical abundances that can be used as model constraints. In addition, small scale pollution plumes from individual power plants or smaller boreal forest fires often can not be resolved by satellite measurements or global models, and local "point" measurements are still required.

With this in mind, we set out to commission a new ground-based observing platform in Halifax, Nova Scotia, at the Dalhousie Atmospheric Observatory (DAO). This thesis details the physical instrumentation, the development of the data processing pipeline, and presents initial results from the first three years of measurements.

Ground-based solar absorption spectroscopy is a very cost effective means of monitoring the composition of the earth's atmosphere, and this thesis begins in Ch. 2 with a general discussion of the method. I discuss how it can be used to study both long term or seasonal trends of important atmospheric gases as well as detect the passage of smaller plumes associated with specific emission events.

In Ch. 3 I introduce the primary instrument used at the DAO: a high-resolution Fourier Transform Spectrometer. Included is a mathematical description of Fourier Transform Spectroscopy. Electronic upgrades to the spectrometer had largely been implemented when I arrived at Dalhousie and so my focus was aimed at the development of the data processing pipeline that takes the raw measurements and transforms them into solar absorption spectra.

Accurate solar absorption measurements require precise solar tracking, and so in Ch. 4 I discuss the design of a new open-source solar tracking platform. This highly accurate and precise tool was initially conceived at the University of Toronto, and was

more fully developed here at Dalhousie University. The flexible design of the tracker and its supporting code have led to its use in a variety of different laboratories to date, and it appears to be gaining acceptance within the community.

First light of the DAO spectrometer coincided with an international campaign to study the transport and chemical evolution of forest fire plumes as they leave North America and enter the maritime air of the north Atlantic. In Ch. 5 I present our ground based measurements made in support of the primary aircraft campaign, and discuss the detection of a plume that had experienced a precipitation scavenging event while being transported towards Halifax.

I then present in Ch. 6 measurements from the first three years of observations at the DAO. The results show that we are successfully capturing the expected seasonal cycles of our target species, as well as detecting the passage of individual plumes.

Finally, in Ch. 7 I summarize the major results of this work and discuss some additional projects that should be pursued in the future.

Chapter 2

Background

In this chapter I briefly review our present understanding of the composition of our atmosphere with a focus on trace gas species related to biomass burning events that will be discussed in greater detail in later chapters. I also present solar absorption spectroscopy as a method of monitoring atmospheric composition. I conclude with an introduction to the Optimal Estimation Method used to derive the trace gas concentrations from the solar spectra.

2.1 Atmospheric Composition

Many trace atmospheric gases, despite constituting less than 1% of the Earth's atmosphere, play a major role in the global radiative balance, and have a direct effect on ground level air quality. This disproportionate influence is the result of two primary effects: their increased chemical-reactivity, and their enhanced ability to absorb and scatter electromagnetic radiation.

The term *atmospheric pollution* is often loosely defined, but generally refers to increased levels of any trace gas to the point of measurable negative effects on humans and the greater ecosystem. At one time it was believed that air pollution was merely a local problem specific to urban centers; however, it is now well understood that stable airborne pollutants (e.g., CH_4, N_2O, & CO) reaching the free troposphere are capable of travelling great distances from their sources [e.g., 3]. Satellite measurements (such as shown in Fig. 2.1) help us to monitor and quantify this transport, and the impacts of trace gases far from their sources is an active area of research.

Trace atmospheric constituents are generally separated into *primary* versus *secondary* pollutants: primary pollutants are those substances that are mainly emitted directly into the atmosphere (e.g., CO, NO_x, & SO_2), while secondary pollutants are usually formed later by chemical processes occurring within an airmass (e.g., O_3, & H_2SO_4). A distinction is also made between *aerosols* (or particulate

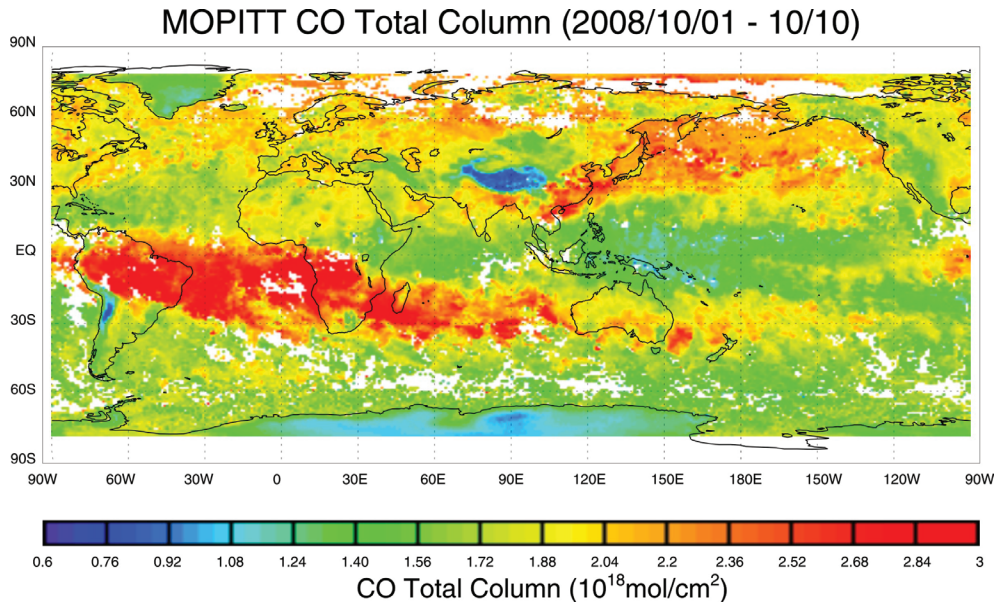

Figure 2.1: Global carbon monoxide (CO) map derived from the Measurements of Pollution in the Troposphere (MOPITT) instrument aboard the Terra Spacecraft in October of 2008. Emissions from southern hemisphere biomass burning events are shown to be transported significant distances from their sources. Smaller plumes are evident in the northern hemisphere downwind of large population regions.

matter) and *gaseous* compounds. Seinfeld and Pandis [5] define aerosols as "any substance, except pure water, that exists as a liquid or solid in the atmosphere under normal conditions and is of microscopic or submicroscopic size but larger than molecular dimensions." Aerosols are further classified by size and composition, with a common distinction made between *fine* and *coarse* mode particles. This distinction is made on the basis of diameter from in-situ measurements: greater than 2.5 μm being considered coarse, and smaller considered fine. However, when sensed remotely, a spectral approach is used which is less specific about the particle diameter [6].

While this work primarily focuses on the detection and comprehension of specific gaseous compounds, it is impossible to ignore the influence of aerosols, and many primary sources of trace gases also emit particles into the atmosphere. I will focus on three primary carbon-containing molecules: Carbon Monoxide (CO) and the two simplest alkanes, Methane (CH_4) and Ethane (C_2H_6). In Chapters 5 and 6 I will also discuss the fine mode particles associated with biomass burning events.

2.1.1 Seasonal cycles of trace gases

The global distribution of trace gases depends not only on the source strengths and locations, but also on the details of how the gases are subsequently transported through, and eventually removed from, the atmosphere. In addition, a critical parameter is the expected survival time of any given molecule before being removed via reaction with another species or by being dynamically deposited back to the surface. This is commonly referred to as the "lifetime" of a species. All three of the species I will be focusing on have both natural and anthropogenic sources, and are removed primarily through oxidation by the hydroxyl radical, OH. The importance of OH as an oxidizer is important enough to warrant a brief discussion of its production in the troposphere.

OH is primarily produced in the troposphere via the photolysis of ozone, O_3, by solar UV radiation:

$$O_3 + h\nu \rightarrow O_2 + O, \quad \lambda < 320\,\mathrm{nm} \tag{2.1}$$

If the resulting oxygen atom is released in its ground state it will quickly combine with O_2 to reform ozone; however, if released in its excited singlet state, it may react with a water molecule to produce two OH radicals:

$$O(^1D) + H_2O \rightarrow 2\,OH. \tag{2.2}$$

Globally, mean OH concentrations are $\sim 10^6$ molecules cm^{-3}, but concentrations vary widely in response to local perturbations to the sources and sinks. As a highly reactive species, OH has a lifetime on the order of seconds, and the availability of UV photons combined with this short lifetime drives significant seasonal and diurnal cycles in concentrations [5].

Methane

Methane (CH_4) is a powerful greenhouse gas whose concentration has dramatically risen since pre-industrial times. Measurements from ice cores reveal dry air mixing ratios of roughly 700 parts per billion by volume (ppbv) prior to increases of anthropogenic sources, while current day global averages range from 1750 ppbv in the southern hemisphere, to 1850 ppbv in the northern [7–9]. Figure 2.2 gives a

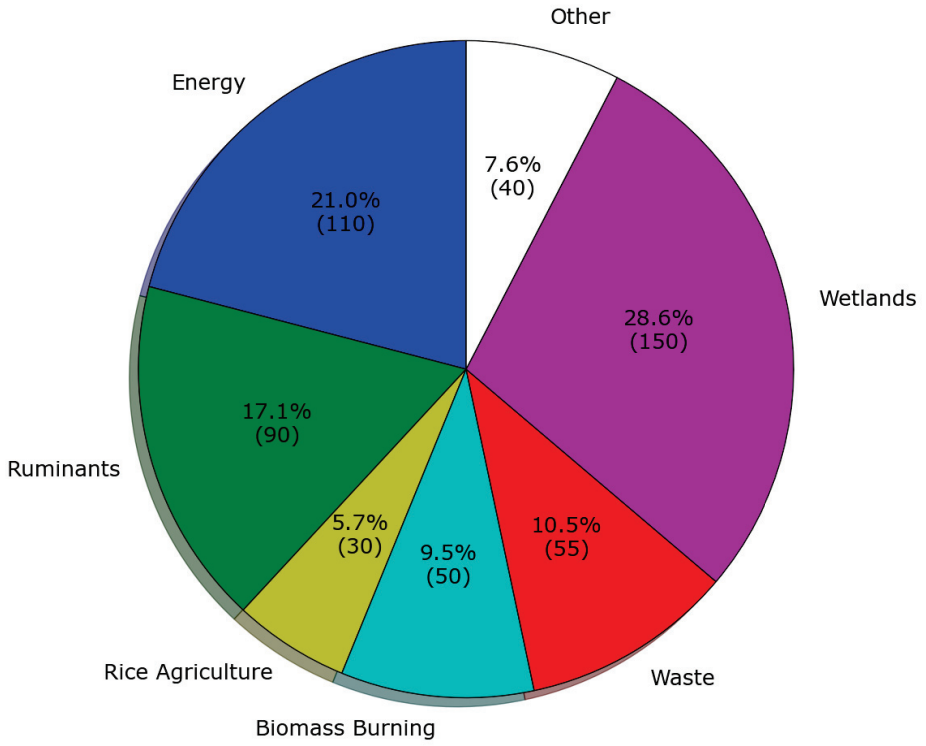

Figure 2.2: Present day sources of CH_4 emissions from [8]. (Values) represent emissions in Tg yr^{-1}.

break down of the most important sources of CH_4. Natural sources are dominated by emissions from wetlands, while anthropogenic sources include the raising of livestock, cultivation of rice, and losses during the extraction and processing of natural gas as an energy source [5]. There is significant uncertainty in how the natural emissions of CH_4 will change in a warming climate as, for example, large regions of the Arctic permafrost begin to thaw [8, 10].

In the troposphere, CH_4 has a mean lifetime of about 9 years and thus the species is relatively well mixed in the atmosphere and exhibits only a small seasonal trend driven primarily by seasonal changes in wetlands emissions [8, 11]

The most common removal mechanism of CH_4 is oxidation by OH followed by a relatively rapid series of subsequent reactions. The initial oxidation by OH produces

a methyl peroxy radical:

$$CH_4 + OH \overset{O_2}{\rightarrow} CH_3O_2 + H_2O, \tag{2.3}$$

which can follow multiple paths via NO or HO_2 to form formaldehyde (HCHO). With a lifetime measured in hours, HCHO is further broken down to CO either by photolysis:

$$HCHO + h\nu \overset{2\,O_2}{\rightarrow} 2\,HO_2 + CO, \tag{2.4}$$

or via another hydroxyl radical:

$$HCHO + OH \overset{O_2}{\rightarrow} HO_2 + CO + H_2O. \tag{2.5}$$

This oxidation of CH_4 is a primary source of CO in our atmosphere as discussed below.

Ethane

After CH_4, the next most abundant hydrocarbon is ethane (C_2H_6). Anthropogenic activity is responsible for the majority of C_2H_6 emissions, mostly through losses during the extraction of natural gas. As this activity is primarily located in the northern hemisphere, we observe a strong latitudinal dependency in the observed mixing ratios. Northern hemisphere values average 1.4 ppbv and decline to 0.3 ppbv in the southern hemisphere [12]. Incomplete combustion during biomass burning is also an important seasonal source of C_2H_6 (see Fig. 2.3)[13, 14]. The primary sink of C_2H_6 is also OH which once again leads to the production of CO, although the pathway is more complex than that of CH_4. With a lifetime that is shorter than CH_4 (on the order of two months) ethane is somewhat easier to trace back to individual sources [5].

The shorter lifetime also results in a pronounced seasonal cycle driven by the availability of OH. During the local winter, concentrations rise as the production of OH by Eq. 2.1 slows, and a maximum C_2H_6 concentration is seen in late winter before increased sunlight once again speeds the chemical loss mechanism. Average amplitudes of this seasonal cycle are also hemisphere-dependant, reaching as high as 800 pptv in some northern locations, and as low as 40 pptv in the south [12].

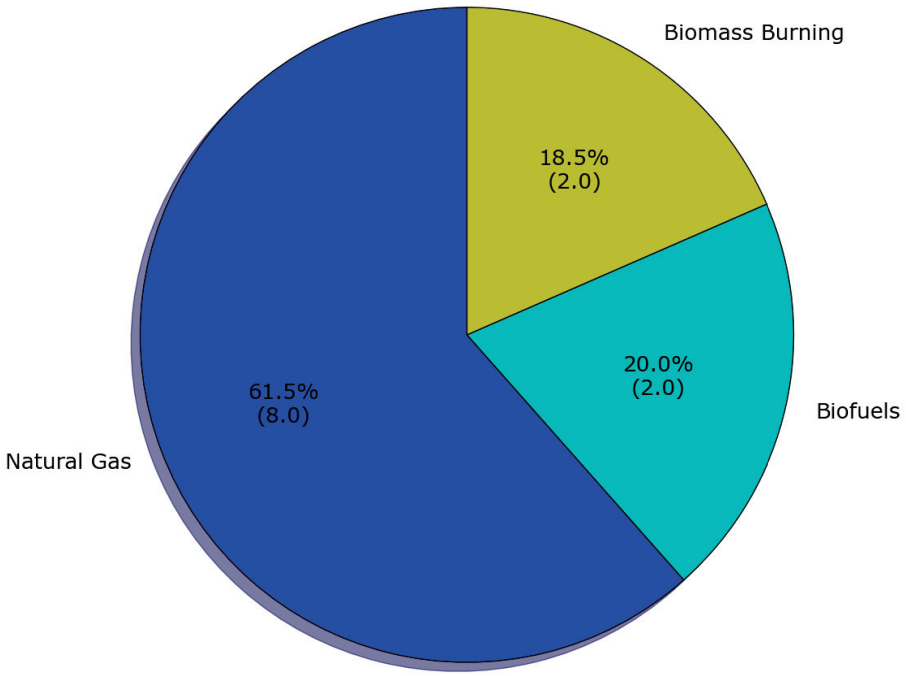

Figure 2.3: Present day sources of C_2H_6 emissions from [13]. (Values) represent emissions in Tg yr^{-1}.

Carbon Monoxide

Both methane and ethane eventually oxidize to form carbon monoxide (CO), and this process, along with the oxidation of other organic species, is responsible for roughly half of the total source of CO in our atmosphere. The remainder is the result of direct emission mostly from incomplete burning both of fossil fuels and biomass material (Fig. 2.4). Once again, present day background concentrations are higher in the northern hemisphere (∼200 ppbv) than in the southern hemisphere (∼60 ppbv), but with a chemical lifetime on the order of two months, significant plumes of CO are easily observed downwind of biomass burning events and regions of heavy industry.

As with the previous two species, the primary sink is via oxidation by OH, and this drives a strong seasonal cycle in the northern hemisphere, with variations on the order of 40% of the mean [5]. The reaction with OH forms carbon dioxide (CO_2), as

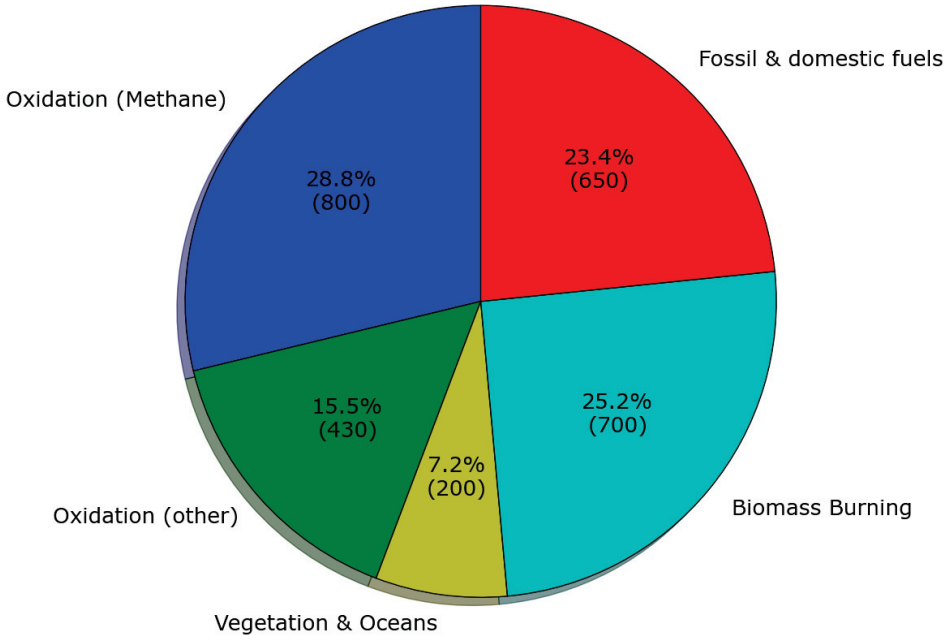

Figure 2.4: Present day sources of CO emissions from [15]. (Values) represent emissions in Tg yr^{-1}.

well as a hydroperoxyl radical:

$$CO + OH \xrightarrow{O_2} CO_2 + HO_2. \tag{2.6}$$

In the next section I demonstrate that the production of the hydroperoxyl radical plays a role in the production of tropospheric ozone.

2.1.2 Influence of biomass burning events

Biomass burning events are an important source of atmospheric pollutants around the globe, and are also a major perturbation to the northern hemisphere seasonal cycles discussed above. The primary emissions from the burning of biomass include CO, CO_2, NO_x (nitrogen oxides), CH_4 and C_2H_6, as well as aerosols such as black carbon [16]. Every year between June and October there are intense human-initiated biomass burning events in southern Africa and Brazil which have profound impacts on the regional air quality[17, 18] (See Fig. 2.1). Comparatively smaller burning events

in the northern boreal forests of Canada and Russia are largely responsible for the biomass burning traces seen in mid-northern latitudes [19, 20], and have even been implicated in intercontinental transport of pollutants [21–23].

In the presence of NO_x, the oxidation of the carbon-containing compounds can lead to significant enhancements of tropospheric ozone. Ozone in the troposphere is considered to be a pollutant as it can lead to respiratory issues in humans, and cause damage to crops.

To understand the production of tropospheric ozone we must first discuss the natural NO_x cycle. The photolysis of NO_2 produces an O_3 molecule via the reactions:

$$NO_2 + h\nu \rightarrow NO + O, \quad \lambda < 420\,\text{nm} \tag{2.7}$$

$$O + O_2 + M \rightarrow O_3 + M, \tag{2.8}$$

where M stands for some other molecule that can carry away excess energy from the second reaction. In most cases the ozone molecule quickly reacts with another NO molecule to regenerate NO_2

$$NO + O_3 \rightarrow NO_2 + O_2, \tag{2.9}$$

resulting in no net gain of ozone. This cycle occurs on the order of minutes which has led to the standard practice of referring to the total abundance of NO + NO_2 as NO_x. However, as shown above, the oxidation of CO and C_2H_6 results in the production of HO_2. These molecules can react with NO by

$$HO_2 + NO \rightarrow NO_2 + OH, \tag{2.10}$$

effectively regenerating the NO_2 without the destruction of the ozone molecule. Thus, the production of O_3 is equal to the rate of this final reaction [5]. Ozone is naturally found in the troposphere at concentrations of roughly 10 ppbv, but in a biomass burning plume where these reactions have occurred concentrations 6 or 7 times higher than this have been observed[22]. These elevated levels can be subsequently advected great distances as the lifetime of ozone is on the order of a month.

However, the expected enhancement in O_3 has not always been observed in the presence of biomass burning [24, 25]. During the Quantifying the impact of **BOR**eal forest fires on **T**ropospheric oxidants over the Atlantic using **A**ircraft and **S**atellites

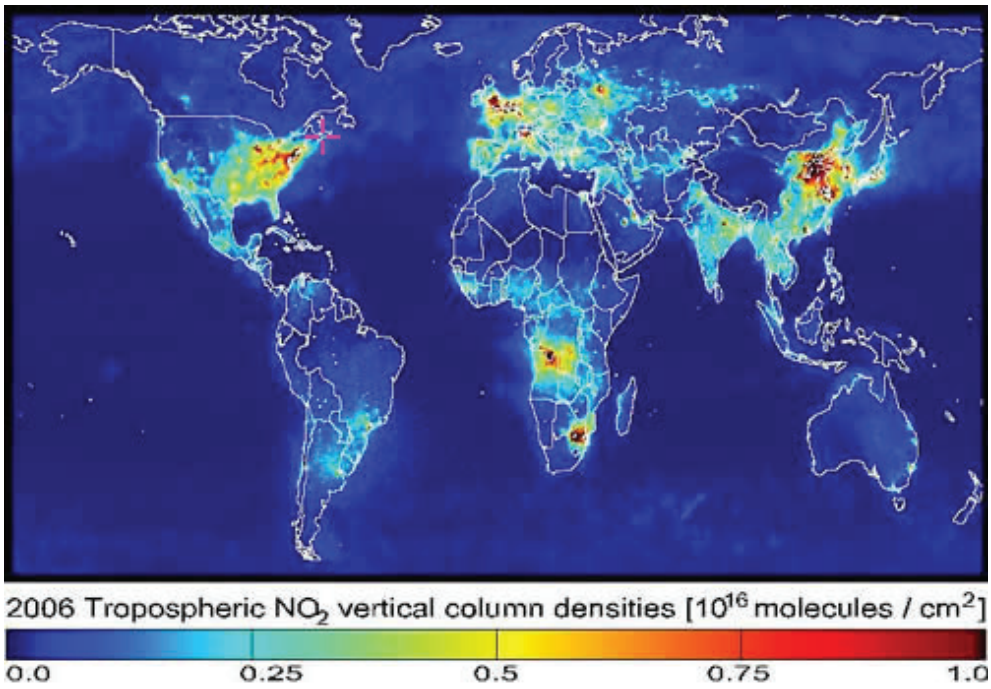

Figure 2.5: Global map of average NO_2 emissions derived from the Ozone Monitoring Instrument aboard the satellite Aura. Halifax, marked by the cross on the eastern seaboard of North America, is situated directly downwind from a large source of industrial pollution.

(BORTAS) mission of 2011, Palmer et al. [26] used a combination of aircraft, ground, and satellite measurements to try to better understand the ozone production and loss within biomass burning outflows. In Ch. 5 I will present some of the ground based measurements made from Halifax during the BORTAS campaign.

2.2 Dynamics around Halifax, Nova Scotia

Halifax, Nova Scotia, is an excellent location from which to monitor trace gas transport. Perched on the eastern edge of the continent, Halifax's maritime environment is dominated by the mid-latitude westerly winds, and the surface temperatures are moderated by the proximity to the Atlantic ocean.

The city is almost directly downwind of the major pollution plume produced by the industrial complex in the northeast of North America, as well as the seasonal biomass burning plumes from the yearly wildfires that ravage the boreal forests of northwestern Canada, and increasingly, the drought-stricken western United States.

For this reason, the region has sometimes been unkindly dubbed the "tailpipe of North America" (Fig. 2.5).

Operating atmospheric instrumentation from Halifax is not without its challenges. Baroclinic waves are often fully developed into extratropical cyclones carrying significant precipitation by the time they reach the city. From 1981 to 2010, Halifax experienced an average of 161 days with precipitation each year, with a total water equivalent of 147 cm (Environment Canada, http://climate.weather.gc.ca/). Winter storms are frequent, and often test the coverings protecting sensitive atmospheric equipment.

However, the local sources of pollution are not abundant and are relatively minor in scale. Emissions are seen from local traffic and from the shipping ports located on both ends of the city [27], but the small scale of the local industry removes much of the ambiguity between locally produced pollution and higher altitude plumes advected in from distant sources. This enables us to properly characterize the elevated plumes from events on the continent to the west of the city.

2.3 Introduction to Solar Absorption Spectroscopy

Trace gases and aerosols can be measured in-situ with appropriate equipment, but such measurements only provide ground level results on very small spatial scales. By installing in-situ sensors aboard an airplane or balloon it is possible to overcome this limitation, but the expense of such missions often requires balancing the increase in spatial resolution with a significant decrease in temporal resolution. These limited-duration campaigns can only provide a "snapshot" of the entire time series.

Ground-based solar absorption spectroscopy provides a means of balancing this equation. Information from the entire atmospheric column along the sight-line of the sun can be measured, but the cost is low enough to allow regular observations for long periods up to several decades. However, the data in this thesis only pertains to the initial few years of observations from Halifax.

Being able to remotely sense the entire atmospheric column is especially important as acute pollution events advected across North America towards Nova Scotia are also often transported vertically via large scale frontal systems, or through localized convective motions. Such plumes are often completely undetected by ground-based

in-situ measurements. Also, concentrations directly measured by surface instruments are often very sensitive to the daily rise and fall of the planetary boundary layer (PBL). Column measurements are far less sensitive to the PBL and provide a more accurate comparison to emission inventories [28].

2.3.1 Radiative Transfer

We begin with a very brief review of the key concepts relating to the radiative transfer of solar photons passing through our atmosphere: The photosphere of the sun emits as an almost perfect blackbody of ∼5780 K. However, spectroscopic measurements of the sun made from the Earth's surface reveal that a substantial amount of energy has been lost at specific optical frequencies. This modification of the blackbody spectrum contains information regarding the composition our atmosphere.

The trace gases described earlier do not only interact chemically with one another, but also with the incident sunlight, and complete photodissociation such as required in reaction 2.1 above is not the only means of interaction. Photons carrying less energy are still capable of being absorbed and scattered out of our line of sight, and it is this process that interests us here.

All molecules exist in specific energy states based on their electron configuration, state of vibration, and current rotational mode. These energy states are specified by quantum mechanical underpinnings and transitions only occur between states (and therefore at specific energies.) In the mid-infrared (MIR), photons carry energies comparable to molecular vibrational transitions, and these absorption features dominate the MIR spectrum. However, most vibrational transitions also include simultaneous less-energetic rotational transitions which causes the primary absorption line to be split up into a series of many lines both above and below the expected frequency depending on the initial rotation state and direction of the rotational transition.

This description is somewhat simplistic as it would suggest that all absorption features would be effectively delta functions at the specific frequencies that precisely correspond to the magnitude of the energy transitions. Uncertainty principle effects will provide some spread in the frequencies involved, but in reality, we observe absorption features that are significantly broadened beyond this minor effect. This

broadening is caused by two primary affects: Doppler broadening and Pressure broadening.

Doppler broadening is the simpler of the two to understand, and is the result of the thermal motions of the trace gas molecules along our line of sight to the solar disc. Such molecular motion produces a Doppler shift that allows photons of frequencies slightly lower or higher than that corresponding to a specific energy transition to still be absorbed. This effect exists at all levels of the atmosphere, and is the primary broadening above the stratosphere.

In the case of local thermodynamic equilibrium, the distribution function of molecule velocity is given by a Maxwell-Boltzmann distribution, and the line shape function caused by Doppler broadening around the expected central frequency ν_o can also described by a Gaussian equation [29]:

$$f_D(\nu - \nu_o) = \frac{1}{\alpha_D\sqrt{\pi}}\exp\left[-\frac{(\nu-\nu_o)^2}{\alpha_D^2}\right], \tag{2.11}$$

where

$$\alpha_D = v_o\sqrt{\frac{2k_BT}{mc^2}}. \tag{2.12}$$

In eq. 2.12, m is the mass of an individual molecule, T is the temperature of the gas, c is the speed of light, and k_B is the Boltzmann constant.

Pressure has an even greater broadening effect on the line shape, but as the density of Earth's atmosphere falls off exponentially, the effect is strongly a function of altitude. Collisions between molecules become frequent as one enters the lower atmosphere, and this interference with the photon scattering process causes the absorption features to be "smeared" as energy is redistributed from the central frequency out to the "wings" of the line.

Empirically the broadening observed is semi-adequately described by a Lorentz profile:

$$f_L(\nu - \nu_o) = \frac{\alpha_L/\pi}{(\nu-\nu_o)^2 + \alpha_L^2}, \tag{2.13}$$

where

$$\alpha_L = \alpha_o\left(\frac{p}{p_o}\right)\left(\frac{T_o}{T}\right)^n \tag{2.14}$$

with appropriate values for α_o and n determined empirically in a lab operating at pressure p_o and temperature T_o.

Except in the lowest portions of the atmosphere, the Lorentz profile is often insufficient to properly fit observed absorption features without also including the influence of the Doppler broadening discussed above. The combined line shape, known a Voigt profile, shares properties from both the Doppler and Lorentz broadening equations with a Gaussian center and extended wings. The Voigt profile is derived by convolving the two line shapes [29]:

$$\begin{aligned} f(\nu - \nu_o) &= f_L * f_D \\ &= \frac{1}{\pi^{3/2}} \frac{\alpha_L}{\alpha_D} \int_{-\infty}^{+\infty} \frac{1}{(\nu' - \nu_o)^2 + \alpha_L^2} \exp\left[\frac{-(\nu - \nu')^2}{\alpha_D^2}\right] \mathrm{d}\nu'. \end{aligned} \tag{2.15}$$

The goal of solar absorption spectroscopy is to use our understanding of these effects to identify both the species responsible for modifying the observed solar spectrum (via the absorption frequency), and to quantify their abundance (via the line strength). With enough spectral resolution, it is even possible to use the shape of the absorption line to derive information regarding the vertical distribution of the species.

2.4 Optimal Estimation Method

The process of deciphering the atmospheric state from observations of these absorption features is an example of an "inverse" problem. Rather than directly measuring the column of trace gases, we instead measure the impact of the trace gases upon the solar spectrum. A common technique used in solar absorption spectroscopy to perform this "retrieval" of the atmospheric state is the optimal estimation method [OEM; 30, 31]. While the complete mathematical basis of applying the OEM to atmospheric sounding can be found in Rodgers [31], in this section I will summarize the critical concepts and formulas required to appropriately apply the method to solar spectra. A discussion of the error characterization process can be found in Ch. 6.

The basis of OEM requires the development of a forward model, $\mathbf{F}$, that relates a set of measurements, $\mathbf{y}$, to the physical state of a system, $\mathbf{x}$. In our application of the method, $\mathbf{y}$ represents a vector of observed spectral information (usually several small micro-windows centered around solar absorption features of interest), while $\mathbf{x}$ represents the desired result, the vertical profile of trace gas concentration. The forward model then represents the radiative transfer and measurement process.

Additional model parameters that are considered known, or simply chosen to be fixed, are represented by the vector $\mathbf{b}$. These terms are related by:

$$\mathbf{y} = \mathbf{F}(\mathbf{x}, \mathbf{b}) + \varepsilon \tag{2.16}$$

where ε represents the errors associated with both the measurements and the necessary approximations made when developing the forward model. The goal is to determine the best value of $\mathbf{x}$ given the measurements $\mathbf{y}$ and an appropriate understanding of the errors.

In the presence of measurement and model errors the problem becomes ill-posed and a priori information, in the form of a reasonable first guess of the state of the system, is required to stabilize the solution. If we can linearize the forward model around this a priori state, $\mathbf{x}_a$, then we can write:

$$\mathbf{y} = \mathbf{F}(\mathbf{x}_a, \mathbf{b}) + \mathbf{K}(\mathbf{x} - \mathbf{x}_a) + \varepsilon \tag{2.17}$$

where $\mathbf{K}$ is the Jacobian matrix of the forward model defined by $\mathbf{K} = \partial\mathbf{F}(x)/\partial\mathbf{x}$ evaluated around $\mathbf{x}_a$. Typically, the forward model is not linear, but we can iterate the solution by using the retrieved state from one cycle as the a priori for the next, and repeating until the system converges on a solution.

The initial a priori is simply a guess of the true state of the system and also has an error associated with it:

$$\mathbf{x}_a = \mathbf{x} + \varepsilon_a, \tag{2.18}$$

and so our task is to weight the error in the measurement against the error in the a priori to determine the optimal solution represented by $\hat{\mathbf{x}}$. Rodgers shows that this optimal solution is given by:

$$\hat{\mathbf{x}} = \mathbf{x}_a + \mathbf{G}\mathbf{K}(\mathbf{x} - \mathbf{x}_a) \tag{2.19}$$

where $\mathbf{G}$ is the gain matrix that relates the sensitivity of the retrieval to the measurement vector:

$$\mathbf{G} = \frac{\partial\hat{\mathbf{x}}}{\partial\mathbf{y}} = (\mathbf{S}_a^{-1} + \mathbf{K}^{\mathrm{T}}\mathbf{S}_\varepsilon^{-1}\mathbf{K})^{-1}\mathbf{K}^{\mathrm{T}}\mathbf{S}_\varepsilon^{-1} \tag{2.20}$$

where $\mathbf{S}_a$ and $\mathbf{S}_\varepsilon$ represent the covariance matrices for the a priori, and spectral measurement noise respectively. The product of the Jacobian matrix, $\mathbf{K}$, with the

gain matrix, $\mathbf{G}$, is known as the averaging kernel matrix:

$$\mathbf{A} = \mathbf{GK} = \frac{\partial \hat{\mathbf{x}}}{\partial \mathbf{y}} \frac{\partial \mathbf{F}}{\partial \mathbf{x}} = \frac{\partial \hat{\mathbf{x}}}{\partial \mathbf{x}}, \tag{2.21}$$

The averaging kernel matrix describes the sensitivity of the retrieved state to the true state, and the knowledge contained within is critical when comparing measurements made by different instruments. In the ideal case, $\mathbf{A}$ is an identity matrix and the application of Eq. 2.19 will perfectly return the true state. In the other extreme, a null matrix suggests that the measurement has no sensitivity at all to the true state, and the retrieved solution is identical to the a priori information provided. In reality, the diagonal elements of $\mathbf{A}$ are often less than one, and off-diagonal elements exist, representing a smoothing of information between vertical levels. Thus, despite the retrieval of a full vertical profile of n elements, the number of independent pieces of information, d_s, known as the degrees of freedom for signal (DOFS), is often much less. Rodgers [31] shows that DOFS from a retrieval can be found by taking the trace of the averaging kernal matrix:

$$d_s = \mathrm{tr}(\mathbf{A}). \tag{2.22}$$

The value of d_s is heavily influenced by both instrumental parameters such as the spectral resolution and signal-to-noise ratio (SNR) of the measurement, as well as the choice of spectral features to fit. Barret et al. [32] demonstrated that by combining multiple spectral features of different strength it is possible to increase d_s and improve the vertical resolution of the observation.

In this thesis I present OEM results derived from a series of different software packages. The details of each implementation will be addressed in later chapters.

Chapter 3

The Dalhousie Atmospheric Observatory DA8

The primary instrument operating at the Dalhousie Atmospheric Observatory (DAO) is a high-resolution Fourier transform spectrometer built by ABB Bomem. Designated a "DA8" for its dynamical alignment system and 8 cm diameter aperture, the instrument will be referred to in this thesis as the DAO-DA8.

In this chapter I will discuss the method of Fourier transform spectroscopy, and describe the instrumentation used at the DAO. I will also detail the data-processing chain that transforms the raw measurements into the solar spectra needed for the trace gas analysis.

3.1 Introduction to Fourier Transform Spectroscopy

3.1.1 Overview and History

Interferometery has been in use since 1882 when it was first developed by Albert Abraham Michelson. Famously used in the failed Michelson-Morley attempt to detect the luminiferous aether – a medium theorized to exist to reconcile the propagation of electromagnetic radiation with other known waves – the Michelson Interferometer continues to be used to this day in a form that would be recognizable to scientists of the 19th century. In its simplest form, the interferometer consists of a beamsplitter, two reflecting mirrors, additional optics to feed a collimated beam into the system, and a detector. The entering light is amplitude split into two beams that travel different paths before returning to the beam splitter for recombination and direction to a detector. An Optical Path Difference (OPD) is introduced to one arm of the interferometer by physically moving a mirror. If the OPD is increased steadily while continually measuring the resulting signal, monochromatic light entering the system will produce a cosine wave whose properties uniquely depend on the wavelength of the light and the speed at which the OPD is varied.

The introduction of a multi-wavelength source will result in the production of a series of overlaid cosine waves whose individual amplitudes depend on the strength of the incoming signal. The resulting interference pattern of output signal amplitude versus OPD is commonly referred to as an "interferogram," or simply an "IGM." One characteristic point of all IGMs is the Zero Path Difference (ZPD) position where the scanning mirror and fixed mirrors are at equal optical distances from the beamsplitter. At the ZPD all incident radiation passes through the interferometer with full constructive interference and a large amplitude is recorded.

The application of a Fourier transform to the IGM then recovers the desired spectrum of the incident beam. This was formerly a great disincentive to the use of these spectrometers because of the complex calculations required, but high power computers have voided this limitation.

Fourier Transform Spectrometers (FTS) offer the ability to achieve high spectral resolutions over a large wavenumber range. One major advantage of these spectrometers is that the entire spectral range of interest is measured simultaneously with waves of every frequency passing through the same optical path. As long as the dominant noise source during a measurement is independent of the signal strength itself (e.g., dominated by detector noise), then time averaging of the signal would be expected to drive down the noise proportional to the square root of the integration time. Therefore, when compared to dispersive techniques using gratings or prisms where each spectral element is observed independently, the FTS is capable of quickly achieving a significantly higher signal to noise ratio. This is commonly referred to as the multiplex advantage, or the Fellgett advantage in honor of Peter Fellgett who first described it [33]. However, if the measurement is dominated by photon noise, then the Fellgett advantage is lost. In order to prevent this situation, narrow-band filters are commonly used to restrict the incoming signal.

Another advantage of the FTS is that the resolution is theoretically limited only by the maximum optical path difference between the two beams of light; however, in practice, large OPDs can lead to difficulties in maintaining an adequate alignment of the optical system.

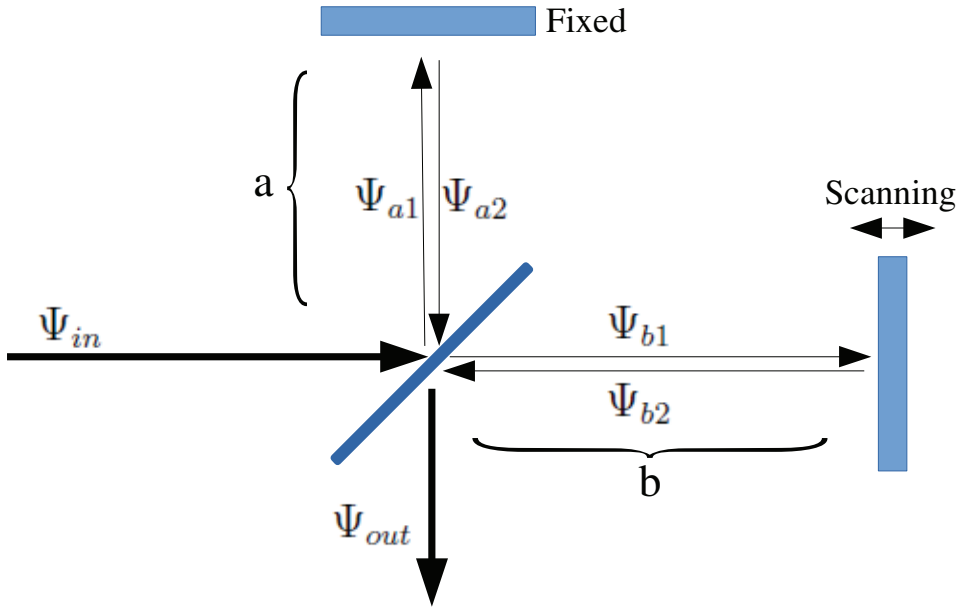

Figure 3.1: A simple schematic of a plane wave passing through a Michelson Interferometer.

3.1.2 Mathematical description

In this section I will provide a mathematical description of a plane wave passing through an ideal interferometer based upon the formulation used by Bell [34] and Chamberlain et al. [35]. A simplified schematic of the optical path is shown in Fig. 3.1.

Mathematically, a plane wave of amplitude A_o, and angular frequency ω, can be described at any time t, and position $\mathbf{x}$ in exponential form as

$$\Psi_{in} = A_o e^{i(\omega t + \mathbf{k}\cdot\mathbf{x})} \tag{3.1}$$

where $\mathbf{k}$ is the wavenumber vector given by:

$$\mathbf{k} = 2\pi\sigma\hat{k} \tag{3.2}$$

with σ representing the magnitude of the wavenumber (or the reciprocal of wavelength) in the $\hat{k}$ direction.

As this wave enters the interferometer it encounters a beamsplitter which, ideally, reflects and transmits the wave evenly. Beamsplitters are designed to minimize any phase shifts during passage, but for now we allow the possibility of a shift upon

reflection or transmission. The waves immediately following the interaction with the beamsplitter can be written as:

$$\Psi_{a1} = |r|A_o e^{i(\omega t+\phi_r)} \tag{3.3}$$

$$\Psi_{b1} = |t|A_o e^{i(\omega t+\phi_t)} \tag{3.4}$$

with the reflection and transmission coefficients ideally satisfying:

$$|r|^2 + |t|^2 = 1. \tag{3.5}$$

The initially reflected wave travels a distance a to the fixed mirror and returns to the beamsplitter, and this path length can be interpreted as a phase shift allowing us to write:

$$\Psi_{a2} = |r|A_o e^{i(\omega t+\phi_r+k2a)} \tag{3.6}$$

Likewise, the wave that was initially transmitted will travel a distance b to the scanning mirror and return to the beamsplitter as:

$$\Psi_{b2} = |t|A_o e^{i(\omega t+\phi_t+k2b)} \tag{3.7}$$

As the waves encounter the beamsplitter again, Ψ_{a2} is transmitted, Ψ_{b2} is reflected, and the final outgoing wave heading to the detector, Ψ_{out}, is the sum of the two waves:

$$\begin{aligned}\Psi_{out} &= |t|\Psi_{a2}e^{i\phi_t} + |r|\Psi_{b2}e^{i\phi_r} \\ &= |r||t|A_o e^{i(\omega t+\phi_r+\phi_t)}\left[e^{ik2a} + e^{ik2b}\right]\end{aligned} \tag{3.8}$$

For clarity I will now make the assumption that the beamsplitter was designed in such a way to assure that

$$\phi_r = \phi_t = 0. \tag{3.9}$$

Eq. 3.8 can then be rearranged using $2a = (b+a) - (b-a)$ and $2b = (b+a) + (b-a)$ to find

$$\Psi_{out} = |r||t|A_o e^{i\omega t}e^{ik(b+a)}\left[e^{ik(b-a)} + e^{-ik(b-a)}\right] \tag{3.10}$$

or

$$\Psi_{out} = |r||t|A_o e^{i\omega t}e^{ik(b+a)}[2\cos(k(b-a))]. \tag{3.11}$$

The detector measures the intensity of this wave which is related by the complex modulus squared:

$$\begin{aligned} I_{out} &= TRA_o^2 4\cos^2(k(b-a)) \\ &= TRA_o^2 2\left[1+\cos(2k(b-a))\right]. \end{aligned} \tag{3.12}$$

The OPD between the two beams is given by $x = 2(b-a)$ so as a final step we can combine our constants to reveal the measured IGM as:

$$I_{out} = I_o\left[1+\cos(kx)\right]. \tag{3.13}$$

Note that the final result consists of two parts: a constant signal overlaid with a cosine term that is a function of OPD. Although the steady term does not include any spectral information, it can be used to detect and even compensate for any slow variations in the strength of the source signal during a measurement [36].

This derivation was based on a single monochromatic plane wave of amplitude A_o, but can be easily expanded to include a broadband source, $B(\sigma)$. Replacing our wavenumber vector, $\mathbf{k}$, using Eq. 3.2, the modulated portion of the IGM can be written as:

$$I(x) = \int_{-\infty}^{+\infty} B(\sigma)\cos(2\pi\sigma x)\mathrm{d}\sigma. \tag{3.14}$$

This idealized IGM is symmetric about the ZPD position, continues out to infinity in both directions, and consists of a superposition of many waves. This allows us to recover the spectrum from Eq. 3.14 by simply performing a cosine Fourier transform:

$$B(\sigma) = \int_{-\infty}^{+\infty} I(x)\cos(2\pi\sigma x)\mathrm{d}x. \tag{3.15}$$

Of course, it is a universal truth that things become more complicated in reality, and we must next consider a variety of issues that prevent us from directly applying Eq. 3.15.

3.1.3 Moving beyond the ideal FTS

The first physical constraint we must account for is the reality that only a finite portion of the IGM can be measured in the laboratory. We can most easily account for this by multiplying our IGM, $I(x)$, in Eq. 3.15 by a "box-car" function, $f(x)$,

which has a value of 1 over the range of OPDs that are measured, and 0 elsewhere:

$$f(x) = \begin{cases} 1 & \text{when } 0 \leq x \leq \mathrm{L}, \\ 0 & \text{when } x < 0, x > \mathrm{L}. \end{cases} \tag{3.16}$$

The measured spectrum, $B'(\sigma)$, can now be defined using the convolution theorem which states that the Fourier transform of the product of two functions is equivalent to the convolution of the Fourier transforms of each function:

$$B'(\sigma) = \int_{-\infty}^{+\infty} I(x) f(x) \cos(2\pi\sigma x) \mathrm{d}x = B(\sigma) * F(\sigma), \tag{3.17}$$

where $F(\sigma)$ is the Fourier transform of $f(x)$. In our present case of the box-car function, $F(\sigma)$ is given by the sinc function:

$$F(\sigma) = 2\mathrm{L}\,\mathrm{sinc}\,(2\pi\sigma\mathrm{L}) \equiv \frac{2\mathrm{L}\sin(2\pi\sigma\mathrm{L})}{2\pi\sigma\mathrm{L}}. \tag{3.18}$$

As this sinc function is convolved with the true spectrum the result is to further broaden the absorption features while simultaneously adding undesirable oscillations to the spectrum. These oscillations can be lessened by choosing alternative truncation functions, but at the cost of widening the central burst of $F(\sigma)$. The full width at half maximum (FWHM) of the central burst becomes the effective resolution of the FTS, and is inversely proportional to the maximum OPD. For our box-car function, the FWHM is 0.6/L. This allows us to design a sampling strategy based on the spectral resolution requirements of the project. To achieve high-resolution spectra in a practical instrument it is common to exploit the symmetry of the ideal IGM and measure only one side relative to the ZPD, with the result known as a "single-sided" IGM. However, as I will show in §3.4.2, it is critical that even single-sided IGMs still sample at least a small portion of the signal beyond the ZPD.

Another physical constraint that must be considered is the effect of an extended source. In §3.1.2 we assumed that the light beam passing through the interferometer was perfectly collimated, but any true FTS has a finite entrance aperture that allows divergent rays to pass. Figure 3.2 shows the geometry of such a divergent ray entering the FTS. An on-axis ray would gain an OPD of twice the relative separation of the two mirrors, but a ray entering at an angle α will have a smaller OPD given by $x\cos(\alpha)$.

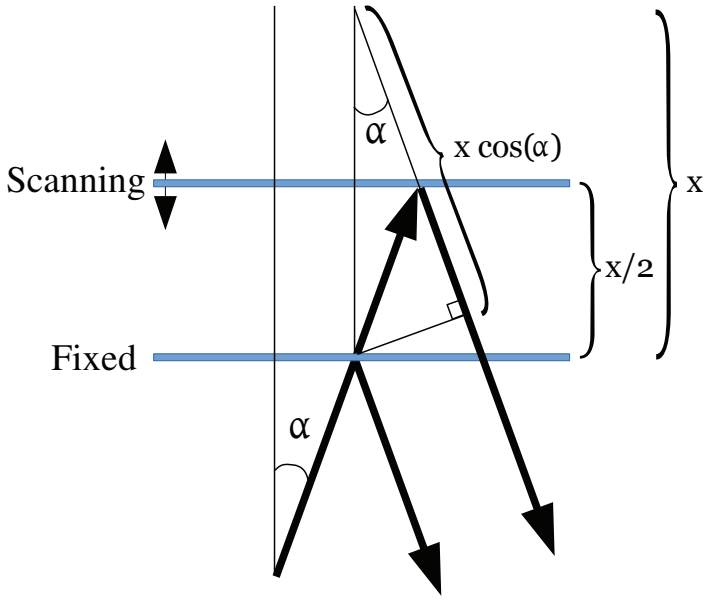

Figure 3.2: Ray diagram showing the shortening of the OPD for a divergent off-axis ray. While an on-axis ray will experience an OPD of x, a ray divergent by α only travels a distance of $x\cos(\alpha)$ before recombination.

The use of an iris at the FTS input allows us to limit α to values sufficient to allow the use of the small angle approximation:

$$x_{eff} = x\cos(\alpha) \sim x\left(1 - \frac{\alpha^2}{2}\right) = x\left(1 - \frac{\Omega}{2\pi}\right), \tag{3.19}$$

where Ω is the solid angle of the field-of-view (FOV) given by $\Omega = \pi\alpha^2$. This effective OPD must be included in Eq. 3.17 and has the effect of further broadening spectral features. As rays will enter the FTS at a variety of angles from zero to α, we must integrate over this range of solid angles:

$$\begin{aligned} B'(\sigma) &= \int_{-\infty}^{+\infty} I(x) \int_0^{\Omega_m} \cos\left[2\pi\sigma x\left(1 - \frac{\Omega}{2\pi}\right)\right] \mathrm{d}\Omega\mathrm{d}x. \\ &= \int_{-\infty}^{+\infty} I(x)\pi\Omega_m \mathrm{sinc}\left(\frac{\sigma x\Omega_m}{2\pi}\right) \cos\left(2\pi\sigma x\left(1 - \frac{\Omega_m}{4\pi}\right)\right) \mathrm{d}x. \end{aligned} \tag{3.20}$$

The cosine term will transform to a delta function which shifts energy to lower wavenumbers, while the sinc term becomes a box-car function of width $\sigma\Omega_m/2\pi$. This additional broadening and the wavenumber shift are the two major effects of an extended FOV [34].

Finally, we assumed in Eq. 3.9 that there was no net phase shift produced by interacting with the beamsplitter. Even if this is true, wavenumber dependant phase shifts may still be introduced by other optical components, or the electronic filters commonly used within the detector pre-amplifiers. This acts to transfer some of the spectral signal into the imaginary plane upon application of a full Fourier transform to the IGM. The measured spectrum, $B'(\sigma)$ is now given by

$$B'(\sigma) = \int_{-\infty}^{+\infty} I(x) e^{-i2\pi\sigma x} \mathrm{d}x, \tag{3.21}$$

where the measured spectrum is related to the true spectrum by:

$$B'(\sigma) = B(\sigma) e^{-i\phi(\sigma)}. \tag{3.22}$$

In §3.4.2 I will describe a method to quantify and correct for these phase errors.

3.2 Description of the DAO-DA8

3.2.1 History of the DAO-DA8

The DAO-DA8 is owned by the Canadian Space Agency, and in 2008 was loaned to Dalhousie University where it underwent an upgrade before beginning regular solar absorption measurements in 2011. The upgrade was nearly complete when I arrived in the fall of 2009 to join Dr. Stacy Wise, a post-doctoral researcher leading the electronic upgrade. I was directly involved in completing the final installation of the DAO-DA8 and alignment of its internal optics, and independently developed the data processing stream described below that derives the solar spectra from the raw measurements.

The first goal of the project was to demonstrate that with a proper electronic upgrade, and when paired with a extremely accurate custom built solar tracker (discussed in detail in Ch. 4), it is possible to use the DA8 for research-grade remote-sensing of the atmosphere. The second goal was to begin making daily solar absorption measurements to monitor the composition of the atmosphere above Halifax, characterize the seasonal cycles of trace gases, and to identify the sources of specific pollution plumes observed.

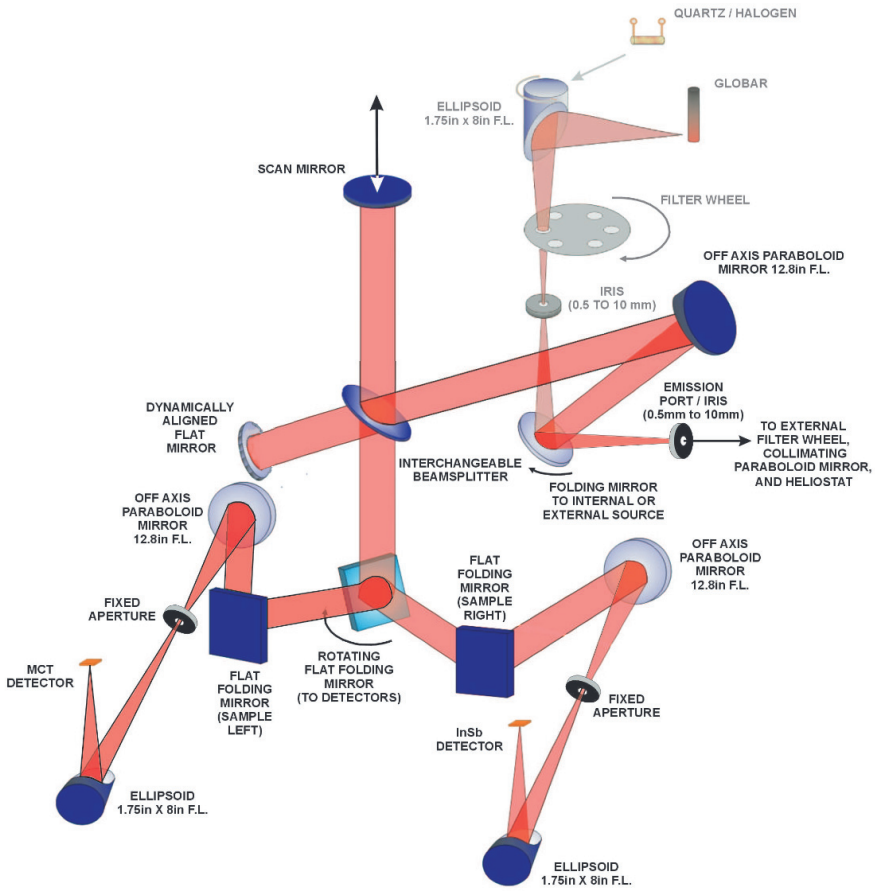

Figure 3.3: Schematic of the DAO-DA8 showing the optical path

3.2.2 Physical description of the DAO-DA8

The DAO-DA8 is capable of reaching a maximum resolution of $\sim$0.004 cm^{-1} by producing single-sided IGMs with a maximum OPD of 250 cm. The scanning mirror must travel 125 cm vertically to produce this OPD, which requires precise alignment of the optical system (Fig. 3.3). Newer FTS systems often employ corner cube reflectors on the scanning mirror which will nullify any mirror tilt during a scan. In contrast, the older DAO-DA8 uses a simple flat mirror, and any undesired mirror motions will impact the optical path of the beam.

To help minimize this unavoidable tilting of the scanning mirror as it moves, a Helium-Neon (HeNe) laser operating at 632.8 nm is also passed through the heart of the DAO-DA8, in effect forming 3 small interferometers at the limits of the aperture. The interference patterns of the HeNe signals as they emerge from the interferometer

are monitored throughout a scan using a series of photodiodes. This information is passed in real time to a dynamical mount which steers the fixed mirror to correct for the tilting of the scanning mirror.

The HeNe laser also provides information regarding the position of the scanning mirror. When digitizing the signal from the detector it is important to sample at equal intervals of OPD. As described in §3.1.2, a monochromatic beam (such as the HeNe laser) passing through an interferometer will produce a cosine wave output. This signal is processed to produce a series of timing pulses that are are solely a function of the scanning mirror position. This signal is then used to trigger the digital sampling.

To increase the possible spectral range of the instrument, the DAO-DA8 has two separate detector ports which currently contain InSb and HgCdTe (MCT) detectors. A computer controlled steering mirror determines which detector receives the focused output beam. The beamsplitter can also be changed depending on the spectral range of interest. We are currently equipped with KBr (450 to 5,000 cm^{-1}) and CaF_2 (1200 to 10,000 cm^{-1}) beamsplitters. As the KBr beamsplitter is hygroscopic, the DAO-DA8 is kept under vacuum whenever the KBr beamsplitter is in use.

3.2.3 The upgrade

From the beginning it was clear that the core optics of the DAO-DA8 were sound, but it was decided that new electronics should be developed to take advantage of the substantial increase in computational power since the instrument was originally built. This, in turn, required a significant effort to ensure that the new software was correctly interacting with the low level electronics, while preserving the quality of the original dynamical alignment system.

One of the changes made to the system was the installation of a new 18-bit Data Acquisition (DAQ) device to replace the 16-bit DAQ that was of insufficient resolution to sample the full dynamic range of the IGM without implementing a less than satisfactory gain switching algorithm. (Recently, Dr. Alexey Tikhomirov, a research associate in our group, has developed a 24-bit DAQ system to perform uniform time sampling of both the IR signal and the HeNe metrology laser. However, all results shown in this document were gathered before the introduction of the 24-bit

Filter	Wavenumber (cm^{-1})	Wavelength	Retrieved Species
1	4000-4300	2.3-2.5	HF, CO
2	2900-3500	2.6-3.3	H_2O, C_2H_2, HCN
3	2400-3100	3.3-4.1	O_3, HCl, N_2O, $\mathbf{CH_4}$, NO_2, $\mathbf{C_2H_6}$, H_2O, CO_2
4	2000-2700	3.9-5.0	**CO**, OCS
5	1500-2200	4.7-6.3	CO, NO, COF_2
6	750-1350	7.4-14	O_3, $ClONO_2$, HNO_3, N_2O, CH_4, C_2H_2, CFCs

Table 3.1: Spectral range of the filter set used at the DAO including a list of species often retrieved by the NDACC community. Species discussed in this work are highlighted.

system.)

New control software was written by Dr. Wise using National Instruments LabVIEW^{TM} software and it is used to both control the spectrometer, and to interact with the DAQ. The code was designed with automation in mind, and includes a full scheduling component that is capable of running a series of user defined scripts throughout a measurement day. Human interaction is only needed at the beginning and end of each observing day to perform tasks such as cooling the detectors with liquid nitrogen (LN_2) and removing protective coverings from the transfer optics. Although I was not directly involved in the initial writing of this software, I have made a number of improvements to the code including general bug fixes as well as the addition of a module to control a new filter wheel.

3.3 Measurement Procedures

The DAO is currently operated as an independent station, but it is clear that our data will be of more use to the community if it is gathered following the agreed upon procedures of previously existing global FTS networks. As part of the Network for the Detection of Atmospheric Composition Change (NDACC), the InfraRed Working Group (IRWG) has developed observing strategies that are shared by all measurement stations.

In accordance with these strategies, we observe the solar spectrum through a series of narrow-band filters. Table 3.1 lists the 6 filters, their wavenumber ranges,

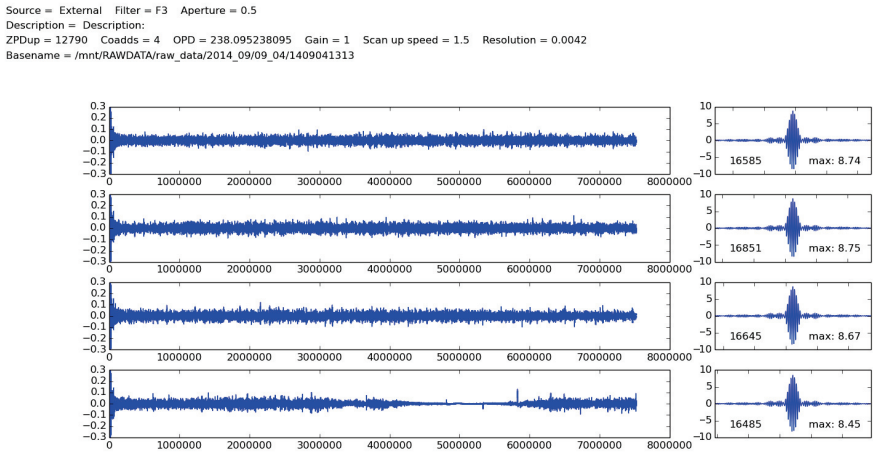

Figure 3.4: Example summary image of raw data gathered by the DAO-DA8. The temporary drop in signal in the fourth scan was caused by the passage of a cloud.

and the trace gases that are typically retrieved by the NDACC community from each. Narrow-band filters are used to preserve the Fellgett advantage discussed in §3.1 above. Highlighted in Table 3.1 are the species that will be considered in this document.

When observing through filters 1-4, four individual scans are averaged together to produce a single measurement, while six scans are averaged when observing with filters 5 and 6. The averaging increases the signal to noise ratio of the final measurement, and diminishes the effect of any temporary variations in the DC signal, but comes at the cost of decreased temporal resolution.

3.4 Data Processing

3.4.1 Data filtering

It is important to directly observe the raw data gathered by any instrument to monitor for any unexpected noise or failure. As such, all data gathered by the DAO-DA8 passes through a data processing pipeline designed to enable the user to quickly view and flag every measurement. Every measurement is summarized in a single figure that displays all 4 or 6 scans scaled to show both the shape of the ZPD region as well as the general signal level at higher OPD. In addition, header information for

the measurement is clearly displayed. These figures are created automatically as the measurements are stored. An example of such a data summary figure is shown in Fig. 3.4

After all individual measurement figures are created, a quality check code is run that displays the figures in order, and allows the operator to quickly accept or reject the measurements with single-key presses. Individual scans that show evidence of clouds (e.g., final scan of Fig. 3.4) can be rejected, thus preserving the remainder of the measurement.

3.4.2 Phase Corrections

Overview

Once the raw data has been filtered we can work towards applying a Fourier transform to produce the solar spectra. At the end of §3.1.2 I discussed a few complications that prevent us from directly applying the cosine Fourier transform of Eq. 3.15. The ideal IGM is expected to be symmetric about the ZPD position, and can be fully described using only cosine functions, but even well aligned spectrometers produce IGMs that, upon close inspection, have significant asymmetries.

One source of this asymmetry is caused by the digitization process of the analog signal from the detector. If a data sample does not perfectly match with the peak of the ZPD burst, then this will show as a phase error that is a linear function of wavenumber. More troublesome are non-linear wavenumber-dependent phase shifts that can be introduced by filters, imperfect beamsplitters, or electronic delays. The result of these phase shifts is to transfer some of the energy into the imaginary plane during the application of the Fourier transform.

For a double-sided IGM (where information is collected at OPD from $-x_{max}$ to $+x_{max}$) these phase errors can be ignored by simply taking a power spectrum of the IGM. However, this method has a non-linear effect on noise, and can not be applied to a single-sided IGM. Instead, in 1966 Michael Forman proposed a method of using a short double-sided region about the ZPD position to correct the phase errors and return a symmetric IGM that once again allows Eq. 3.15 to be applied [37].

A variety of phase correction software is available, but because of the difficulties of diagnosis of instrument and other problems with proprietary software we created

an open source version of the Forman method written in Python. In this section I will present the mathematical derivation of the Forman method while illustrating its application to a true IGM measured by the DAO-DA8.

The Forman Method

The phase correction of a single-sided IGM is only possible under the assumption that the wavenumber-dependant phase error, $\phi(\sigma)$, varies smoothly and slowly. The Forman method attempts to correct the asymmetry of the measured asymmetric IGM by convolving it with a "phase interferogram," or the Fourier transform of the phase spectrum, $e^{i\phi(\sigma)}$.

Borrowing some notation from Forman et al. [37], our measured asymmetric IGM can be written as:

$$M(x) = \int_{-\infty}^{+\infty} B(\sigma) e^{-i\phi(\sigma)} e^{-i2\pi\sigma x} \mathrm{d}\sigma, \tag{3.23}$$

and is the transform of $B'(\sigma)$ from Eq. 3.22. Computation of the phase spectrum is only possible from a double-sided IGM, and this is why even single-sided IGMs must include some values from before the ZPD. If our single sided IGM, $M(x)$, was recorded from $-x_{min}$ to $+x_{max}$ (where $|x_{min}| \ll |x_{max}|$), then we must begin the phase correction process by considering a short double-sided IGM, $M_s(x)$, that spans $-x_{min}$ to $+x_{min}$. The low-resolution (and complex) spectrum $B'_s(\sigma)$ is then given by the transform:

$$B'_s(\sigma) = \int M_s(x) e^{i2\pi\sigma x} \mathrm{d}x. \tag{3.24}$$

By Eq. 3.22 this is equal to

$$\begin{aligned} B'_s(\sigma) &= B_s(\sigma) e^{-i\phi(\sigma)} \\ &= B_s(\sigma) \left[\cos(\phi(\sigma)) - i \sin(\phi(\sigma))\right], \end{aligned} \tag{3.25}$$

and therefore:

$$\phi(\sigma) = -\arctan \frac{\Im(B'_s(\sigma))}{\Re(B'_s(\sigma))}. \tag{3.26}$$

With the phase error in hand, we can then take another Fourier transform to create the phase interferogram, $F(x)$:

$$F(x) = \int_{-\infty}^{+\infty} e^{i\phi(\sigma)} e^{-i2\pi\sigma x} \mathrm{d}\sigma. \tag{3.27}$$

This is useful, because our desired symmetric IGM, $I(x)$, can be written as:

$$\begin{aligned} I(x) &= \int_{-\infty}^{+\infty} B(\sigma) e^{-i\phi(\sigma)} e^{i\phi(\sigma)} e^{-i2\pi\sigma x} \mathrm{d}\sigma \\ &= \int_{-\infty}^{+\infty} \mathscr{F}^{-1}(M(x)) \mathscr{F}^{-1}(F(x)) e^{-i2\pi\sigma x} \mathrm{d}\sigma, \end{aligned} \tag{3.28}$$

where $\mathscr{F}^{-1}$ represents the inverse Fourier transform. The convolution theorem states that the Fourier transform of the product of two functions is equivalent to the convolution of the Fourier transforms of each function. And so our phase corrected IGM can be calculated by:

$$I(x) = M(x) * F(x). \tag{3.29}$$

As the Forman method, when applied to an asymmetric IGM, returns another IGM, it is possible to iterate the procedure if necessary. However, Forman et al. [37] recommend multiplying the phase interferogram, $F(x)$, by an apodization function, and therefore multiple iterations of the procedure will continually add small errors into the final spectrum.

Once the corrected IGM is considered sufficiently symmetric, the cosine Fourier transform of Eq. 3.15 may finally be applied to retrieve the desired spectrum.

3.4.3 Instrument Line Shape

The optical alignment of the DAO-DA8 has been seen to drift over time, and regular monitoring is essential as this drift can lead to OPD-dependent errors that will influence the measured spectra. The combined effect of a finite OPD and off-axis rays (§3.1.3) can be characterized by the Instrument Line Shape (ILS). The ILS can be thought of as the impulse response of the FTS to a delta-function input signal. If this response function is known then it can be included mathematically as a parameter of the forward model in the OEM retrieval process described in §2.4. Failure to include the ILS in the retrieval process can lead to significant systematic errors in the derived trace gas columns [38].

It is not feasible to produce a true delta-function input signal, and so typically the ILS is calculated by measuring narrow absorption features of a low-pressure gas cell placed in the optical path of the FTS. Hase et al. [38] describe the method that we use at the DAO which is also used at most NDACC observing locations. Even at low

pressures, the absorption features of the calibrating gas will be Doppler broadened, but this effect can be moderated by using a gas with a higher molecular weight (see Eq. 2.11 in §2.3.1). It is also ideal to choose a gas that does not exist in the atmosphere in observable quantities as this allows the determination of the ILS concurrently with the solar absorption measurements. A good candidate gas is HBr and significant effort has been made to properly determine the spectral line parameters needed [39].

The absorption features of the HBr (0-1) fundamental band have widths at room temperature comparable to the resolution of the DAO-DA8, and so it is necessary to use an iterative retrieval process to quantify the ILS. The forward model uses knowledge of the HBr line parameters, as well as gas temperature and pressure, to produce an ideal absorption spectrum that can be convolved with a modelled ILS based on the FOV of the FTS. The resulting synthetic spectrum is then compared to the measured spectrum, and the ILS is varied until suitable agreement is achieved. At the DAO we use the software package LINEFIT (v.12) to perform this retrieval [38]. Results from our ILS measurements will be presented in Ch. 6.

Chapter 4

The Community Solar Tracker

In this chapter I discuss the development and implementation of a new open-source solar tracker designed as a support tool for solar absorption spectroscopy measurements. The material in this chapter was submitted for publication on 14 November 2015 and has been reformatted and slightly expanded to match the flow of this dissertation.

4.1 Motivation

Accurate solar tracking is a critical component of many quantitative approaches to remote sounding of our atmosphere. The retrieval of trace gas columns from an observed solar spectrum requires precise knowledge of the instrument's line-of-sight (LOS) at the time of observation. Solar radiation observed when the sun is near the horizon will have transited a longer optical path through the atmosphere and will exhibit stronger absorption features compared to spectra gathered when the sun is overhead. This longer path length must be recreated within the forward model of §2.4. It is common to quantify this effect by referring to the effective "airmass factor" (AMF) through which the radiation has propagated. The AMF is defined as the observed atmospheric path length normalized by the path length at the zenith. Figure 4.1 uses a simple plane-parallel homogeneous-mass model of the atmosphere to show that the AMF increases as a function of solar zenith angle (SZA; z, defined as the angle between the local zenith and the visible center of the sun):

$$\text{AMF} \approx \frac{1}{\cos z}. \tag{4.1}$$

As the SZA increases, Eq. 4.1 begins to overestimate the true AMF of a non-homogeneous spherical atmosphere and a more careful analysis is required. Kasten and Young [40] used a more complex model of the atmosphere to derive a

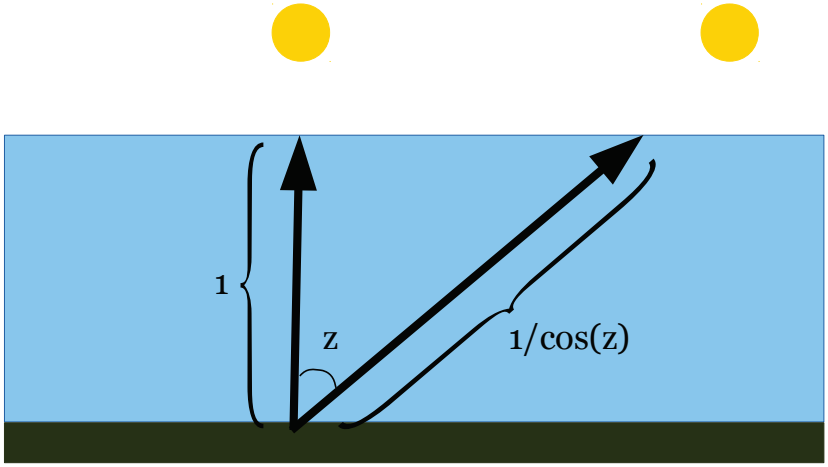

Figure 4.1: Plane-parallel model of the atmosphere showing the relative atmospheric path length increasing as $1/\cos z$. As z increases this model over predicts the true effective airmass of a non-homogeneous spherical atmosphere.

more accurate approximation given by:

$$\mathrm{AMF} \approx \frac{1}{\cos z + 0.50572(96.07995 - z)^{-1.6364}}. \tag{4.2}$$

These two functions are shown in Fig. 4.2. At high SZA the AMF curve becomes very steep, and small changes in pointing lead to large airmass differences.

Inadequate tracking can cause substantial systematic errors in the final atmospheric column values. Observing networks focused on enhancing our understanding of the global carbon cycle [e.g., TCCON; 41, 42] as well as trends in other trace gases (e.g., NDACC) are required to produce extremely accurate concentration values and recognize that limitations on the knowledge of LOS can drive the error budget of their measurements [e.g., 41]. Other instrumentation including UV and Visible spectrometers also require accurate tracking, and a reliable simple system such as the one described in this chapter will fulfill the requirements of many experiments.

Historically, solar tracking has been maintained using an "active" feedback signal provided by a quandrant-diode system. These devices seek to balance the photocurrent produced by four identical photodiodes illuminated by the solar beam [e.g., 43]. However, such devices track the center of power rather than the geometric

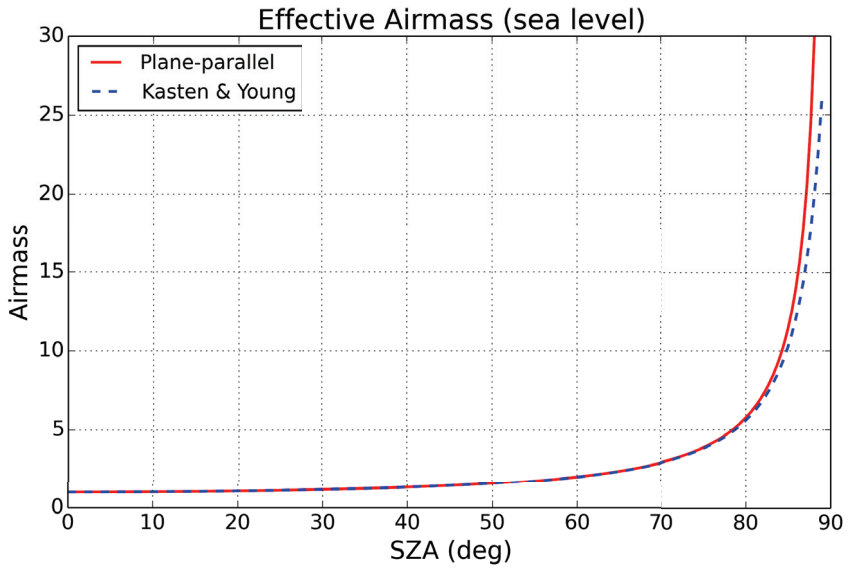

Figure 4.2: Effective airmass as a function of SZA. The plane-parallel approximation is accurate to 1% at $z < 72$ deg, but rapidly diverges at higher SZA.

center, and are thus unable to appropriately handle gradients in brightness across the solar disc that may be caused by thin clouds or aerosols. In addition, if no "passive" system of tracking exists (e.g., employing ephemeris calculations to predict the location of the sun), a temporary loss of signal due to a passing cloud often requires either user input or a time intensive search function. Purely passive systems are not affected by brightness gradients, but are prone to large systematic errors stemming from errors in the installation, drift in components, and other time-dependent effects.

To overcome such deficiencies some tracking systems now employ a camera to monitor and help correct deviations of the solar disc from its desired position. Gisi et al. [44] demonstrate such a system, the "CamTracker", and show a marked decrease in tracking errors even at high SZA. However, different laboratories often have unique requirements, and many groups continue to invest time and energy into developing custom tracking systems, resulting in a continual "reinventing of the wheel".

We attempt to break this cycle by creating the Community Solar Tracker (CST) – a simple, yet robust, accurate, and precise solar tracker that was conceived with the notion of making an open-source model that other labs can expand upon. The resulting system is cheaper to build, and significantly more flexible than commercial

options. In §4.2 we present a list of requirements for the system. In §4.3 we introduce the physical hardware and control software used in our tracker, and discuss multiple versions of the system currently operating at three locations. §4.4 presents data demonstrating the quality of our tracking. We conclude in §4.5 as we propose a method to couple the CST solar beam to a FTIR spectrometer.

4.2 Requirements

Although there are a variety of commercial products available, none meet the slew of requirements that different tracking applications may need. In hopes of easily integrating our tracking system with a variety of different measuring instruments, we aimed to realize a design which is useful and adaptable, and of low enough complexity that any reasonably-equipped laboratory could quickly construct a tracker suited to their unique situation. The design was, of necessity, driven by some of our own requirements which were roughly in order of importance:

Accuracy: The tracker is required to maintain tracking to a level where tracking error is a minimal part of the error budget of our FTIR measurements. Tracking errors typically manifest themselves as errors in determining the correct AMF to include in subsequent analyses. One of our stations is at a latitude of 80° N and routinely tracks very close to the horizon where knowledge of the AMF is critical. At 80 deg SZA a 1 deg pointing error leads to a 10 percent change in the air mass. Despite this steep AMF vs SZA we continue to strive for an accuracy that makes errors due to tracking negligible, and require a tracking precision that at more modest latitudes would be more than adequate. We desire an AMF error no greater than 0.1 percent at 80 deg SZA, and therefore must track better than ±0.01 deg (±36 arcsec).

Flexibility/Scalability: One of the exciting and sad facts of life is that equipment availability changes quickly. In addition, we recognized that there are requirements for small trackers and large trackers as some laboratories are limited by space, while others require a large enough solar beam for multiple instruments that share a single tracker. Finally, some groups may wish to retrofit existing tracking mechanisms. Thus, the design must be able to accommodate a variety of different configurations. Flexibility must also extend beyond hardware concerns and the control software should be able to make use of different viewing geometries including lunar and off-axis

tracking.

Automation/Remote operation: In order to maximize the data acquisition of an installation, the tracker should be as autonomous in operation as possible. Recovery from a temporary loss of signal due to a passing cloud should be swift and automatic. At the same time it should be controllable, preferably (again because of the remoteness of one of our sites) through a low-bandwidth communication link.

Error reporting and recovery: It is extremely advantageous to have along with the data, a log of the performance of the tracker, therefore it should be capable of reporting errors and confidence in the tracking. Also in view of the desire for automation, it should be able to recover from error conditions and/or shut down gracefully.

Integration with other equipment: As the tracker does not operate in isolation but in concert with other equipment, it should be capable of being controlled by other systems and also provide relevant data to those systems to enable the entire measurement suite to function optimally.

Cost: It should be reasonably priced.

4.3 System description

We have built and operated multiple versions of the CST, and one of the greatest strengths of the system is the ease in which alternative rotation stages, cameras, and mirrors can be exchanged. Such changes require only minimal modifications to the control software, thus making the CST a general purpose tool that can exist in many forms. The following sections describe the details of one version of the CST as currently employed at two of our observing stations, and §4.3.3 will discuss some variants.

4.3.1 Hardware

The mechanical design of the tracker is extremely simple with a small number of parts and a typical realization shown in Fig. 4.3 and described in detail here. It employs an altitude-azimuthal architecture which uses two mirrors to steer the solar beam into the laboratory, thus enabling the tracker to cover the full hemisphere of the sky. The first mirror is mounted on a Newport RVS80PP rotation stage (`http:`

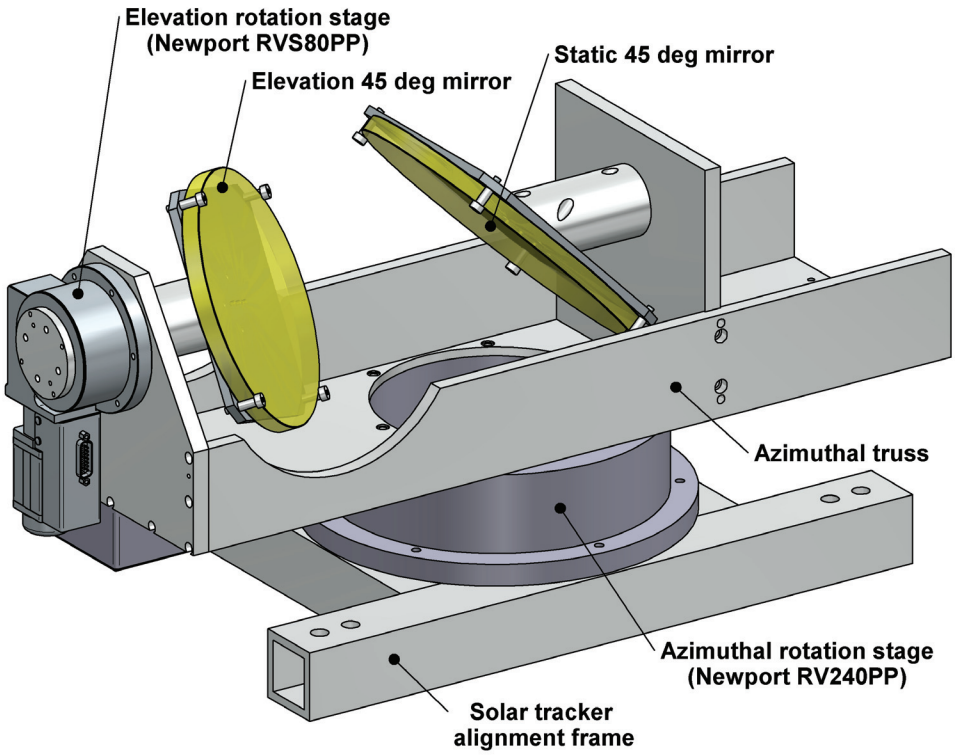

Figure 4.3: Schematic drawing of the CST design as implemented at the DAO.

`//www.newport.com/`) which provides elevation tuning. The beam reflected from the first mirror goes to a static mirror which transfers the light straight down into the laboratory. This assembly sits on a truss made of a U-shaped aluminum extrusion which in turn is mounted on a Newport RV240PP rotation stage to provide azimuthal tuning. Both rotation stages are stepper motor driven and controlled via the Newport ESP301 driver which enables continual monitoring of any motor errors. Newport stages were chosen because of past positive experiences with the brand even in harsh environmental conditions with cold temperatures and high air humidity; however, given the flexibility in the design of the CST, rotation stages from other suppliers could be easily utilized. The mirrors are custom made elliptic borosilicate glass 0.5 inch thick flats with a SiO_2 protected aluminum coating. The mirrors are epoxied (using Milbond Adhesive System; Type I) to Kovar backplates in order to provide a stress-free joint. The choice to epoxy the mirrors also significantly simplifies the design by avoiding intricate attachment systems that must be perfectly matched to the chosen mirrors. Kovar has thermal expansion characteristics compatible with those of

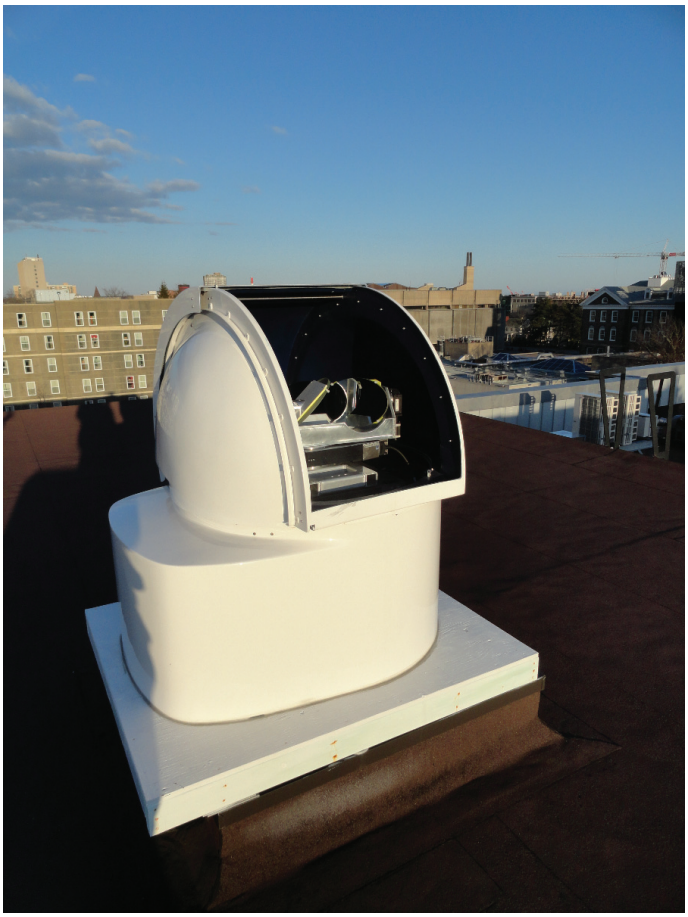

Figure 4.4: Image of the CST operating within the protective RoboDome on the roof of the DAO.

borosilicate glass which also helps to eliminate stress in the mirrors due to temperature changes. The complete tracker weighs about 35 kg and has the dimensions 70 cm x 30 cm x 35 cm (L x W x H). It can deliver a 175 mm diameter solar beam to the laboratory, limited by the dimensions of the hollow shaft of the RV240PP stage.

The solar tracker is placed on a frame inside a RoboDome made by Technical Innovations (`http://www.robodome.com/`). The RoboDome is a fully automated fiberglass telescope dome with a base and a shutter. The function of the RoboDome is to protect the solar tracker from bad weather conditions (Fig. 4.4).

Inside the laboratory, the majority of the solar beam is focused on the field stop of the spectrometer by flat mirrors and an off-axis parabolic mirror while a portion of the beam is directed to a network video camera (Fig. 4.5). A neutral

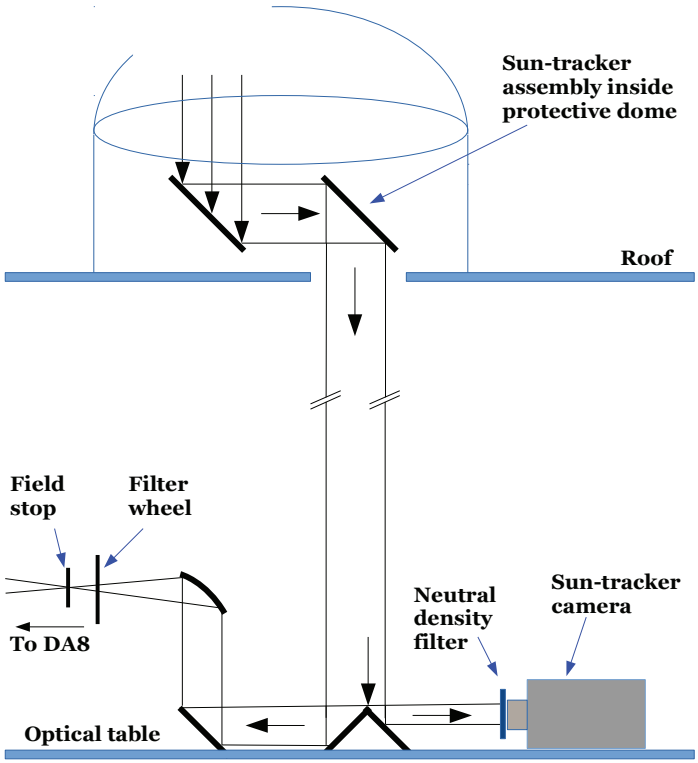

Figure 4.5: Simplified schematic of the optical path of the solar beam leading from the CST, passing into the laboratory, and being split into the sun-tracking camera and the DAO-DA8. (Not drawn to scale)

density filter (shade 11 welding glass) is placed before the lens to aid intensity level adjustments. The camera (NetcamXL, StarDot Technologies, 2048x1536 pixels, `http://www.stardot-tech.com/`) is equipped with a 48 mm zoom and optical doubler providing a 0.0019 deg per pixel (∼6.8 arcsec/pixel) image of the solar disk. The camera continuously takes images of the solar disk which are used to update the position of the solar tracker mirrors. The position of the camera serves as the control point for the active tracking system. While any minor shifts in the optics before the camera will be corrected, any changes downstream will not, and therefore it is necessary that the camera be positioned at an appropriate location close to the input of the measuring device. However, by providing flexibility in the positioning of this control point, the CST system is able to provide a steady solar beam for multiple instruments. This is especially important during validation and comparison

campaigns when we seek to minimize differences in the solar beams fed to the various spectrometers.

4.3.2 Software

The solar tracker, the dome, and the camera are all controlled via a 2-part software package written in the open-source programming language of Python. A primary control code, Trax, is run locally and is responsible for the direct control of the rotation stages and camera. The user interface is handled in a second code which may be run off-site and communicates with Trax via a TCP link. Users have the option of running the system from the command line or with a simple graphical user interface. The user interface programs are compatible with both Linux and MS Window environments. It is also possible to temporarily disconnect the control software while the CST continues to actively track, thus enabling easy transfer of control to another location without measurement interuption. This ability also insures against brief communication failures by having the CST enter into disconnect mode and listen for a new connection. If communication is not restored within 10 minutes the system automatically parks the tracker and secures the dome.

Communication with, and control of, the various hardware components (rotation stages, camera, dome) are handled within individual Python modules, and the introduction of a different component simply requires the writing of a new module containing the critical control functions. Information regarding which components (and therefore which modules) are in use at a given observing station are contained within a 'site file' that is passed to Trax during start up. All site-specific information is contained in the site file, making modifications to the main code unnecessary in most situations.

The control code has two modes for solar tracking: passive and active. In both modes the code calculates the apparent astronomical coordinates of the Sun on the sky depending on the geographical position of the tracker and local time and sends appropriate commands to the driver for mirror control. The ephemeris is calculated using the Python module pyephem which is based on XEphem written by Elwood Downey (`http://rhodesmill.org/pyephem/`). A simplified refraction calculation is included in the ephemeris calculation. Active mode is used to correct for any

systematic offsets from the passively determined coordinates that may be introduced by an imperfect construction or installation of the solar tracker. If the solar disk is temporarily obscured by clouds, the system continues to track in passive mode until it reacquires a signal, thus minimizing the time off target.

Active corrections are calculated by processing an image from the camera every passive step (roughly every 0.3 seconds) and locating the center position of the solar disk. The image processing software OpenCV (`http://opencv.org/`) is used to first threshold the image and locate the edges of the solar disk. An ellipse is then fit to the edge points using a least squares fitting. The final ellipse parameters are then subjected to a quality check (described in §4.4) before determining if an active correction is appropriate. To minimize the effect of any errors in the ellipse fitting process, a series of active corrections ($\sim$5) are typically averaged before being applied to the tracking.

Any offset of the solar disk relative to a reference pixel on the camera sensor is converted into an altitude/azimuth offset through a simple coordinate transformation. This transformation depends not only on the fixed geometry of the optical path, but also on the continually changing altitude and azimuth of the tracked object. From the perspective of the camera the image of the solar disk will rotate as it crosses the sky. As the optical path between the camera and the tracker may vary from site to site it was necessary to develop a calibration mode to simplify the process of determining the coordinate transformation at the new location. To achieve this, in calibration mode the tracker is physically "nodded" in both altitude and azimuth in order to empirically determine the parameters of the coordinate transformation. Since these values relate only to the physical geometry of the transfer optics they can be saved to a calibration file and the procedure does not need to be repeated unless the optical path to the camera is physically altered.

4.3.3 Current installations

Dalhousie Atmospheric Observatory

The CST has now been installed and is successfully operating in a variety of locations, each with its unique challenges. The system was originally designed to meet the requirements of the Dalhousie Atmospheric Observatory (DAO), located in

Halifax, Nova Scotia, Canada (44.6° N, 63.6° W, 65 m a.s.l.). The DAO is a standard mid-latitude site making solar absorption measurements at a large range of SZAs. The primary challenge in Halifax is the marine environment and the poor observing conditions that limit the number of days of measurement and test the shielding provided by the protective dome. Multiple versions of the CST have been successfully tested at the DAO, and in 2011, two units were employed to support Dalhousie Ground Station measurements during the BORTAS field campaign to investigate the transport and chemical evolution of biomass burning plumes [26, 45, 46].

Polar Environment Atmospheric Research Laboratory

During June 2013 an identical system was installed in the extreme high arctic at the Polar Environment Atmospheric Research Laboratory (PEARL) located on Ellesmere Island, Nunavut [80.05° N, 86.42° W, 607 m a.s.l.; 47]. FTIR measurements have been made from this location since 1993 [e.g., 48–50]. The original purpose-built tracking system consisted of a single tracking mirror and a quadrant diode-based active tracking system. The sun only reaches a peak altitude of $\sim$ 33.5° at this latitude, and therefore a single mirror rotating on two axes was sufficient to direct the solar beam into the laboratory. The old system tracked very well in ideal observing conditions, but required a level of periodic monitoring and manual intervention that prevented complete automation – a highly desirable capability given the high cost of maintaining personnel in the high Arctic. Without a passive tracking algorithm the system was dependent on user input for initialization or after a extended loss of signal, and adjustments to the gain in the quadrant diode detector were often necessary as the sun approached the horizon. These concerns drove the decision to replace the entire tracking system with a copy of the CST.

The extreme conditions at PEARL presented additional challenges for the CST over the DAO installation. Beyond the expected low temperature considerations, there was also concern regarding the 24 hour operation during the polar summer, and special care was required to avoid wrapping the elevation rotation stage cable. Finally, remote operation algorithms had to be designed to function successfully within the minimal bandwidth available. These challenges were all overcome, and during the summer of 2014 we successfully demonstrated remote operation and greatly

expanded our measurement capabilities in comparison to the past two observing seasons. Remote operation not only allowed continued observation days outside of intensive campaigns (107 days of measurements in 2014 compared to roughly 30 in 2012 and 2013), but also enabled us to extend each observing day leading to a factor of five increase in individual measurements.

The CST design can also be used at UV-visible wavelengths for differential optical absorption spectroscopy (DOAS) measurements. In their traditional zenith-sky viewing geometry, DOAS instruments are primarily sensitive to stratospheric trace gases. The CST enables direct-sun and off-axis viewing geometries [51], which can be used to obtain more information on tropospheric trace gases. Furthermore, lunar tracking can be used to take night-time measurements. This is particularly useful at high latitudes, where sunlight is not available during polar night.

An early passive-only version of the CST was installed above a Ground Based Spectrometer (GBS) DOAS instrument at PEARL in February of 2008 [52] and continues to operate at that location. In order to test the system, the CST and GBS participated in a formal NDACC intercomparison campaign in the Netherlands in 2009, where off-axis measurements of nitrogen dioxide and formaldehyde showed good agreement with other DOAS systems [53, 54]. This suggests that the CST provides good pointing and sufficient signal for off-axis viewing. At PEARL, the off-axis viewing geometry has been used to measure tropospheric bromine-monoxide [55, 56]. The CST has also been used to take direct-sun and lunar DOAS measurements at PEARL using the passive tracking technique, and the lunar measurements have shown promise for extending the GBS measurements into polar night. The system is currently being upgraded to implement active tracking. The application of the CST for the GBS DOAS instruments is described in detail by Adams [55].

Toronto Atmospheric Observatory

In a demonstration of the flexibility of the tracking software, the Toronto Atmospheric Observatory (TAO) located in Toronto, Ontario, Canada (43.66° N, 79.39° W, 174 m a.s.l.), successfully modified the code to control their existing rotation stages and mirrors. The modification was required as their mirror setup is comprised of a single alt/az tracking mirror which bisects the angle between the normal of the sun

and the north/south axis that ends at a fixed 45 degree mirror which then directs the solar beam downwards into the laboratory. The coordinate transformation required to correctly calculate the position of the tracking mirror employing such an optical path was based on the theory described in Hawat et al. [57]. Currently the TAO tracker is achieving ± 15 arc second accuracy although that is expected to improve as communication with the rotation stages is improved.

Others

In addition to the above currently functioning installations, the CST is being modified for use during the PAyload for Remote Sounding of the Atmosphere using Balloon Limb Experiments (PARABLE) high altitude balloon mission scheduled to fly in fall 2015. PARABLE is organized by the University of Toronto.

4.4 Performance Data

A primary advantage of a camera-based tracking system is the ability to easily record and quantify tracking errors. In this section we demonstrate the accuracy of the CST operating at the DAO as well as its ability to recover from a temporary loss of signal due to an obstruction such as a cloud or foreground object.

4.4.1 Solar Tracking

Every time an ellipse is fit to a solar image the result must pass a quality check to determine if an active correction is appropriate. First, the eccentricity of the ellipse is compared to a simple refraction calculation to determine if the solar disc is complete. If the solar disc is determined to be partially obscured, the system then checks the central position in an attempt to distinguish between an off-center image cut off by the edge of a mirror (requiring a movement to correct) and an image obscured by a cloud (requiring only patience). Ellipse fit information, as well as quality flags, are logged into hourly files that can be easily queried.

Figure 4.6a shows the deviation in one dimension (arc seconds) during a complete day of tracking under partly cloudy conditions. Scatter in the other dimension is of similar magnitude (not shown). Spikes in the data set correspond to times when the

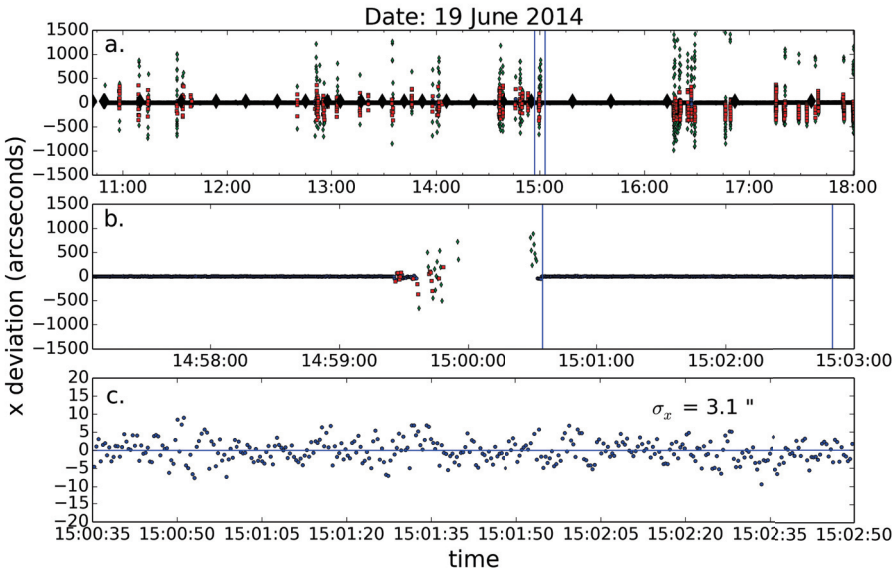

Figure 4.6: One dimensional tracking deviations (arcseconds) at the DAO on 19 June 2014. **(a)** Entire day of tracking showing the passage of many clouds. **(b)** Tracking deviations during the passage of a single cloud – marked by blue lines in (a) – that led to a temporary complete loss of signal. **(c)** Tracking deviations immediately after re-acquiring signal. Note that the vertical scaling for (c) is different than for (a) and (b).

solar disc was partially or completely obscured by cloud. Blue circles represent "good" fits where a complete solar disc was found and active corrections were possible. Red squares represent "bad shape" fits where the solar disc was partially obscured and no active correction was made. And green diamonds represent those fits that were sufficiently far from the ideal location that an active correction was made regardless of the ellipse shape in hopes of preventing the edge of the solar disc from moving outside of the field of view of the camera. The large black diamonds are times when the RoboDome is moving to prevent it from blocking the sun.

The passage of a single cloud is expanded in Fig. 4.6b which shows 6 minutes of active tracking around 15:00:00 LT. The optically thin edge of a cloud begins to pass in front of the sun at 14:59:25 and the ellipse fitting algorithm quickly determines that active corrections are no longer appropriate. By 14:59:55 the solar disc is completely obscured by the cloud and no signal is seen by the camera for ~ 30 s. However, during this time the CST continues to track the location of the solar disc using the passive

ephemeris calculations, and is thus able to quickly reacquire an active tracking lock within a few seconds of the sun reappearing at 15:00:30. Figure 4.6c further expands the final 2 minutes of tracking shown in 4.6b to demonstrate the high quality of active tracking immediately after re-acquisition of the signal. Note that the scale of the y axis changes significantly between panels b and c of Fig. 4.6.

Figure 4.8 gathers all of the "good" fits made over the full 7+ hours of solar tracking shown in Fig. 4.6 and displays the center points of the ellipses in a scatter plot. The origin is defined as the ideal location of the solar disc, and every point on the graph represents the location of a single fit. With over 60,000 data points it is necessary to plot the density of points on a log scale. Deviation in the radial direction is defined by adding the one sigma x and y deviations in quadrature. The small scatter of 6.5 arcseconds on a partly cloudy day demonstrates the effectiveness of our quality control algorithm described above. On a perfectly cloud-free day we are capable of reaching a scatter of only 4 arcseconds, but the higher deviations seen in Fig. 4.8 are still sufficiently small to be a negligible portion of the error budget in our FTIR measurements. The inset shows the scale of this tracking error figure relative to the entire sun.

Any future efforts to further reduce the scatter seen in Fig. 4.8 require a clear understanding of the source of the errors. Typical solar tracking errors can be partitioned into three categories: motion of the rotation stages, turbulence in the air column, and fitting of the ellipse to the image of the solar disc. An attempt to separate and quantify these error sources at the DAO was made on 25 March 2014. Software improvements since spring 2014 have further reduced the errors that will be discussed; however, the results of this experiment remain useful. The one-dimensional scatter during the short experiment is shown in Fig. 4.7, and typical tracking in active mode under normal sunny, but cold, conditions is seen in Region 1.

Region 2 shows an attempt to remove errors contributed by the motion of the rotation stages. The system was placed in standby at 15:07:40 and all motion was halted. Camera images continued to be gathered and analyzed as the solar disc drifted away from the reference pixel. Figure 4.7b more clearly shows the scatter during this portion of the experiment by removing the linear term from region 2. One sigma deviations along the y-axis of the camera are listed in Fig. 4.7b, and show

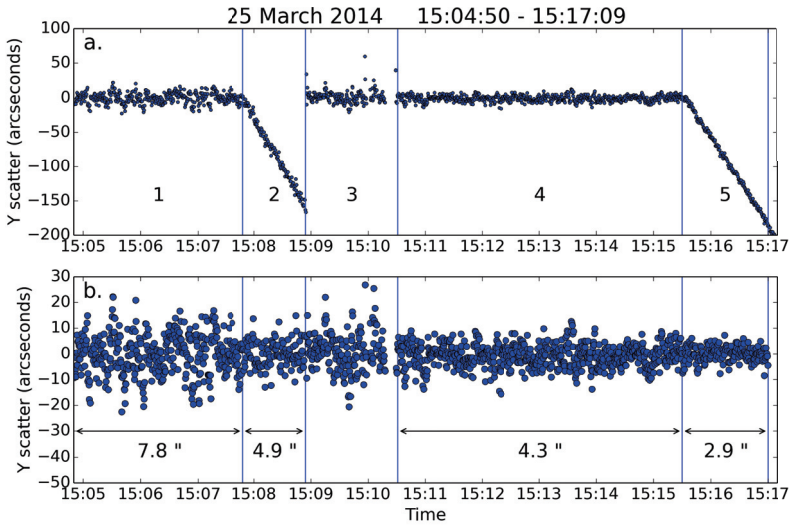

Figure 4.7: **(a)** One dimensional tracking deviations (arcseconds) during an error partitioning experiment at the DAO on 25 March 2014. **(b)** Same, but after removing a linear trend from regions 2 and 5. One sigma deviations are shown for regions 1,2,4,and 5. Regions 1 and 2 show the tracking errors during active tracking and in standby for a turbulent air column. Regions 4 and 5 show the same after installing a window to prevent air flow. Additional transients in region 3 are caused by installation of the window. See text for more detail.

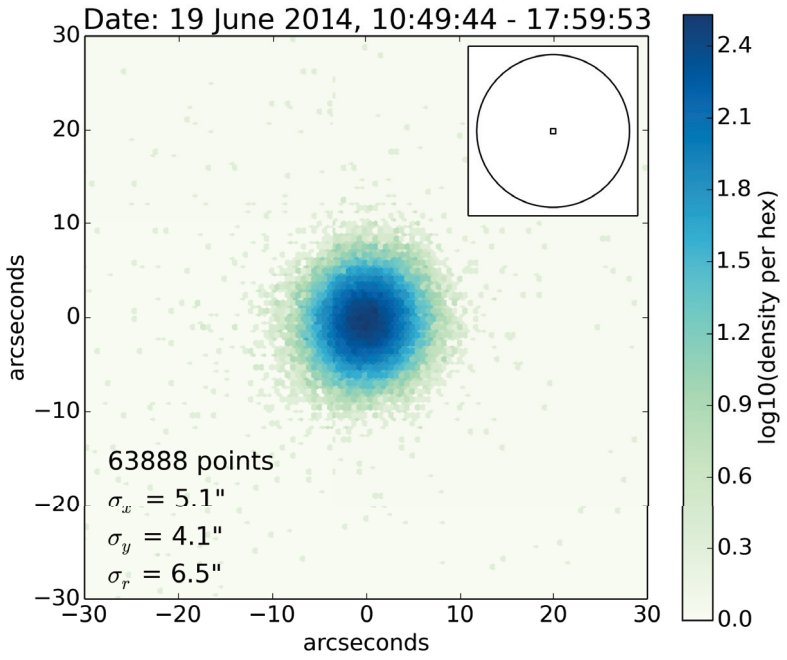

Figure 4.8: Logarithmic density plot of location of "good" fitted ellipses during active tracking at the DAO on 19 June 2014. Points correspond to all blue dots in Fig. 4.6. Inset in upper right shows the scale of the entire figure (inner box) relative to the full solar disc.

a significant reduction in scatter from 7.8 to 4.9 arcseconds once the rotation stages were still.

25 March 2014 was a cold day in Halifax and it was observed that the contrast in temperature between the laboratory and outside was driving a turbulent flow of air upwards through the roof opening and leading to significant scintillation of the solar beam. Region 4 shows an attempt to quantify the error associated with this air flow by temporarily installing a Plexiglass window to prevent air exchange between the lab and the exterior environment. Scatter associated with the installation process is noticeable in region 3 and thus no statistics were calculated during this time. Active tracking with the window (region 4) has a one sigma scatter of 4.3 arcseconds, similar to region 2 when the rotation stages were not in motion, but the window was not yet installed.

Finally, at 15:15:30, the CST was once again placed in standby mode and a further reduction in scattering was observed (region 5). At 2.9 arcseconds, the one sigma scatter along the y axis seen in region 5 of Fig. 4.7b represents the error associated with the process of fitting an ellipse to an image with finite pixel size and potential sensor noise. The magnitude of the fitting error appears to be roughly comparable to the scatter contributed by the motion of the rotation stages which have minimum incremental motions of 3.6 and 0.7 arcseconds in azimuth and altitude respectively. However, both sources of error can be dominated in the winter months by the turbulence of the air column. Many TCCON sites use a permanently installed CaF_2 window to prevent this turbulence, but at the DAO we are interested in observing at wavelengths beyond the cut off of CaF_2 and appropriate window materials are expensive and often hygroscopic.

4.4.2 Lunar Tracking

The CST is also capable of tracking the lunar disc with high precision. This is particularly useful at high latitudes, where sunlight is not available during polar night. Tracking the full moon requires no special changes to the code, but a new quality-checking algorithm is needed to actively track a partially illuminated lunar disc. While we rely on refraction calculations to assess the quality of a fitted solar disc, we instead use the phase of the moon to determine the range of acceptable lunar

ellipse parameters. At the DAO the CST has been shown to track even a 50% phase moon better than 15 arcseconds. Lunar measurements recently began at PEARL during the fall of 2015, and will be attempted at the DAO upon completion of the 24-bit DAQ upgrade.

4.5 Aligning the CST to a FTIR spectrometer

In the previous section we demonstrated that the solar beam provided by the CST is exceptionally stable relative to the LOS of the camera. The process of properly coupling this solar beam to another instrument is the responsibility of the user. As the CST may be used for a variety of tracking needs, it is not possible to provide a complete description of all methods of aligning instruments to the solar beam. However, in this section we will describe one method that may be used to couple the CST to a FTIR spectrometer making solar absorption measurements. This procedure is in the process of being applied to the Bruker IF125HR located at PEARL, and the preliminary results shown here are derived from measurements made in the spring and summer of 2015.

4.5.1 Solar Lines

A careful fitting of high resolution solar spectra in the MIR or NIR requires accounting for absorption features associated with the outer layers of the sun. The rotation of the sun (with a period of $\sim$ 26.7 days) produces Doppler shifts in these features along the solar equator with a magnitude of $\delta\nu/\nu \sim 3.9 \times 10^{-7}$ for every 1 arcmin of pointing error [44]. Pointing errors purely perpendicular to the solar equator will not result in solar line shifts. As some of these absorption features are located near lines of atmospheric interest, the solar line shifts must also be fit during the retrievals of trace gas columns, and are commonly used as an estimate of the magnitude of any tracking errors.

As discussed in §4.3.2, the CST's use of an altitude-azimuth system causes the solar beam to rotate about the LOS of the camera over the course of the day. If the LOS of the spectrometer is offset from the center of the sun, then this beam rotation will cause the FOV of the instrument to trace out an arc on the solar disc over a full day of measurements. Such an offset will manifest itself as a quasi-sinusoidal

trend in the solar line shifts. While any individual measurement of the solar line shift only provides the one-dimensional offset along the solar equator, by quantifying the magnitude and phase of the daily sinusoid we can accurately identify both the magnitude and direction of the offset.

If the CST solar beam is only supporting one instrument, it is easiest to correct such an offset by adjusting the tracking position of the sun on the CST camera. Moving the solar beam is superior to a seemingly equivalent adjustment to the transfer optics between the CST camera and the spectrometer because the change is made completely within the software and is thus fully repeatable. However, it is important to note that this process can only be used to align the CST beam to a single FTIR. Additional instruments sharing the solar beam must be aligned via transfer optics.

4.5.2 Results

We began applying this method to the Brucker IF125HR operating at PEARL during the 2015 polar sunrise campaign. Due to the significant cycle time of measuring, transferring, processing, interpreting, and responding to observed solar line shifts gathered from the high-Arctic, this procedure is still in process. However, our results to date are sufficient to demonstrate that we are able to monitor and modify the co-alignment of the CST - FTIR system. We also found that the measurements gathered prior to a successful co-alignment can be corrected by properly accounting for the LOS offset using a two-stage retrieval process.

The PEARL IF125HR has a field of view ~ 9 arcmin, and was initially aligned to the CST beam by maximizing the signal at the detector. Using the spectral retrieval software GFIT (described in Wunch et al. [41]), we began monitoring the NIR line shifts during the 2015 polar sunrise campaign.

Figure 4.9 shows all observed solar line shifts derived from TCCON measurements from March to May 2015, and at first glance appears to show a significant amount of scatter. However, Fig. 4.10 expands two days of measurements to demonstrate that there is actually relatively little scatter around a strong daily trend. This trend represents the rotation of the the solar image on the CST camera described above. With knowledge of the rotation it is possible to fit this daily trend with a simple sinusoidal function, and derive a correction to the CST LOS. Note that the modelled

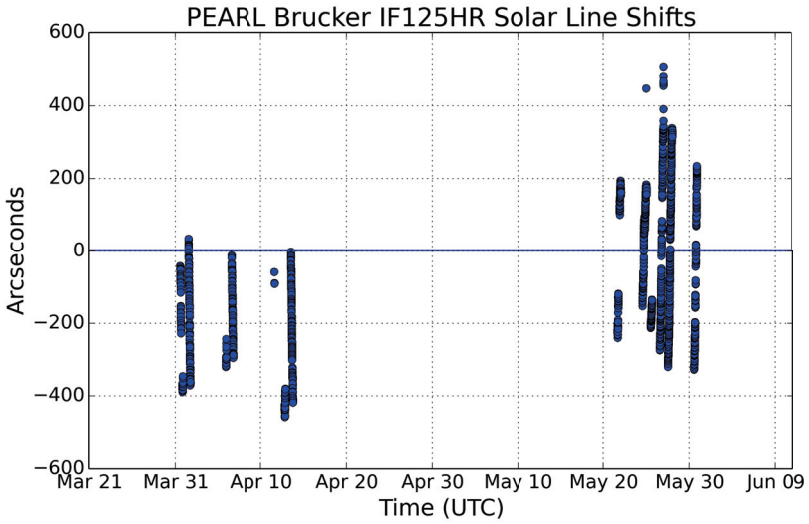

Figure 4.9: All PEARL Bruker IF125HR solar line shifts derived from TCCON NIR measurements from March to May 2015. No measurements were gathered from mid-April to mid-May due to a dome shutter failure.

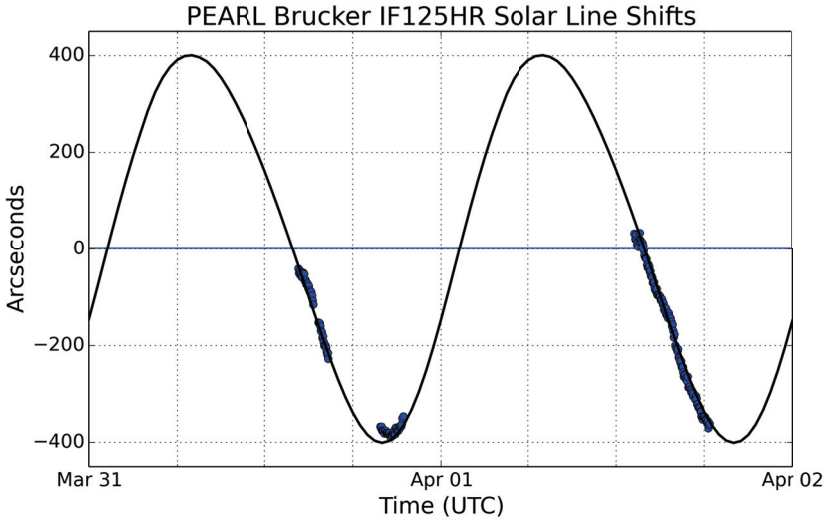

Figure 4.10: PEARL Bruker IF125HR solar line shifts derived from TCCON NIR measurements on 31 March and 01 April 2015. Black line represents a simplified model of the shifts assuming a systematic offset of $\sim$ 400 arcseconds.

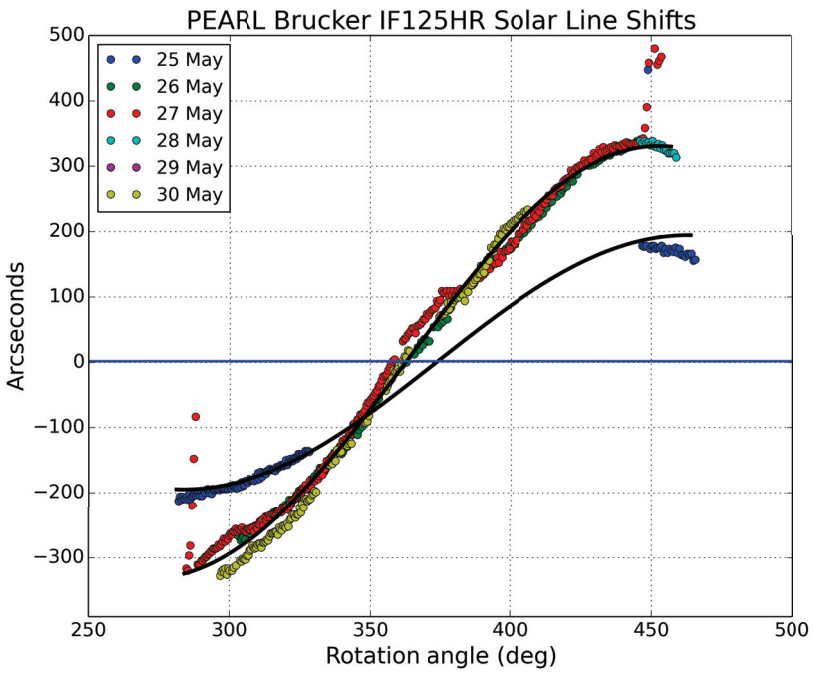

Figure 4.11: PEARL Bruker IF125HR solar line shifts derived from NIR measurements in late May 2015. The sudden shift after 25 May represents the introduction of a new wedged ND filter that shifted the LOS of the CST.

sinusoid is a function of rotation angle, not time, thus explaining the skewed shape apparent in Fig. 4.10.

It is critical that no portion of the optical path is altered during and following the co-alignment procedure. This was demonstrated clearly in late May when the ND filters in front of the CST camera were changed. The new filter was apparently wedged differently than the original leading to a slight shift of the solar beam that is easily visible in the solar line shifts. Figure 4.11 shows the solar line shifts from 25 to 30 May 2015 as a function of the rotation of the solar image on the CST camera. Two sinusiodal relationships are clearly seen in the data with a sudden shift between the 25 and 26 May reflecting the introduction of the new ND filter.

Some changes to the optical path are unavoidable. For example, the PEARL IF125HR provides data to both the TCCON and NDACC communities, and therefore must switch beam-splitters and detectors on a regular basis. This exchange slightly shifts the LOS of the spectrometer and a similar shift must also be made to the solar

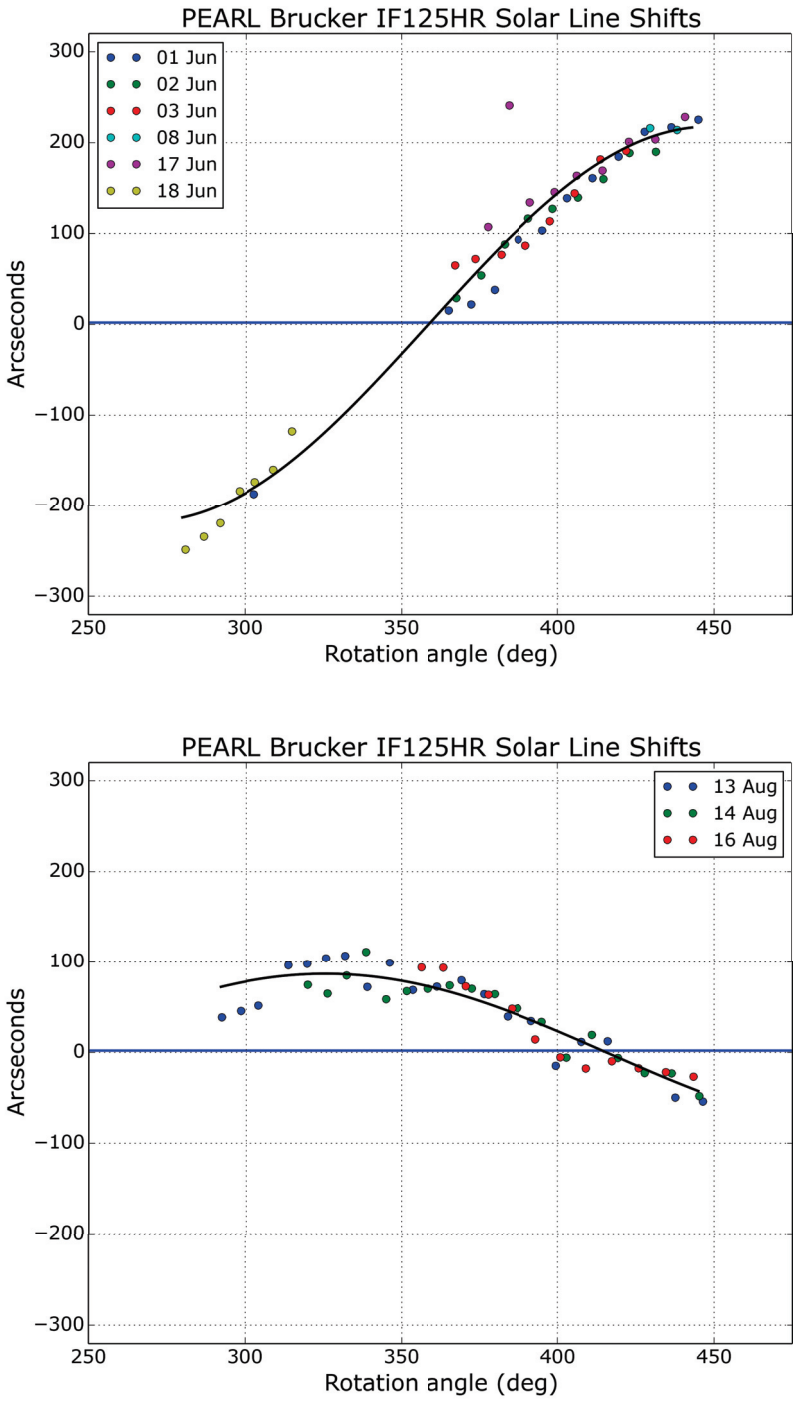

Figure 4.12: Daily trend in PEARL Brucker IF125HR solar line shifts derived from MIR measurements in early June 2015 (top) and mid August (bottom). June data reveal a systematic offset of ∼220 arcseconds between the CST and IF125HR, which decreases to ∼85 arcseconds in August after shifting the CST.

beam for a suitable co-alignment to be maintained. The procedure described above has been repeated using solar lines fit by the spectral software SFIT4 (discussed in more detail in Ch. 6) and recent results are shown in Fig. 4.12. Operationally, the process of changing beam-splitters now includes shifting the CST to match the changing LOS of the IF125HR.

NDACC measurements in the MIR are not as frequent as the TCCON NIR measurements shown above, and there is more scatter in the derived solar line shifts. The increased scatter is likely a result of SFIT4's use of smaller spectral windows that contain fewer isolated solar absorption features. It is also important to note that these measurements were made at SZAs that would be considered extreme at lower latitudes, and with large airmass factors, as well as extreme temperatures. Together these add a significant amount of noise to all of the solar line shift data.

4.5.3 Applying an air mass correction

Once the CST and spectrometer have been perfectly co-aligned, the trace gas retrieval process is straightforward and simply uses the SZA of the center of the solar disc during the observation. However, for the PEARL IF125HR the alignment offset went unnoticed during the 2014 observing season, and despite on-going correction efforts, still exists in 2015. When processing this dataset it is necessary to account for these pointing errors or else significant air mass errors can propagate through to the final results.

As a diagnostic, a typical TCCON retrieval of the column-averaged dry-air mole fraction of CO_2 (X_{CO_2}) also uses the retrieved column of O_2 (from the band centred at 7882 cm^{-1}) to calculate the dry-air mole fraction of the atmosphere, X_{air}, which should be unity by definition. A daily trend in X_{air} is often either the result of timing errors, or pointing errors such as those introduced by the offset of the CST beam [41]. Figure 4.13 shows values of X_{air} during the two days of measurements shown in Fig. 4.10. Before accounting for the LOS offset, GFIT retrieves a strong daily trend as the procedure assumes that we are observing at a different SZA than we truly are.

The impact of this pointing error on X_{CO_2} can be minimized by using the O_2 column instead of the surface pressure to derive the dry-air column. As both the CO_2 and O_2 columns are affected by the pointing error, its influence can be cancelled

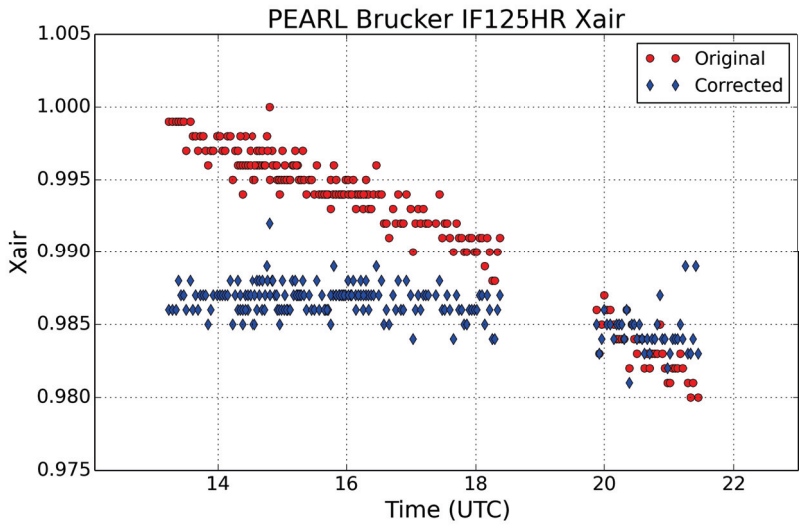

Figure 4.13: X_{air} results from 31 March and 01 April 2015 showing an undesirable daily trend before (red) and after (blue) accounting for the offset between the LOS of the CST and FTIR.

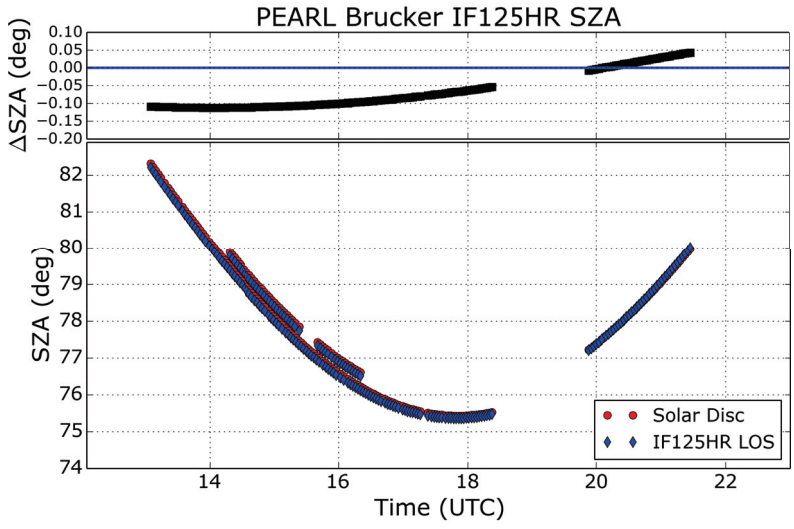

Figure 4.14: Comparison between the true SZA (red) and the zenith angle of the PEARL IF125HR LOS (blue) for 31 March and 01 April 2015. The difference in pointing is expanded in the upper panel.

during the ratio [41]. This technique is commonly used by TCCON, but is unavailable to the NDACC community as there are no suitable O_2 features in the observed portion of the MIR. Thus, it is necessary to develop a method to account for the pointing errors in the MIR retrievals.

The solution is to perform a two-stage retrieval. We begin by assuming perfect pointing and perform a normal retrieval of all products. The daily trend in the solar line shifts from this run are then used to calculate the true LOS of the FTIR. If any changes have been made to the optical path of the system, then it is critical that this process is applied separately to each pointing. New SZA values are then calculated (Fig. 4.14) and are passed to the second and final retrieval. The impact of the new SZA values on X_{air} can be seen in Fig. 4.13. The daily trend has been removed, and the constant offset from unity that remains is seen throughout the TCCON network and is believed to be primarily caused by spectroscopic errors [41].

Chapter 5

DAO support of the BORTAS campaign

In July 2011, mere weeks after the initial solar measurements were made by the DAO-DA8, Dalhousie University served as a ground station in support of an aircraft mission to study the influence of biomass burning emissions on the downwind chemistry of the atmosphere. The experiment was well timed as large fires in Western Ontario burned a considerable region of the boreal forest that July and multiple smoke plumes were effectively transported to the Halifax region. This chapter investigates the transport history of the largest carbon monoxide plume seen during the campaign by the DAO-DA8 spectrometer. The material in this chapter was published as Franklin et al. [46]. Although there exists some minor overlap with earlier chapters of this thesis (e.g., §5.3), the repeated material was kept to preserve the flow of the chapter.

5.1 Motivation

Wildland fires have burned an average of 2.3 million hectares of the Canadian boreal forest annually over the past 25 yr, with the majority of large fires being started by lightning strikes (data from the Canadian Wildland Fire Information System; `http://cwfis.cfs.nrcan.gc.ca/`). These biomass burning events are a significant source of carbonaceous aerosols and trace gases to the atmosphere. In addition to the local ecological effects, it has been demonstrated that plumes lofted into the free troposphere are capable of undergoing significant long range transport (LRT) and chemical evolution [e.g., 17, 58, 59]. The climatic implications of these perturbations to the troposphere are extremely sensitive to the characteristics of the LRT. As lofting of air via meso-scale convection often occurs during LRT, clouds may form and aerosol particles may be scavenged by cloud/rain drops and potentially removed from the atmosphere via wet-deposition. These processes are therefore critical in determining aerosol lifetimes [e.g., 5, 60]. Many of these processes remain poorly constrained in

atmospheric models [e.g., 61, 62], and further observations are necessary.

A number of recent field campaigns have looked at mid- to high-latitude wildfires and their impact on atmospheric composition. For example, the NASA Arctic Research of the Composition of the Troposphere from Aircraft and Satellites (ARCTAS) campaign in the summer of 2008 investigated the influence of biomass burning outflows on the Arctic environment [24]. An emphasis was placed on quantifying the chemical composition and near-field evolution of the fire plumes, as well as on better understanding their radiative impact on a regional scale. Transport pathways and the lofting efficiency of black carbon (BC) detected over Alaska during the ARCTAS campaign were investigated by Matsui et al. [63] who found a discrepancy between BC released by wildfires in northern Russia, and BC released by anthropogenic sources further to the south. Lofting of BC associated with the northern wildfires generally occurred isentropically at low relative humidity, while lofting of BC from more southern sources was often associated with rapid ascent and heavy precipitation [63].

The Aerosol Radiative Forcing in East Asia (A-FORCE) campaign in the spring of 2009 specifically investigated the role of wet removal of BC in Asian outflow [64]. Precipitation was found to be the most important scavenger of BC from the atmosphere. However, previous studies [e.g., 65] have shown that precipitation washout can be inhibited by smoke thereby allowing aerosols to reach the upper troposphere. The interaction between the convective plumes from the fires, aerosols from the fires, and the local meteorology is complex and requires further study.

The Quantifying the impact of **BOR**eal forest fires on **T**ropospheric oxidants over the Atlantic using **A**ircraft and **S**atellites (BORTAS) project was a multi-national campaign led by the University of Edinburgh and conducted over eastern Canada during the summers of 2010 and 2011. The overall goal of BORTAS was to investigate the connection between the composition and the distribution of biomass burning outflow, ozone production and loss within the outflow, and the resulting perturbation to atmospheric chemistry in the troposphere [26]. The primary datasets of the campaign were provided by the UK Facility for Airborne Atmospheric Measurements (FAAM) BAe-146 Atmospheric Research Aircraft (ARA) flying out of Halifax, Nova Scotia. These measurements were only available during the 2011 portion of the

campaign (BORTAS-B; herein referred to as BORTAS). A series of 14 flights designed to sample biomass burning plumes of varying ages at a variety of altitudes were completed between 15 July to 03 August 2011. Flight paths were selected from the predictions of forecast models in order to maximize the probability of intercepting plumes. Specific flight paths are detailed in Palmer et al. [26]. A simultaneous ground-based campaign was undertaken to support the ARA measurements. In-situ and remote-sensing instruments were clustered at the Dalhousie Ground Station (DGS) located at Dalhousie University (Halifax, NS; 44.6° N, 63.6° W, 65 m a.s.l.). The full list of DGS instruments is described in Palmer et al. [26] and Gibson et al. [27].

In this work we present observational evidence of a biomass burning plume that experienced a period of precipitation scavenging during transport to the DGS. We begin by presenting a summary of the 2011 Canadian wildfire season. We follow this in §5.3 by describing the different instruments and methods used in this work. In §5.4 we present the time series of ground-station measurements and compare them with available aircraft and satellite data, as well as with transport model results. In §5.5 we present and discuss the observational evidence for precipitation along the plume trajectory. We conclude with a summary of our results.

5.2 Overview of the 2011 wildfire season

The wildfire season in the Canadian boreal forest runs from April to October with the majority of fires occurring from June to August (Canadian Forest Service; `http://cfs.nrcan.gc.ca/`). BORTAS measurement flights based out of Halifax were scheduled from 18 July to 31 July 2011 to coincide with this climatological peak.

A hot and unusually dry summer contributed to the province of Ontario recording a total of 1334 fires during the 2011 season with a total burned area of over 635 000 ha, or roughly 5 times the 10 yr average affected area (data from the Ontario Ministry of Natural Resources; `http://www.mnr.gov.on.ca/`). The Sioux Lookout 70 fire (SL70; 52.3° N, 90.7° W) was the largest recorded Ontario fire in over 50 yr with a total burn area of 141 000 ha. Ignited by a lighting strike on 14 July, SL70 burned for 6 days before being extinguished by rainfall. Smaller, yet still intense, wildland burning

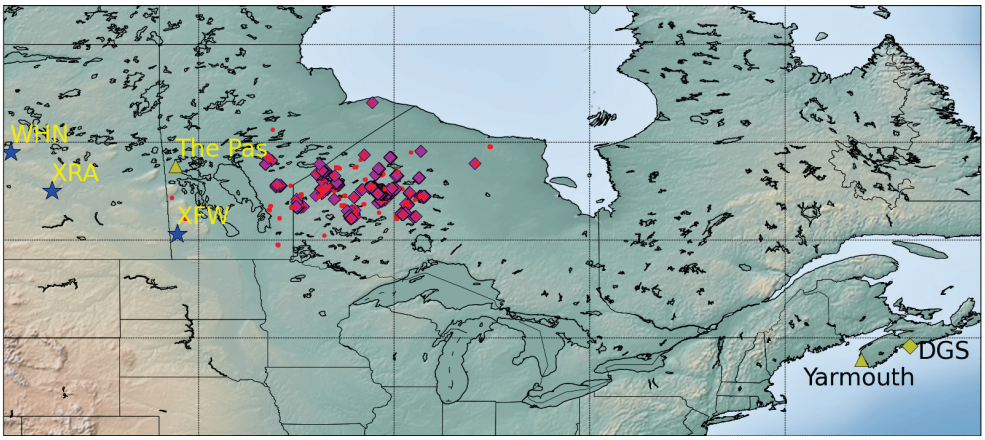

Figure 5.1: Map of eastern Canada showing all MODIS hotspots from 17 July to 20 July 2011 as detected by the Aqua and Terra satellites. Fires with radiative powers over 100 MW are shown as diamonds. The location of the DGS is marked with a yellow diamond in the lower right, while radio sonde stations used in this study (The Pas, Yarmouth) are marked with yellow triangles. RADAR facilities mentioned in the text (WHN, XRA, XFW) are marked with blue stars.

occurred in eastern Manitoba during the same period. Figure 5.1 shows the locations of fires catalogued by the NASA Fire Information for Resource Management System [FIRMS; 66], using data from the MODerate Resolution Infrared Spectroradiometer (MODIS) instruments aboard the Aqua and Terra satellites [67].

We will show that the differences in the local meteorology at each of these fire regions are a significant factor driving the differences in detections made down-stream. A series of meso to synoptic scale disturbances tracked over Manitoba, Ontario, and southern Quebec during the campaign and provided the means for lofting biomass burning plumes out of the boundary layer. Beyond rapid uplift within thunderstorms, other possible mechanisms for initiating lofting include localized convective motions from the fires themselves, as well as transport along the warm conveyor belt of the synoptic lows [58]. Lofted plumes were efficiently transported toward the DGS via a strong mid-tropospheric flow driven by a major low pressure system situated over the northern Quebec/northeastern Hudson Bay region, while lower level plumes remained under the influence of a slower westerly wind. A more detailed overview of the general meteorological conditions during the BORTAS mission can be found in Palmer et al. [26].

5.3 Measurements and models

This work focuses on the measurements made by the four remote-sensing instruments that were operating at DGS during the BORTAS campaign: two Fourier Transform Spectrometers (FTSs) providing solar absorption measurements of trace gases, a Sun Photometer providing aerosol optical depth during daylight hours, and a Star Photometer providing the same during clear nights.

5.3.1 Fourier Transform Spectrometers

Dalhousie Atmospheric Observatory DA8

The primary Dalhousie Atmospheric Observatory (DAO) instrument is a newly refurbished high-resolution DA8 FTS (DAO-DA8) manufactured by ABB (Bomem) and installed at Dalhousie University in 2010. The spectrometer is owned by the Canadian Space Agency, and the modifications to the electronics have been made at Dalhousie University. The heart of the DAO-DA8 is a Michelson Interferometer with a maximum optical path length of 250 cm providing an unapodized resolution of $0.004\,\mathrm{cm}^{-1}$. Alignment is maintained over the full optical path by monitoring the modulated signal of an internal HeNe laser. In accordance with procedures developed by NDACC, solar absorption measurements are made through a series of 6 narrow band interference filters to optimize the signal to noise ratio. Every filter measurement consists of 4 to 6 co-added scans, enabling us to sample the entire spectrum from 750 to $4300\,\mathrm{cm}^{-1}$ (via all 6 filters) at full resolution every 55 min.

A dedicated active-tracking heliostat was designed and built to support the DAO-DA8 spectrometer. The use of a camera in the tracker allows us to accurately monitor the position of the sun and make active feedback corrections, while a passive system of ephemeris calculations enables us to continue tracking in the event of a temporary loss of signal. This arrangement permits high tracking precision with a root mean square (rms) error of ~ 10 arcseconds.

PARIS-IR

The Portable Atmospheric Research Interferometric Spectrometer for the Infrared [PARIS-IR; 68] was temporarily installed at the DGS during the BORTAS campaign.

PARIS-IR was built by ABB (Bomem) as a ground-based adaption of the Atmospheric Chemistry Experiment FTS (ACE-FTS) aboard the SciSat satellite [69]. With a maximum optical path difference of ±25 cm, PARIS-IR measures the entire 750–4400 cm^{-1} spectral region with an unapodized resolution of 0.02 cm^{-1} every 7 min.

A second independent solar tracker of the same design as described above was installed at the DGS to provide PARIS-IR with a solar beam for its absorption measurements.

Trace gas retrievals

Columns of carbon monoxide (CO), ethane (C_2H_6), and nitrous oxide (N_2O) were derived from measured solar spectra using an optimal estimation technique [30, 31] as implemented by the retrieval software SFIT2 version 3.94c [70, 71]. SFIT2 first calculates a spectrum using the High-Resolution Transmission Molecular Absorption Database (HITRAN) 2008 line list [72] and a priori Volume Mixing Ratio (VMR) profiles of trace gases. This synthetic spectrum is then compared and fitted to the observed spectrum by varying the vertical profile of the desired species and scaling the profiles of any interfering gas species. The retrieval is performed simultaneously over multiple short regions of the spectrum (referred to as microwindows) recommended by the NDACC community.

The two FTS systems retrieve trace gas profiles on vertical grids with different resolutions. PARIS-IR retrieves gas profiles on a 29 layer grid, while the higher spectral resolution of the DAO-DA8 allows us to retrieve profiles on a 48 layer grid. Thus, a proper comparison of the total gas column measurements between the two instruments requires smoothing the DAO-DA8 profiles using the PARIS-IR averaging kernels. This process is detailed in Griffin et al. [45]. Total and partial column values are calculated from the retrieved VMR profiles by integrating over the altitude range taking into account the density of the atmosphere at each layer.

With one exception, a priori VMR profiles for trace gases above Halifax were taken from 40 yr averages (1980–2020) of the Whole Atmosphere Climate Chemistry Model [WACCM V6; 73]. Halifax is a marine site and the highly variable nature of water vapour above the DGS required the use of more accurate daily a priori

water vapour VMR profiles. The lowest 20 km of the WACCM water vapour VMR profile was replaced with profiles calculated from radiosondes released every 12 h from Yarmouth, NS (43.9° N, 66.1° W, 9 m a.s.l.). For the DAO-DA8, the inclusion of the radiosonde derived water vapour profiles removed a non-physical oscillation from the retrieved CO VMR profiles without significantly changing the total column. Although the temporal resolution of PARIS-IR greatly exceeds that of the DAO-DA8, the lower spectral resolution decreases the sensitivity of the instrument to CO above $\sim$ 5 km, and only permits retrieval of total column abundances. Therefore, daily water vapour VMR profiles were not necessary in the PARIS-IR retrievals, and the mean WACCM a priori VMR was used. Pressure and temperature information were taken from the National Centers for Environmental Prediction (NCEP) each day and then interpolated onto the retrieval altitude grids.

DAO-DA8 retrievals of C_2H_6 produced $\sim$ 1.3 Degrees of Freedom of Signal (DOFS) and therefore only permit us to state a total column measurement. In contrast, N_2O retrievals have $\sim$ 3.0 DOFS, but the observed N_2O enhancement is very modest and therefore we also only present total column measurements. CO is retrieved with $\sim$ 2.4 DOFS, and the DAO-DA8 resolves the wings of the pressure broadened CO absorption lines sufficiently well to allow calculation of partial columns in addition to the total column value. Vertical limits of 0 to 4 km and 4 to 20 km were chosen to provide a full DOFS in each partial column. The contribution of CO above 20 km to the total column is less than 2 %.

Uncertainties in the derived columns were calculated in a manner similar to that described by Batchelor et al. [48] and Griffin et al. [45]. Errors considered in our calculations include the smoothing error, measurement error, uncertainties in the HITRAN 2008 line parameters, and errors in the temperature profile.

5.3.2 Sun and star photometers

Dalhousie University has hosted an automated CIMEL Electronique 318A as part of the AEROCAN sun photometer network since June 2002. The AEROCAN network is a subset of the worldwide Aerosol Robotic Network [AERONET; 74]. The CIMEL sun photometer provides measurements of vertically integrated aerosol properties at a variety of optical wavelengths with a sampling resolution of about 3 min.

A star photometer operated by the University of Sherbrooke was temporarily installed at the DGS during the BORTAS campaign. Operating under a similar principle to the sun photometer, this instrument uses a telescope to monitor the light of known bright stars, thus allowing measurements of aerosol properties any cloud free night [75].

The Aerosol Optical Depth (AOD) at 500 nm is partitioned into a fine (roughly sub micron) and coarse mode via a spectral deconvolution algorithm [SDA; 6]. As aerosols associated with the long range transport of biomass burning plumes are expected to be on the sub micron scale, we will only present the post-calibrated level 1.0 SDA-derived fine mode AOD in this work.

5.3.3 Dalhousie Raman Lidar

The Dalhousie Raman Lidar (DRL) employs a Nd : YAG laser to produce 532 nm light at a pulse frequency of 20 Hz. Vertical profiles of atmospheric scattering are derived from the returned signals at both the elastic scattering wavelength as well as at the nitrogen (N_2) Raman-shifted wavelength of 607 nm. A complete description of the instrument, as well as a detailed discussion of the uncertainties in the measurements, is available in Bitar et al. [76].

5.3.4 BAe-146 aircraft instruments

A multi-instrument payload was installed aboard the BAe-146 ARA during the BORTAS campaign flights. A full listing of instruments can be found in Palmer et al. [26]. Of most interest to this work are the Aerosol Mass Spectrometer (AMS) and CO monitor. The AMS had a temporal resolution of 30 s and provided measurements that include NH_4, SO_4, NO_3, and organics [77]. The CO monitor operates via UV fluorescence with a temporal resolution of 1 s, and a sensitivity of 1 ppb [78, 79].

5.3.5 Numerical simulations

The transport histories of plumes intercepted by the aircraft and the DGS remote sensing instruments were first analyzed using the HYbrid Single-Particle Lagrangian Integrated Trajectory (HYSPLIT) model [80, 81]. Runs were initialized at the DGS and along the aircraft flight track and used NCEP Global Data Assimilation System

(GDAS) reanalysis fields to model the transport to roughly locate the origins of the plumes. A more quantitative transport analysis was then performed using the Lagrangian Particle Dispersion Model FLEXPART [82]. Meteorology provided by the NCEP Global Forecast System (NCEP GFS) was used by FLEXPART to advect CO from biomass burning locations. Additional runs were completed using particles susceptible to removal via wet deposition.

5.4 Results

5.4.1 Dalhousie Ground Station observations

Total columns of CO, C_2H_6, and N_2O retrieved from the DGS spectrometers during the extended BORTAS ground campaign are shown in Fig. 5.2a–c. Biomass burning is a significant source of CO and C_2H_6, and a moderate source of N_2O to the atmosphere. While CO and C_2H_6 are removed in a matter of months via reaction with OH radicals, N_2O has been estimated to have a tropospheric residence time of over 100 yr, eventually being transported to the stratosphere where it is susceptible to photodissociation [5]. Episodic correlated enhancements in these three species are considered to be evidence of biomass burning. PARIS-IR retrievals only detect significant enhancements in CO during the campaign period, and thus these are the only PARIS-IR measurements shown in Fig. 5.2. Total column CO values measured by DAO-DA8 agree with PARIS-IR retrievals within 4 % after smoothing to a comparable vertical resolution [45].

Fine-mode AOD data derived from sun and star photometer measurements during the campaign are shown in Fig. 5.2d. As demonstrated in Fig. 7 of Griffin et al. [45], the fine-mode AOD is generally positively correlated with total column CO throughout the campaign. However, not all measurements of specific air masses follow this trend, and it is one of these exceptions that is investigated in this work.

The strongest CO signal seen in Fig. 5.2 is associated with a plume that arrived in the afternoon of 20 July 2011. Solar tracking instruments at the DGS intercepted the plume to the southwest before it was detected by zenith pointing instruments (including the DRL). Measurements of CO and AOD during this event are expanded in Fig. 5.3a and b. The total column of CO begins to rise at 17:30 UTC from a local

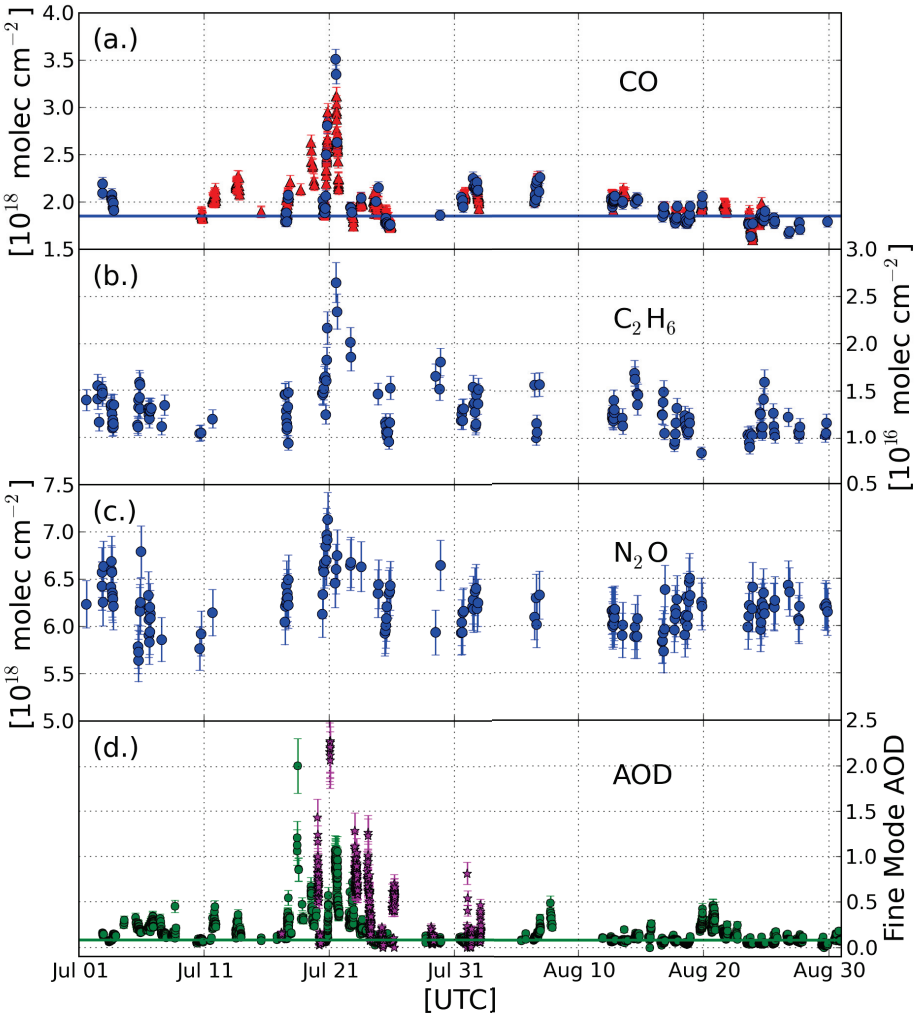

Figure 5.2: DGS remote-sensing measurements observed during the extended BORTAS campaign. **(a)** Total retrieved column of CO as measured by the DAO-DA8 (blue circles) and PARIS-IR (red triangles). Typical background column of CO above the DGS in the summer is shown by the horizontal blue line. (**b** and **c**) Total column of C_2H_6 and N_2O derived from DAO-DA8. **(d)** Fine mode AOD derived from the CIMEL sun photometer (green circles), and star photometer (magenta stars). Background level of fine mode AOD at the DGS is shown by the horizontal green line.

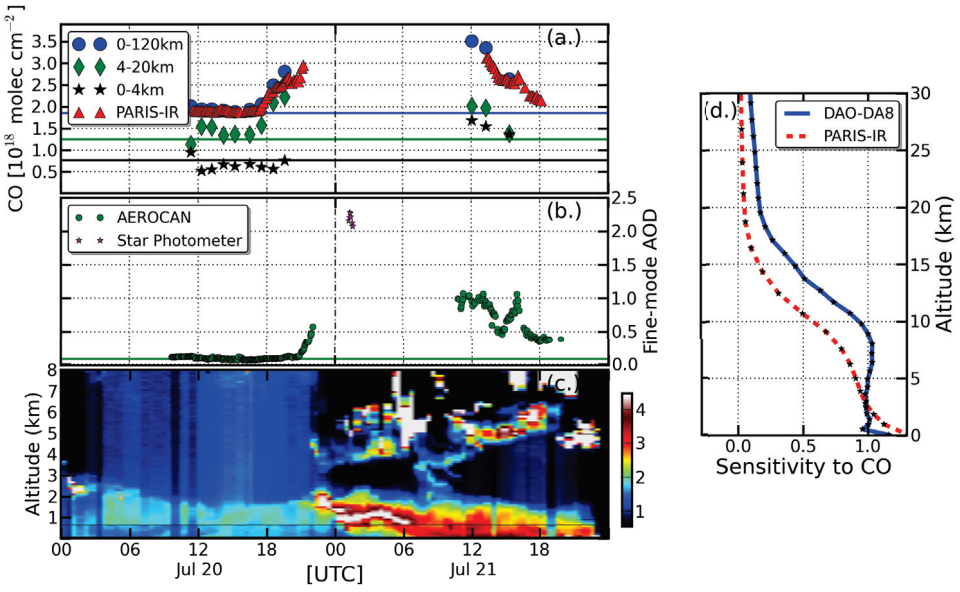

Figure 5.3: DGS observations of the 20–21 July biomass burning event. **(a)** Retrieved total and partial columns of CO (in molec cm^{-2}). Horizontal lines represent typical background total and partial columns of CO at DGS (0–4 km lowest, 4–20 km middle, total column upper). **(b)** Fine-mode AOD as measured by the sun and star photometers. The horizontal line represents the typical background fine-mode AOD at DGS. **(c)** DRL attenuated backscatter ratio showing vertical distribution of aerosols above DGS. **(d)** Sensitivity, as a function of altitude, of the PARIS-IR and DAO-DA8 retrievals of CO to the true profile rather than the a priori profile.

morning value of $(2.0\pm0.1)\times10^{18}$ molec cm^{-2} and reaches $(2.9\pm0.1)\times10^{18}$ molec cm^{-2} by 21:20 UTC (Fig. 5.3a). The enhancement appears to have continued throughout the night as a maximum value of $(3.5 \pm 0.1) \times 10^{18}$ molec cm^{-2} was measured on the morning of 21 July. Total column values then declined throughout the day, but the sun was obscured by clouds from 18:00 UTC on 21 July to sunset ($\sim$ 23:50 UTC) so there are no measurements in that period.

Figure 5.3b shows the derived fine mode AOD from the CIMEL sun photometer and star photometer throughout the event. The arrival of the plume is marked by a sudden increase in both the coarse and fine mode AOD around 20:30 UTC on 20 July. From a typical background value of 0.05, the fine mode AOD climbed to 0.6 in less than two hours before the sun set and continued to rise into the night when the star photometer measured a peak value of 2.3 at 01:30 UTC. The extreme optical depth of this event interfered with the star photometer's ability to properly focus on stars, and therefore permitted only a handful of star photometer measurements during the night. After sunrise on 21 July ($\sim$ 08:50 UTC) the sun photometer measured a fine mode AOD value of 1.0 that then declined throughout the day. Coarse mode AOD (not shown) associated with clouds begins to interfere with measurements by 18:00 UTC.

Of particular interest is the onset of the event. The higher spectral resolution of the DAO-DA8 enables us to retrieve partial columns of CO from our measurements. In addition to the total CO column from 0 to 120 km, Fig. 5.3a shows retrieved partial CO columns from 0 to 4 km, and from 4 to 20 km. Although the second partial column extends to 20 km, typical July tropopause heights above Halifax are closer to 12 km, resulting in a sensitivity to CO that is highest between 4 and 12 km. Lines representing typical background partial and total column values are also shown in Fig. 5.3a. There is some evidence of an enhancement of CO in the mid-upper troposphere column starting at 13:00 UTC on 20 July, although this is made uncertain by an absence of earlier measurements. Then, at 17:30 UTC, a clear signal of a significant mid-upper troposphere enhancement begins that is not observed in the lower column. This is in contrast to 21 July when we see strong enhancements in both the lower and upper tropospheric partial columns.

These 0 to 4 km partial CO column observations are in agreement with the vertically resolved DRL attenuated backscatter ratio shown in Fig. 5.3c. The

backscatter ratio is derived by comparing the measured lidar signal against a modelled aerosol-free atmosphere. No significant aerosol enhancement is seen on 20 July until around 22:00 UTC, at which point a strong signal appears and persists throughout 21 July. The DRL measurement ends at 22:00 UTC on 21 July when fog and rain moved over the DGS.

There is clear evidence for an enhancement of CO in the upper levels of the troposphere on 20 July $\sim$ 3 h ahead of the fine mode AOD increase, and some indications of a smaller increase $\sim$ 9 h ahead. These observations suggest the presence of a high-trace gas/low-particulate plume ahead of an additional plume with high levels of both particles and gases. One possible explanation for this observation involves a single plume that underwent a change in composition with time. Alternatively, these observations reflect the overlapping of two airmasses with different histories. We will distinguish between these possibilities using satellite and aircraft observations supplemented by atmospheric transport modelling.

5.4.2 Satellite and aircraft observations

It is important to interpret our column measurements from the DGS within the context of the larger regional picture. A variety of different satellite-derived atmospheric products are available with near-daily global coverage. Images gathered on 20 July by the MODIS instrument aboard the NASA Aqua platform (passing over the DGS at 17:50 UTC) show a region of low AOD over Nova Scotia with significant higher AODs to both the east and west of the region (Fig. 5.4). At the same time, the Atmospheric Infrared Sounder [AIRS; 83], also aboard Aqua, measured an enhanced total-column CO value of $(2.6 \pm 0.2) \times 10^{18}$ molec cm^{-2} over Halifax in agreement with the DAO-DA8 measurements. CO columns as high as 4.0×10^{18} molec cm^{-2} are seen approaching from the west. While the satellite measurements broadly support the DGS observations, they do not provide sufficient vertical information.

The BAe-146 ARA in-situ measurements gathered 800 km upwind of the DGS during flight #B622 on 20 July show that there were indeed two distinct plumes (in terms of gas and aerosol concentrations) moving toward Halifax. While flying west from northern New Brunswick, the ARA performed a sawtooth pattern of profile ascents/descents in advance of a cold front associated with a surface low.

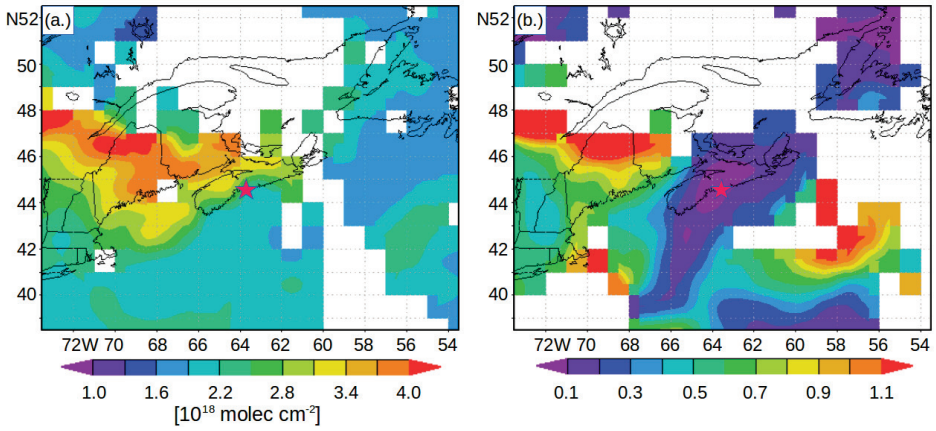

Figure 5.4: Satellite observations made during the 17:50 UTC ascending pass of Aqua over the DGS on 20 July 2011. **(a)** Total column CO measured by the AIRS instrument (Level 3 Daily standard physical retrieval V005) showing a large enhancement approaching the DGS (marked by star near center of plot). **(b)** Simultaneous 550 nm Aerosol Optical Depth as measured by the MODIS instrument showing a region of low-aerosol loading above the DGS. White regions indicate interference from clouds.

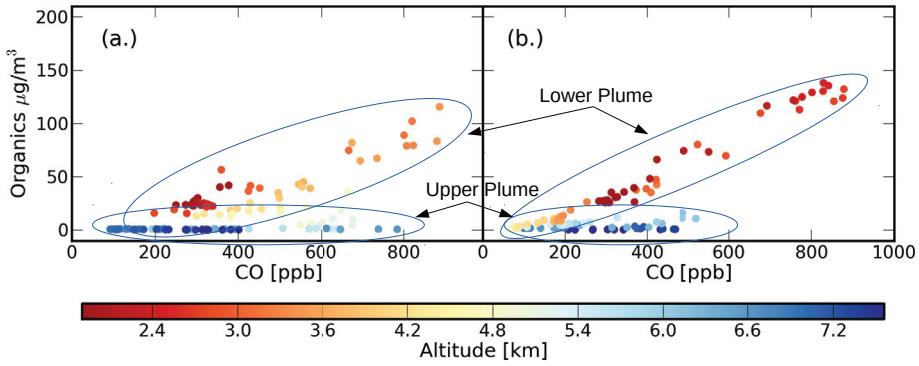

Figure 5.5: In-situ measurements of organic particulate mass plotted against CO as measured by instruments aboard the BAe-146 ARA during **(a)** an ascent, and **(b)** the subsequent descent on 20 July 2011 during flight #622. Exact locations of the profiles are given in the text and plotted in Fig. 5.6. Both profiles revealed the presence of two vertically separated plumes of CO, and that the upper plume contained little or no organics.

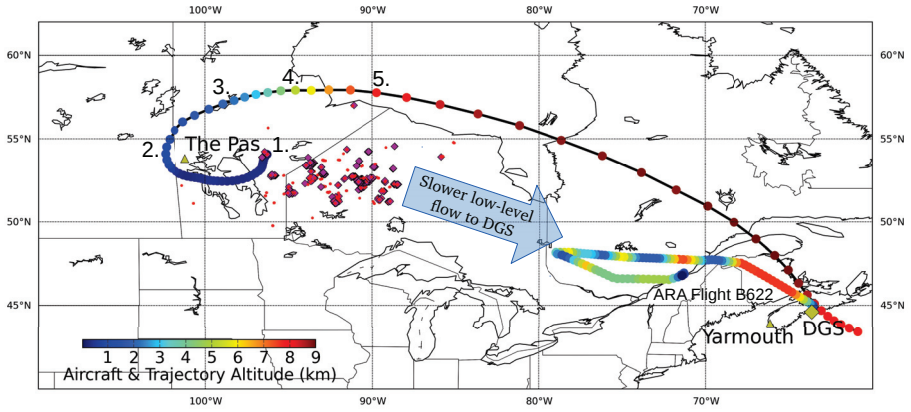

Figure 5.6: Representative upper plume trajectory from the HYSPLIT model. Particles were released at 18:00 UTC on 17 July 2011 from 54.07° N, 96.30° W. Also shown is the flight path of the ARA during flight B622 on 20 July 2011. Plume and aircraft altitudes are reflected by the marker colors. See text for details of plume transport at numbered positions.

Figure 5.5a shows the concentration of organic aerosols (μg m^{-3}, as measured by the onboard AMS) plotted against CO (ppbv) for an ascent that began at 16:11 UTC at a position of 47.7° N, 70.0° W, at an altitude of 1.9 km and ended at 47.8° N, 71.5° W, at an altitude of 7.5 km. Two distinct plumes of elevated CO are clearly visible in the data: a low altitude layer between 3 and 4 km, and a thinner layer above at an altitude of 6.5 km. There is a clear relationship between CO and organics in the lower plume, while the upper plume of CO shows little enhancement in organic material. The aircraft then descended to a position of 47.8° N, 72.8° W, at an altitude of 1.9 km and measured a similar pattern of two vertically distinct plumes of CO with drastically different organic aerosol loadings (Fig. 5.5b). The full track of flight #B622 is shown in Fig. 5.6.

The contrast of elevated CO concentrations and elevated organic aerosol mass in the lower plume vs. elevated CO concentrations and low organic aerosol mass in the upper plume support the theory that the two plumes followed different paths with different histories, and that the upper plume may have experienced a lofting event coupled with removal of the aerosol mass. The ARA measurements are geographically and temporarily separated from the DGS observations, yet reflect the regional presence of vertically separated biomass burning plumes. While we use the ARA flight #B622

measurements simply to support our theory of two vertically separated plumes, Taylor et al. [79] perform a full analysis of aerosol properties measured in the different plumes aboard the ARA.

5.4.3 Trajectory analysis

The HYSPLIT dispersion model was used to locate a probable origin of the two plumes intercepted by the DGS remote sensing instruments. The backwards trajectory for the lower particle-rich plume was initialized at 00:00 UTC 21 July 2011 with an even distribution of particles between 0.5 and 1.5 km to match the observations made by the DRL (Fig. 5.3c). The backwards trajectory of the upper-troposphere particle-poor plume was more sensitive to starting times and so a series of runs were performed with releases ranging from 14:00 to 19:00 UTC. Although the best timing with DAO-DA8 measurements did not show strong vertical motions, backwards trajectories with small changes in start time exhibited rapid lofting of the airmass $\sim$ 24 hours before detection at the DGS. Considering the coarse grid of the NCEP GDAS meteorology used to advect the particles, we believe that 15:00 UTC on 20 July is an acceptable initialization time for modeling the upper-troposphere plume. An even distribution of particles between 7.0 and 9.0 km was used to match the center of the CO sensitivity of the DAO-DA8's upper partial column. Both backwards trajectories were started above the DGS, and run for 84 h. No deposition or chemical evolution was considered in these models.

The HYSPLIT model shows that the majority of the lower plume remained in the lowest 3 km of the atmosphere throughout the modelled time, and the footprint at -84 h covers the region of fires in northwestern Ontario (Fig. 5.7). This is in contrast to the upper plume that is shown to have approached from southern Hudson Bay after undergoing a period of intense lofting. This lofting is clearly visible in the HYSPLIT dispersion model time step shown in Fig. 5.8. The resulting footprint from the upper plume suggests that there was little or no contribution from the main Ontario fires, but a possible contribution from the region of Lake Winnipeg in Manitoba on 17 July.

Possible fires in this area were identified using MODIS fire counts from NASA FIRMS. Mid July conditions in eastern Manitoba were hot and dry with a ridge of high pressure settled over the region. On 16 July, the MODIS instruments aboard

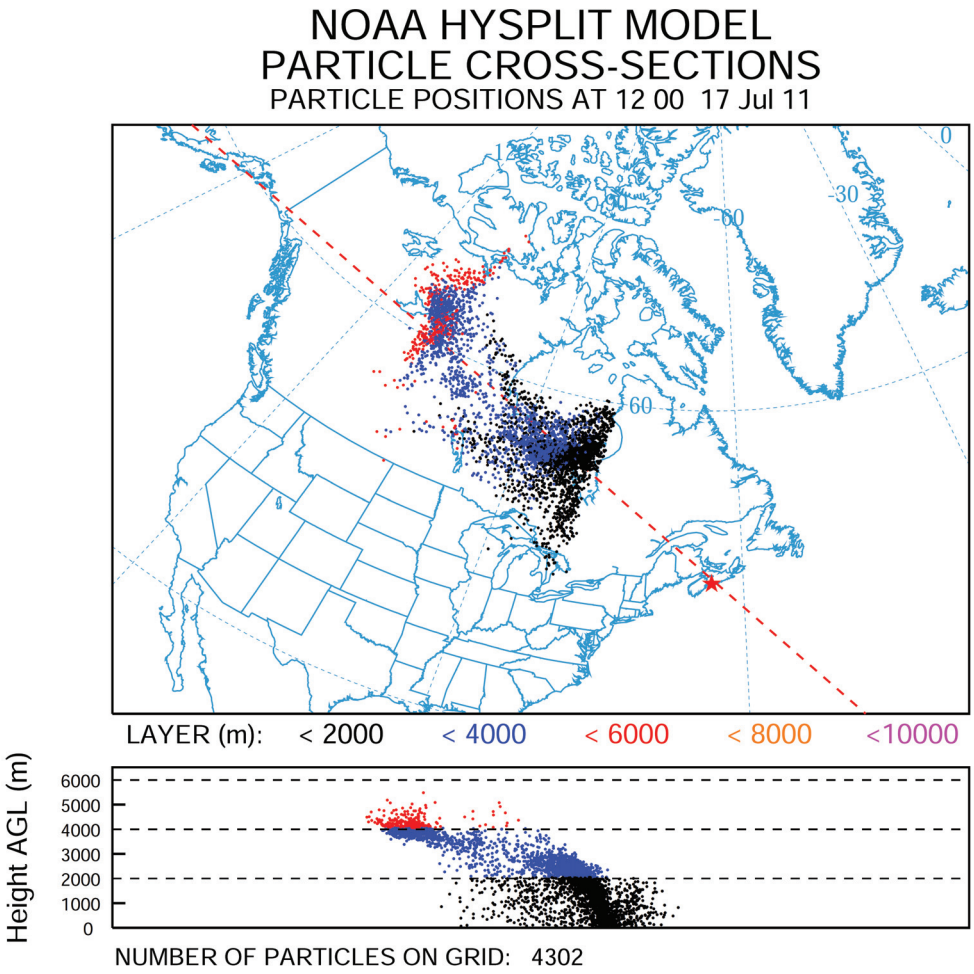

Figure 5.7: HYSPLIT dispersion model showing location contributions to the lower plume of trace gas and aerosols observed at 00:00 UTC from the DGS on 21 July 2011. Particles were initialized between 0.5 and 1.5 km above the DGS (marked by red star) and advected back by 84 h. A significant overlap is observed between the model footprint and regions of wildland fires in western Ontario (see Fig. 5.6). The lower panel shows the vertical distribution of particles along the red dashed line in the upper panel with the majority of the particles still in the lowest 4 km of the atmosphere.

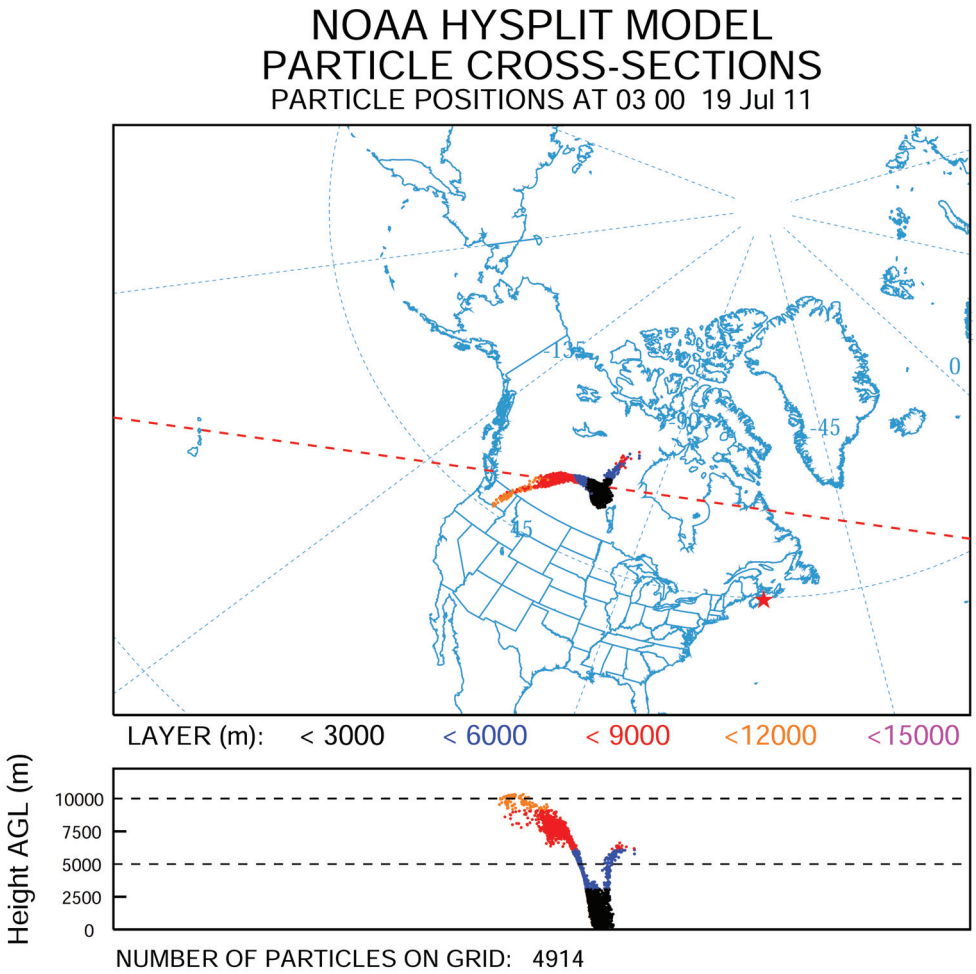

Figure 5.8: HYSPLIT dispersion model showing location contributions to the upper plume of trace gas observed at 15:00 UTC from the DGS on 20 July 2011. Particles were initialized between 7.0 and 9.0 km above the DGS (marked by red star) and advected back by 36 h. Contributions from below 4.0 km ($\sim 70\,\%$ of particles released) are concentrated at the border of Manitoba and Saskatchewan in the region where reports of smoke were observed. This time step corresponds to Position 2. in Fig. 5.6. The lower panel shows the vertical distribution of particles along the red dashed line in the upper panel.

Aqua and Terra first detected fires in the region northeast of Lake Winnipeg. Many of these fires significantly expanded in both size and intensity over the next 24 h, and the largest continued to burn until being extinguished by rainfall on 19 July. This general region (Position 1. Fig. 5.6) was used to initialize a more detailed FLEXPART forward trajectory. Both HYSPLIT and FLEXPART indicate that the plume remained within the boundary layer for almost 24 h where it was influenced by easterly winds which carried it away from the Ontario fires and toward the Saskatchewan border. Figure 5.6 shows a single HYSPLIT trajectory that is representative of the full FLEXPART results. It is important to recognize that these models are not well suited to accurately describe transport within the boundary layer. However, there is a general agreement between the models that the airmass west of The Pas, Manitoba (53.8° N, 101.2° W) underwent $\sim$ 18 h of moderate to strong vertical ascent.

FLEXPART results suggest that dispersion by the vertical wind shear during the dynamic lofting between Positions 3 and 5 in Fig. 5.6 significantly lowered the CO and aerosol concentrations within the plume. Additional FLEXPART runs using particles susceptible to removal via wet-deposition show a further loss in particle concentrations during the lofting phase. The now particle-poor plume eventually reached 8 km where it was quickly transported toward Halifax via a strong west-northwest flow driven by an upper level low over northeast Hudson Bay.

5.5 Evidence of precipitation

The HYSPLIT model tracks rainfall along trajectories using information from the NCEP GDAS reanalysis and shows that the upper plume passed through a broad region of precipitation in northern Manitoba with rainfall rates of 5 to 7 $\mathrm{mm\,h^{-1}}$ (Fig. 5.9). A similar analysis shows that the lower particle-rich plume did not encounter any precipitation during transport to the DGS. Very few ground station measurements exist in northern Manitoba to confirm this precipitation reanalysis, and the region is beyond the range of the nearest radar station. However, a number of pieces of information combine to provide evidence for this lofting event.

First, surface analysis charts of this region provided by the Winnipeg Storm Prediction centre (Environment Canada) show the passage of a small area of low pressure early on 19 July. Station pressure at The Pas, Manitoba, began falling

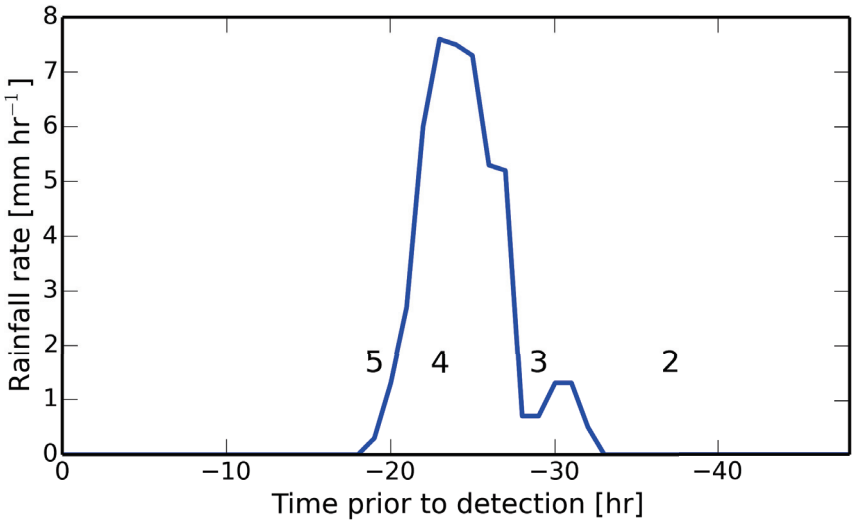

Figure 5.9: Precipitation rates along the HYSPLIT trajectory shown in Fig. 6 for the upper, potentially scavenged, airmass. The rainfall information was derived using the NCEP GDAS reanalysis. Time on the horizontal axis is measured in hours prior to detection of the airmass at the DGS. Numbers correspond to HYSPLIT positions marked in Fig. 5.6. The same analysis applied to the trajectories for the lower particle-rich plume does not show any significant precipitation along the path (not shown).

around 18:00 UTC on 18 July under mostly cloudy skies. The sounding released from The Pas at 00:00 UTC 19 July shows an atmosphere that was conditionally unstable above 2 km. The Pas weather observations recorded a temperature of 26 °C and reported smoke that lowered the visibility below 10 km. Thus, the conditions were in place for the initial lofting of the biomass burning plume.

Second, although radar data is unavailable along the plume trajectory, the radar stations farther to the west in Saskatchewan and Alberta (see Fig. 5.1) detected the initial precipitation from a forming mesoscale convective system (historical radar data taken from National Climate Data and Information Archive, Canada). At 00:00 UTC on 19 July a line of thunderstorms, oriented north-south, formed along an advancing cold front south of Edmonton, AB, and bloomed in size and intensity while travelling east. The system crossed the western border of Saskatchewan around 04:00 UTC 19 July.

Finally, high numbers of lightning strikes associated with this system were detected

by the Canadian Lightning Detection Network [84]. Thunderstorms were observed at The Pas between 07:00 and 09:00 UTC, and a total rainfall of 11.4 mm was recorded during this event. Other regional stations reported rainfalls between 10 and 20 mm, and a number of significant weather events were noted in the region including hail with diameters in excess of 6 cm.

Thus, despite the remote location with its sparse observing network, it is clear that a convective event with moderate to heavy rainfall transited northern Manitoba early on 19 July. The correlation between this rainfall and the trajectory analysis described above supports the theory that some biomass burning plumes in eastern Manitoba experienced a period of precipitation scavenging while being lofted to the upper troposphere.

Chapter 6

Three years of observations at the Dalhousie Atmospheric Observatory

The DAO-DA8 began regular solar absorption measurements in late June 2011. This chapter discusses measurements made up to mid September 2014 when a dome failure caused damage to the CST and transfer optics. I begin with an explanation of how the measurements were gathered, and follow with a discussion of a few alignment issues that must be considered in our analaysis. I then introduce the retrieval process before presenting the full time series including details of the analysis and a discussion of the results. Over the course of these three years a variety of improvements were made to the system, most notably upgrades to the CST described in Ch. 4. The spectrometer was also realigned multiple times during the time series, and measurement procedures varied. These changes need to be considered when processing the entire data set. In addition to these physical changes to the system, we also upgraded the trace gas analysis software during the final year of work.

6.1 Data Gathering

Some fields of study allow for the careful design and implementation of a controlled experiment which can then be repeated as needed. The study of atmospheric processes is not such a field. Despite improvements in forecasting, interesting air masses are usually discovered only upon the analysis of data that has already been gathered. With this fact in mind, measurements were conducted at the DAO on most sunny days throughout the years, regardless of weekends and many holidays.

As described in Ch. 3, the DAO-DA8 became more autonomous over the 3 years of measurement, but always required an operator on site at start up for initialization tasks. Therefore, I am thankful that I had a series of summer students (and even the occasional co-op student during regular term) to aid me with these observations. Morning duties consist of initializing active solar tracking using the CST, cooling

the detectors with LN_2, and, once the internal HeNe laser has stabilized, starting an observing macro designed to cycle through the 6 individual narrow-band filters.

From June 2011 to March 2013 all filters were used with a complete filter cycle requiring approximately one hour. Thus, any trace gas species being retrieved from a given narrow region of the solar spectrum would be observed with a temporal resolution of one hour. Starting in April 2013 the MCT detector began exhibiting increased noise, and measurements were no longer consistently made using filters 5 and 6. Unfortunately, alignment issues became more severe in late 2013, and without an automated iris, insufficient light was reaching the InSb detector during measurements made through filters 1 and 2. Starting in 2014, the decision was made to prioritize greater temporal resolution of a select number of species associated with biomass burning events, and most observing days consisted of switching between filters 3 and 4. Efforts were actively underway to correct the system alignment and reintroduce all filters when the dome failure caused all measurements to cease in September 2014. The system is currently being upgraded to include the new 24-bit DAQ discussed briefly in §3.2.3 and will return to active duty in 2016.

One inconsistency in the data set is the travel speed of the scanning mirror. Faster scanning speeds allow greater temporal resolution, but this comes at the trade off of increased noise as the dynamic alignment system struggles to keep pace. The scanning mirror speed was varied during the initial year of measurements as we continued to learn the system, but 1.5 cm s^{-1} was a typical speed until January 2013 when the DA8 was operated for several months with a scanning mirror speed of 3 cm s^{-1}. This speed was excessive and led to a dramatic increase in noise, and in June 2013 the scanning mirror was once again slowed to 1.5 cm s^{-1} through to the end of the data set presented here.

6.2 Instrument Line Shape

In §3.4.3 I briefly described a method for quantifying the ILS of a FTS using a gas cell containing HBr at low pressure. This procedure was implemented at the DAO on a semi-regular basis using the internal MIR source as a background signal. In a typical ILS test, two sets of ∼50 full-resolution scans were gathered using the KBr beamsplitter and InSb detector. The MIR source was measured directly in the first

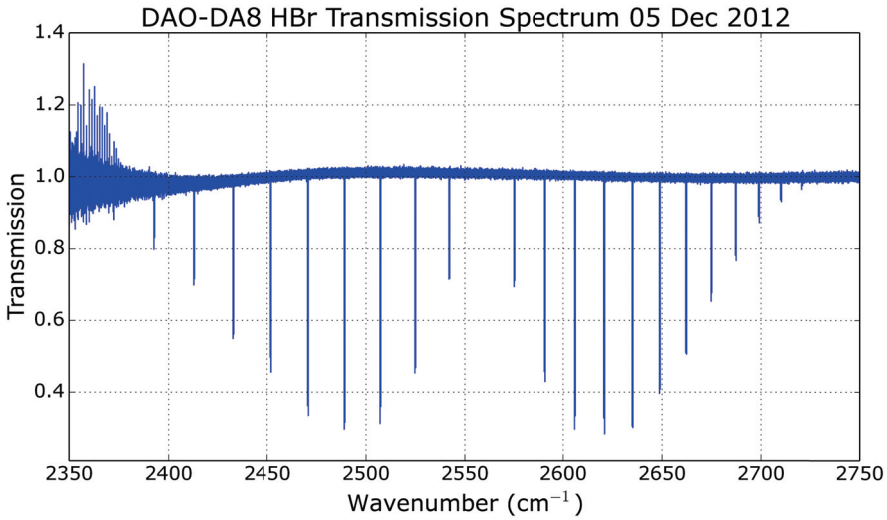

Figure 6.1: Transmission Spectrum of HBr cell #41 on 05 December 2012 revealing the vibration-rotation (0-1) lines used to determine the ILS of the DAO-DA8. Increased noise at lower wavenumbers is the result of low signal near the spectral edge of an optical filter.

set before introducing the HBr cell into the optical path for the second set, enabling us to create a transmission spectrum of the HBr gas (Fig. 6.1). A narrow band filter (NDACC F3; see Table 3.1) was placed in the sample compartment to limit the wavenumber range of the measurement and assure that the detector was the dominant source of noise. The increased noise below 2450 cm^{-1} in Fig. 6.1 is the result of observing near the edge of the filter.

The software package LINEFIT [v.12; 38] introduced in §3.4.3 was then used to fit a series of individual absorption features and retrieve the ILS. Results from three ILS tests performed in late 2012 and mid 2013 are shown in Fig. 6.2. The test in November 2012 (red dots) revealed an ILS that deviated significantly from the ideal sinc function expected for a perfectly aligned FTS. Figure 6.3 shows the modulation efficiency, or the attenuation of the signal, as a function of OPD, as well as the phase error which is a measure of the asymmetry of the ILS. An ideal ILS has a modulation efficiency of one and a negligible phase error at all values of OPD. The poor November results prompted me to realign the DAO-DA8, and a new ILS test was performed on 05 December 2012 (black dashes) showing a significant improvement. Unfortunately, this improvement was short-lived as a new ILS test in June 2013 (blue line) revealed

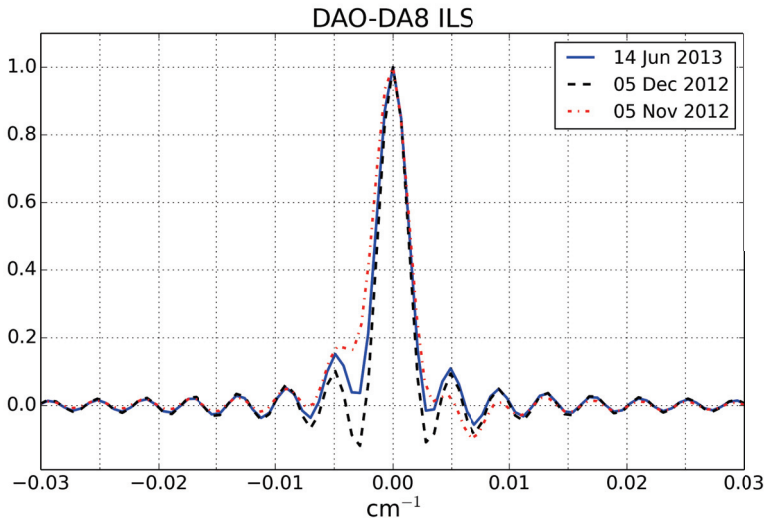

Figure 6.2: Normalized ILS results from late 2012 and 2013 showing the improvement and subsequent deterioration of the DAO-DA8 alignment.

another significant drop in modulation efficiency.

One significant weakness in the ILS test described above is the use of the internal MIR source as a background signal. To direct the light into the interferometer the folding mirror must be shifted into its alternate position (Fig. 3.3). It is possible that this change in the optical path might alter the response function of the spectrometer. An external MIR source could be used in place of the internal source, but this experiment was never attempted at the DAO. Instead, during the fall of 2013 we attempted to characterize the true ILS by keeping the HBr cell in the sample chamber during regular solar measurements. While HBr is not present in observable quantities in the atmosphere, other nearby absorption lines sometimes interfered with LINEFIT, and it was necessary to limit which vibration-rotation lines were used in the analysis. Even with this limitation we were able to successfully retrieve the ILS from regular solar measurements. However, regular atmospheric measurements only average four scans (rather than the $\sim$50 used in ILS tests) leading to increased noise in the transmission spectra. This noise was carried through to the retrieved ILS, and after a few weeks of tests we removed the HBr cell from the optical path.

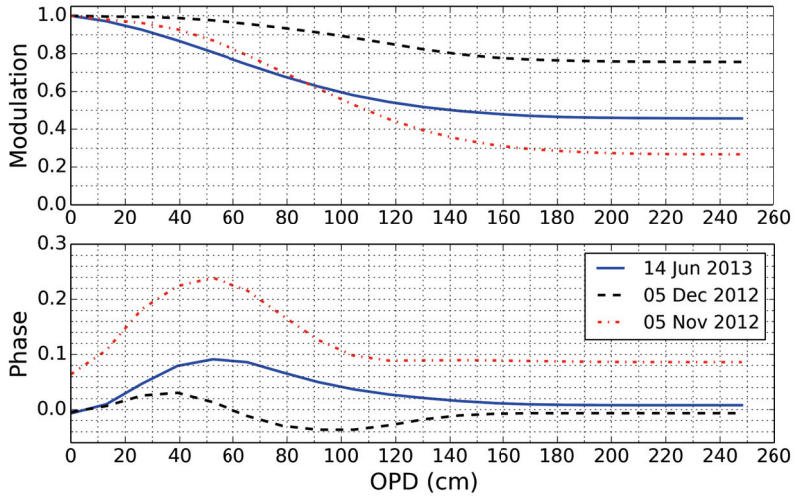

Figure 6.3: Modulation efficiency (top) and phase errors (bottom) in the DAO-DA8 ILS in late 2012 and 2013.

6.3 Channeling

The successful conversion of our measured IGMs into solar spectra is predicated on precise knowledge of the OPD at a given datapoint. While the impact of a slight misalignment and a finite FOV can be accounted for by quantifying the ILS of the FTS and including the information within the retrieval process, undesirable reflections in the optical path can produce additional spectral features. These reflections can occur within the beamsplitter, or while passing through any filters or windows along the optical path. Since a portion of the input energy now follows a different path length to the detector, these reflections can create a false ZPD to occur at a non-zero OPD (Fig. 6.4). During the Fourier transform, this false ZPD is transformed into a strong cosine wave that overlays the entire solar spectrum (Fig. 6.5b).

Efforts to identify the source of the channeling within the DAO-DA8 have so far been unsuccessful. As many observations already suffer from its presence, it became important to develop methods to counter the effect of the channeling on our spectra. One possible correction method is to model the channeling as an instrumental effect within the forward model of the retrieval. Another option is to attempt to alter the IGM itself before the transformation. As the channeling at the DAO has not been consistent, we decided to attempt the second method by replacing a small portion of

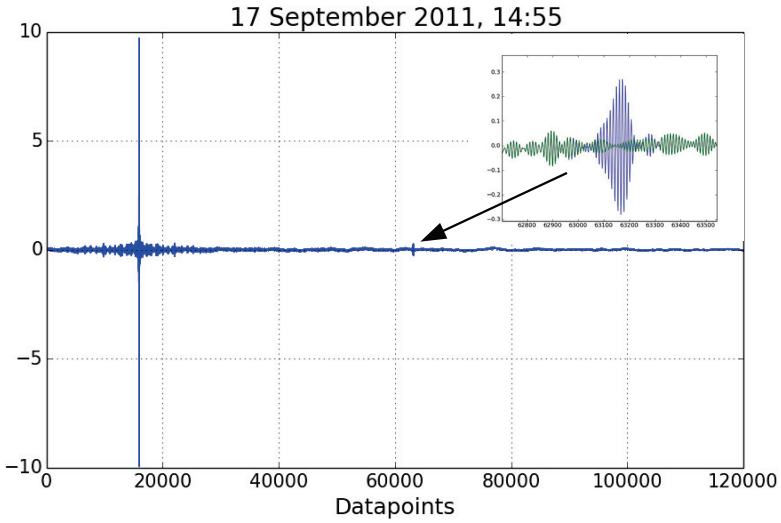

Figure 6.4: A small portion of a DAO-DA8 IGM from 17 September 2011 showing the true ZPD burst and an additional false ZPD caused by channeling. Inset shows detail of the false ZPD and a correction.

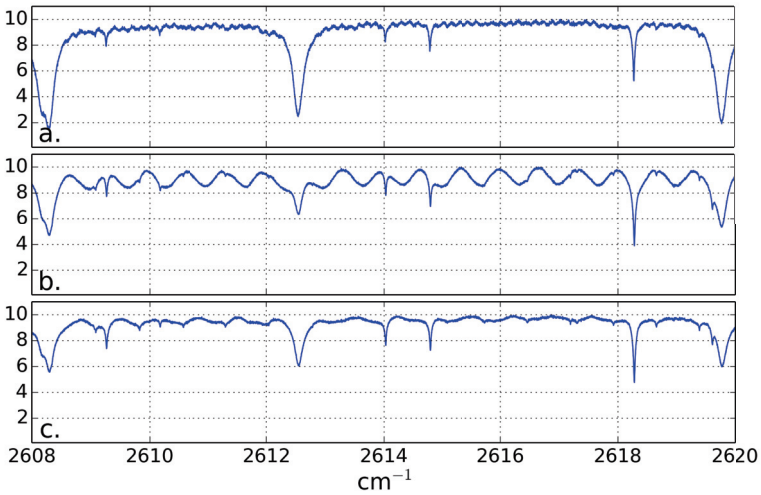

Figure 6.5: The impact of channeling on the solar spectrum. **(a)** An example of minor channeling from 05 July 2011. **(b)** The same spectral region on 17 September 2011 showing significant channeling which disrupts two CH_4 absorption lines at 2614.1 and 2614.8 cm^{-1}. **(c)** Same spectrum as (b) after applying the correction shown in Fig. 6.4.

the observed IGM with data gathered through the same filter when channeling was not present. The inset of Fig. 6.4 shows an example of this replacement, and similar corrections are made for all filters.

Figure 6.5 demonstrates the importance of correcting for channeling before performing trace gas retrievals. While the minimal channeling seen in Fig. 6.5a will have some impact on the results, more extreme cases such as Fig. 6.5b will often cause the retrieval to completely fail. The residuals seen in Fig.6.5c show that our correction method is not perfect, and these artifacts lead to increased scatter in the CH_4 results that I will present in §6.5.

6.4 Trace gas retrievals

Trace gas columns at the DAO are derived from the calculated solar spectra using an optimal estimation method [OEM; 30, 31] as implemented by SFIT, a retrieval software package widely used by the NDACC-IRWG. Through the summer of 2014 all spectra were processed using SFIT2 version 3.94c [70, 71]. This version of SFIT has been rigorously compared to an independently developed OEM retrieval software package [85]. At the DAO, we dedicated a significant effort to the development of software to properly pass our data into the core of the SFIT2 code.

Then, in 2014, a new version of SFIT was released under the name SFIT4 (https://wiki.ucar.edu/display/sfit4). Unfortunately, the input mechanisms of the code were altered enough to nullify much of the wrapper work I had invested into running SFIT2 which had to be modified for the new software. However, this disappointment was tempered by the inclusion of an inline error analysis code. The results presented in this chapter were processed using SFIT4 version 0.9.4.4.

SFIT4 begins the retrieval process by creating a modelled atmosphere based on assumed VMR profiles of trace gases, and knowledge of the temperature and pressure profiles. This model is used by a ray tracing program to calculate a synthetic absorption spectrum that can be compared to the observed spectrum. Based on the residuals of the spectral fittings, SFIT4 then modifies the modelled atmosphere via the OEM method described in §2.4, and the process is iterated until no further reduction in residuals obtained.

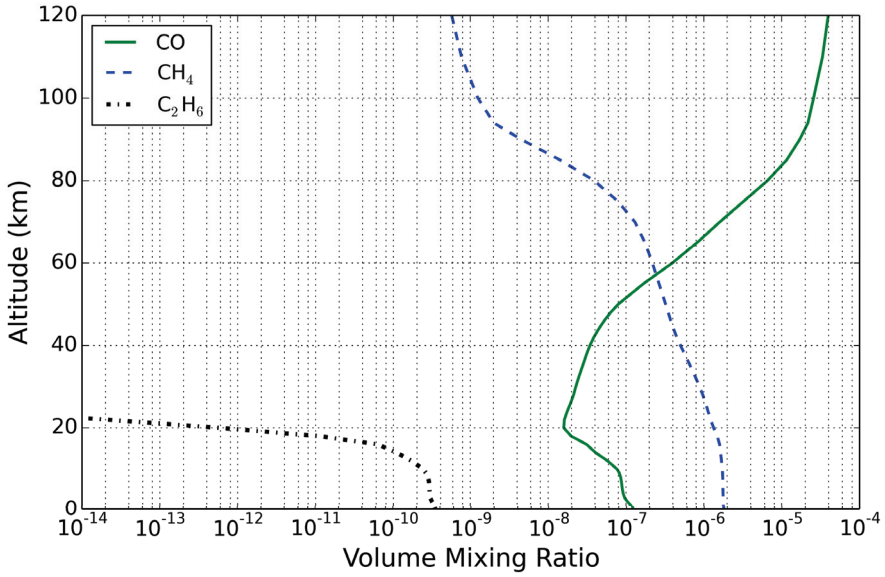

Figure 6.6: Initial VMR profiles for CO, CH_4, and C_2H_6 taken from the 40 yr averages of the WACCM model over Halifax, NS. The VMR of C_2H_6 drops to negligible values above 25 km and is therefore not shown.

6.4.1 Ancillary data

A significant task was to determine appropriate parameters and ancillary data with which to drive the DAO-DA8 trace gas retrievals. Here I will focus on the three species introduced in Ch. 2: carbon monoxide (CO), methane (CH_4), and ethane (C_2H_6). CO and C_2H_6 were chosen as typical tracers of biomass burning events in the Canadian boreal forest. Another typical biomass burning tracer, hydrogen cyanide (HCN), was not retrieved in this work due to spectral interference by the significant water columns that exist in the maritime environment of Halifax, NS.

We use a forward model at the DAO that operates on a 48-level altitude grid starting at 65 m and reaching to 120 km. All ancillary data used must be interpolated onto this same grid. Figure 6.6 shows the a priori VMR profiles used for our three target species. These profiles were taken from 40 yr averages (1980–2020) of the Whole Atmosphere Climate Chemistry Model (WACCM V6) sampled over Halifax [73]. While C_2H_6 VMRs fall off precipitously above ∼15 km, CO VMRs actually increase with the oxidation of CH_4 as the primary source [86].

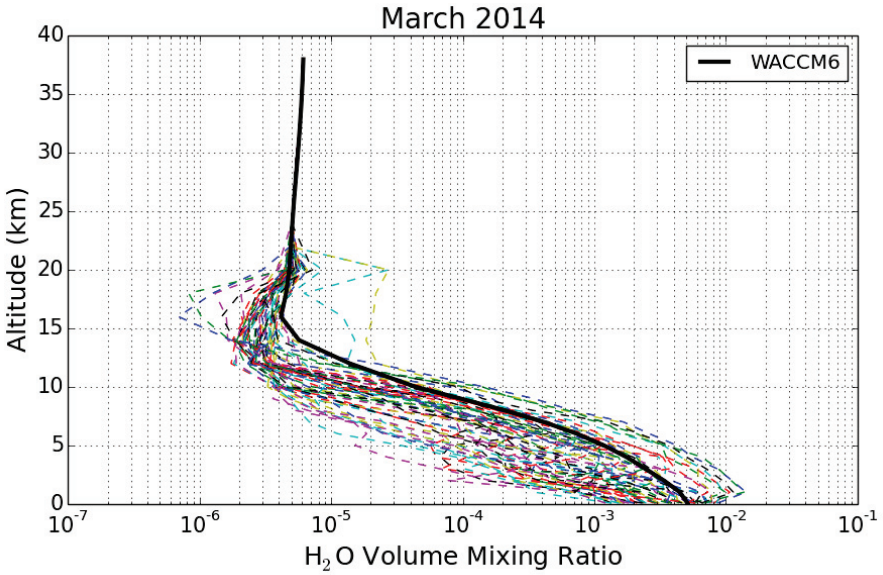

Figure 6.7: H_2O VMR profiles derived from radio sonde measurements over DAO in March 2014 compared to WACCM 40 yr March average.

Identifying proper a priori information for water vapour profiles is more challenging for the maritime environment of Nova Scotia where H_2O VMRs can vary by an order of magnitude on daily timescales. Some sites handle this variation by performing a "two-step" retrieval whereby the water vapour profile is first retrieved on the full grid and then entered as an a priori value when retrieving the desired trace gas. At the DAO, we have instead elected to use daily radio sonde measurements to provide reasonable a priori profiles that can then be scaled during the retrieval.

As in Ch. 5, we use the relative humidity and temperature information gathered by the daily radio sondes released from Yarmouth, NS (43.9° N, 66.1° W, 9 m a.s.l.) to calculate the H_2O VMR profiles. The values from a given measurement can show significant vertical structure and to avoid numerical issues in the retrieval it is necessary to strongly smooth the profiles as they are interpolated onto the DAO forward model altitude grid. The radio sondes only provide information in the lower atmosphere, and so we still rely on WACCM results above 25 km. However, rather than use a yearly average profile as for other species, we use monthly H_2O averages from the 40 yr data set. Fig. 6.7 demonstrates the variable nature of water vapour above Halifax in March 2014 as well as the March mean from the WACCM model.

Target gas	Microwindow (cm^{-1})	Interfering species
CO	2057.684-2058.000	H_2O, O_3,
	2069.560-2069.760	OCS, CO_2,
	2157.507-2159.144	N_2O
C_2H_6	2976.660-2976.950	H_2O, O_3
	2983.200-2983.550	
	2986.500-2986.950	
CH_4	2613.700-2615.400	HDO, CO_2,
	2835.500-2835.800	H_2O, NO_2
	2921.000-2921.600	

Table 6.1: Microwindows used in the retrievals of CO, C_2H_6, and CH_4, as well as the interfering species that must be simultaneously fit.

Pressure and temperature information is also required when performing the retrievals, and these data were taken from the National Centers for Environmental Prediction (NCEP) each day and interpolated onto the appropriate altitude grid.

6.4.2 Spectral regions and retrieval parameters

The microwindows used during the retrievals presented in this thesis were chosen based on the recommendations of the NDACC IRWG (Table 6.1). The use of multiple windows containing absorption features of varying strengths has been shown to increase the degrees of freedom for signal (DOFS) of the retrieval [32]. SFIT4 uses temperature and pressure dependant spectral information from the High-Resolution Transmission Molecular Absorption Database (HITRAN) 2008 line list [72], and assumes a Voigt line shape when calculating the simulated absorption spectra.

Other instrument parameters, including the resolution and field of view of the spectrometer, are also considered in the forward model as they will modify the calculated spectrum as shown in §3.1.3.

Figures 6.8, 6.9, and 6.10 show typical examples of the spectral calculation compared to observations. The influence of water vapour absorption is clearly seen in almost every window. The residuals seen in the CH_4 window are extreme and show structure that suggests our channeling correction of §6.3 is insufficient.

To perform the retrieval we must also determine values for the measurement error covariance matrix, $\mathbf{S}_\varepsilon$, as well as the a priori covariance matrix, $\mathbf{S}_a$, that together

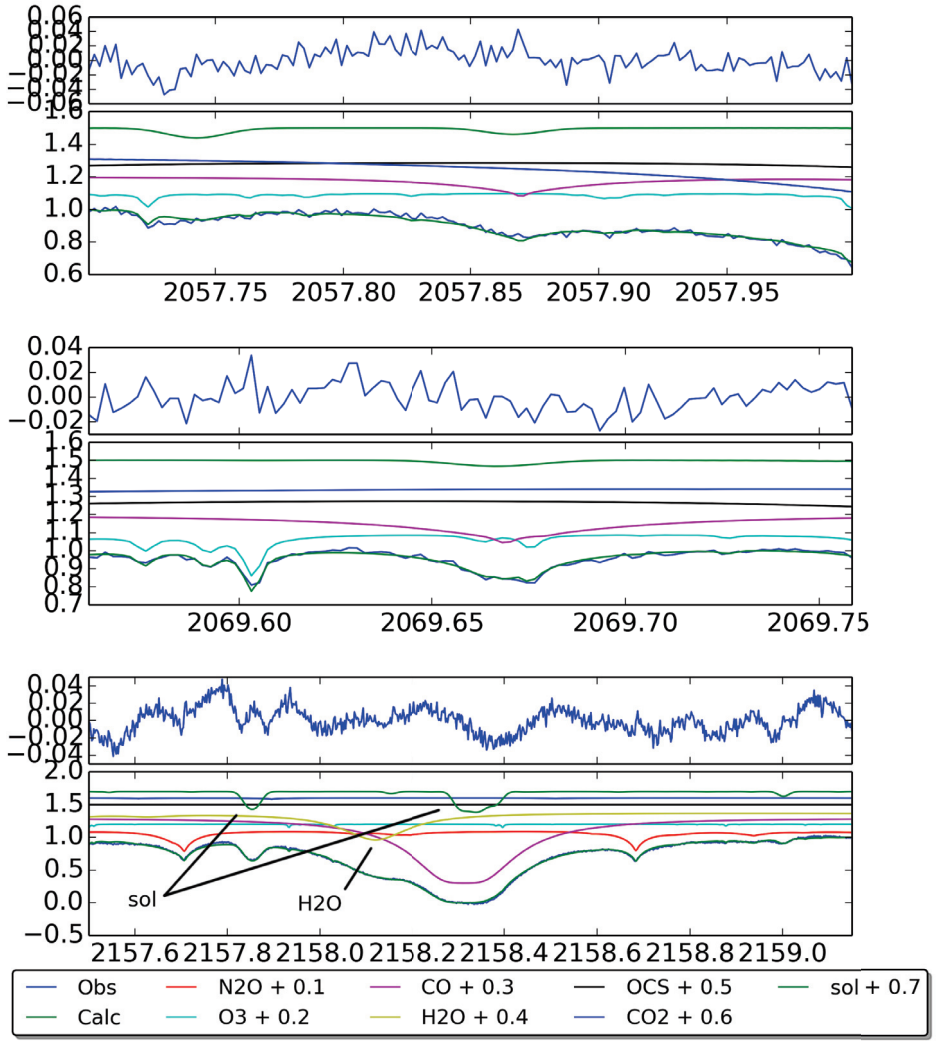

Figure 6.8: Microwindows used in the retrieval of CO showing spectral contributions of all major interfering species. Note the strong impact of water vapour in the third window, as well as the presence of solar lines.

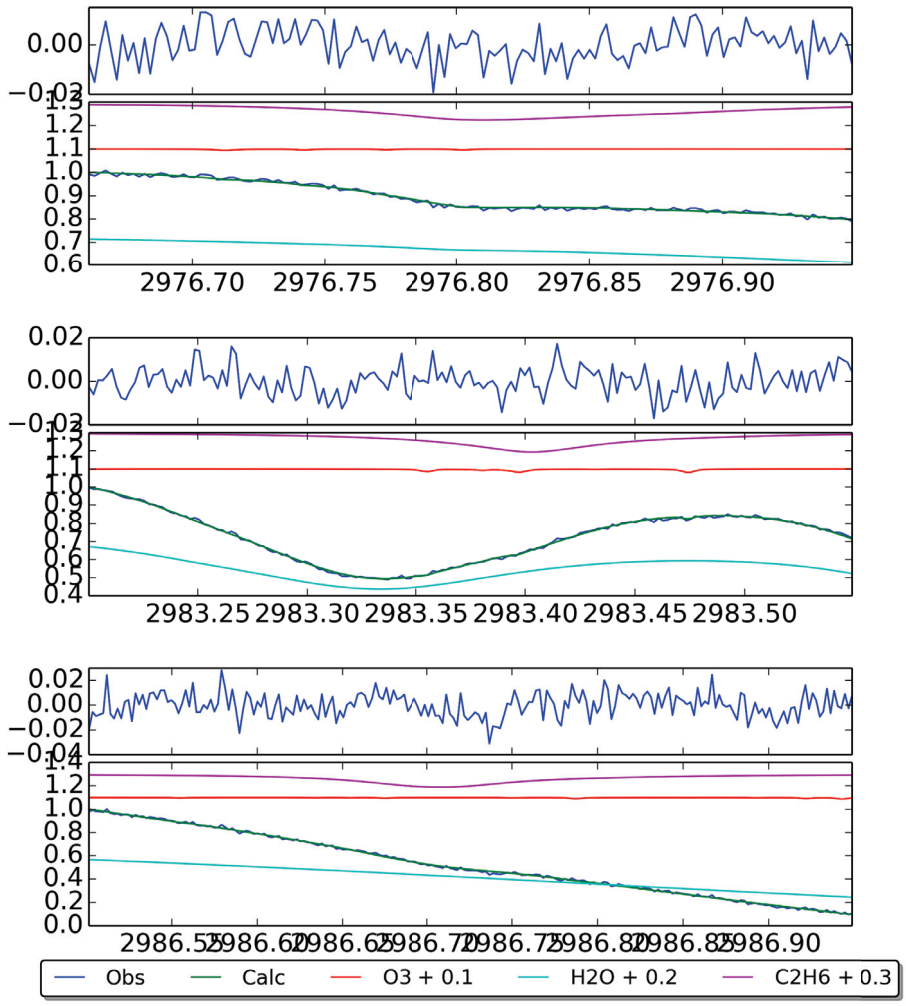

Figure 6.9: Microwindows used in the retrieval of C_2H_6 showing spectral contributions of all major interfering species

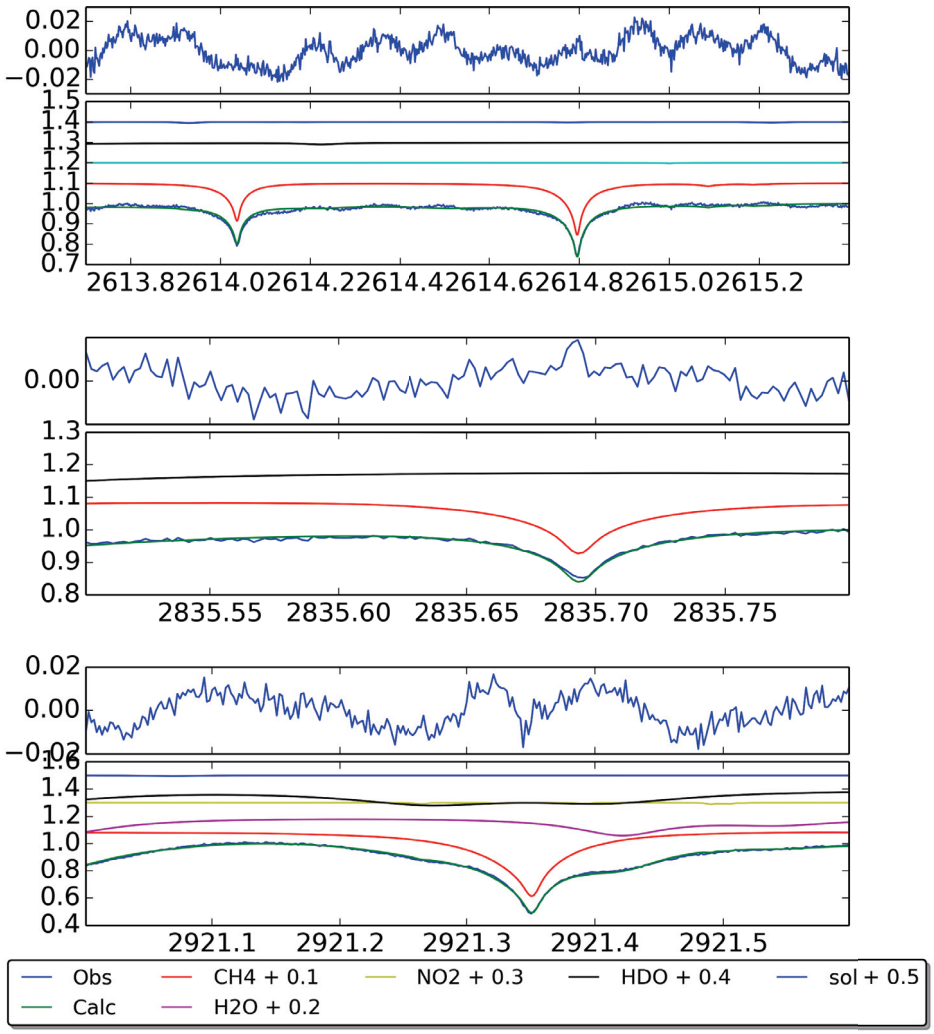

Figure 6.10: Microwindows used in the retrieval of CH_4 showing spectral contributions of all major interfering species. The residuals show significant structure that is primarily caused by not fully accounting for the channeling discussed in §6.3

define the gain matrix, $\mathbf{G}$ of Eq. 2.20. Typically, $\mathbf{S}_\varepsilon$ is represented as a diagonal matrix (signifying measurement errors that are uncorrelated) with each element set to the inverse of the signal to noise ratio (SNR) squared. In Ch. 5 we defined a single SNR to be used for every retrieval of a given trace gas using the "trade-off curve" method described by Batchelor et al. [48]. SFIT4 instead uses the true SNR value for each spectrum to define an individual $\mathbf{S}_\varepsilon$ that more accurately represents the measurement errors. To form the a priori covariance matrix, $\mathbf{S}_a$, we need to have some knowledge of the true variability of the trace gas above Halifax. Accurate information is hard to obtain, but we can derive estimates based on the modelled variability seen in the WACCM data. In practice, the values of $\mathbf{S}_a$ were varied from initial estimates to balance between providing enough flexibility for the retrieval to detect strong trace gas enhancements associated with pollution events and providing enough stabilization to prevent non-physical oscillations in the retrieved profile.

In §6.5.4 I will demonstrate how the choice of $\mathbf{S}_a$ and $\mathbf{S}_\varepsilon$ affect the error budget of the entire retrieval. However, having a sense of the errors is helpful when considering the results of the trace gas retrievals presented in the following section. Therefore I present the final results of the error analysis here in Table 6.2 without explanation.

6.5 Trace gas results

6.5.1 Carbon monoxide

Typical diagonal $\mathbf{S}_a$ values for CO used by other mid-latitude FTS observatories are on the order of 20%. However, at the DAO we have discovered that these values result in a strong oscillation in the CO VMR profile in lowest layers of the atmosphere, and in the presence of an elevated plume of CO can cause the lowest altitude bin to become negative. Therefore we have chosen to restrict the retrieval by lowering the uncertainty associated with the a priori profile to 10%. We also allow for correlations between different heights in $\mathbf{S}_a$ by assuming a Gaussian shaped covariance with a correlation length of 4 km.

The decision to reduce the uncertainty in the a priori results in a smaller retrieved DOFS compared to the SFIT2 retrievals performed in Ch. 5 (1.5 vs 2.4), and so only total columns will be presented in this chapter. Total column values are calculated

Error budget (%)	CO	C_2H_6	CH_4
N spectra retrieved in time series	2870	3024	3439
DOFS	1.5	1.2	1.2
Random errors			
Measurement error	0.4	1.7	0.3
Uncertainty regarding temperature	0.6	0.4	0.4
Uncertainty regarding retrieval parameters	0	0.5	0
Uncertainty regarding interfering species	0	0.2	0
Uncertainty regarding SZA	0.3	0.2	0.3
Total random error	0.8	1.8	0.5
Systematic errors			
Uncertainty regarding line intensity	3.3	3.2	7.4
Uncertainty regarding line width	0.7	0.2	1.0
Total random and systematic error	3.5	3.7	7.5
Smoothing error	0.4	1.6	6.9
Total error (random + systematic + smoothing)	3.5	4.0	10.2

Table 6.2: Error budget as a function of the different sources of random and systematic uncertainties for typical CO, C_2H_6, and CH_4 total columns retrieved at DAO. Format of Table based on Table 3 of [50]. Explanation of the various errors is detailed in §6.5.4

from the 48 layer VMR profile by integrating over the full altitude range and taking into account the density of the atmosphere at each layer. The averaging kernels (defined by the rows of $\mathbf{A}$ defined in Eq. 2.21) for our CO retrieval are presented in Fig. 6.11 and represent the sensitivity of our retrieval to the true state of the atmosphere. It is evident that all results from above 20 km are driven completely by our a priori data rather than our measurements. A muted secondary peak in the averaging kernels is evident at ∼8 km, and future refinement of the SFIT4 retrieval will hopefully allow us to once again calculate an upper-troposphere partial CO column.

The full time series of CO observations from the DAO is presented in the top panel of Fig. 6.12. Changing observing procedures led to significantly denser data coverage in 2013 and 2014, and less scatter is evident as we continued to identify and eliminate sources of noise in the system. A portion of the increased scatter evident during winter months can be explained by the turbulent air column described in §4.4. Gaps in the data set reflect periods of extended maintenance.

The seasonal trend of CO discussed in §2.1.1 is more easily identified by overlaying each calendar year's data plotted as a function of season. This is shown in the

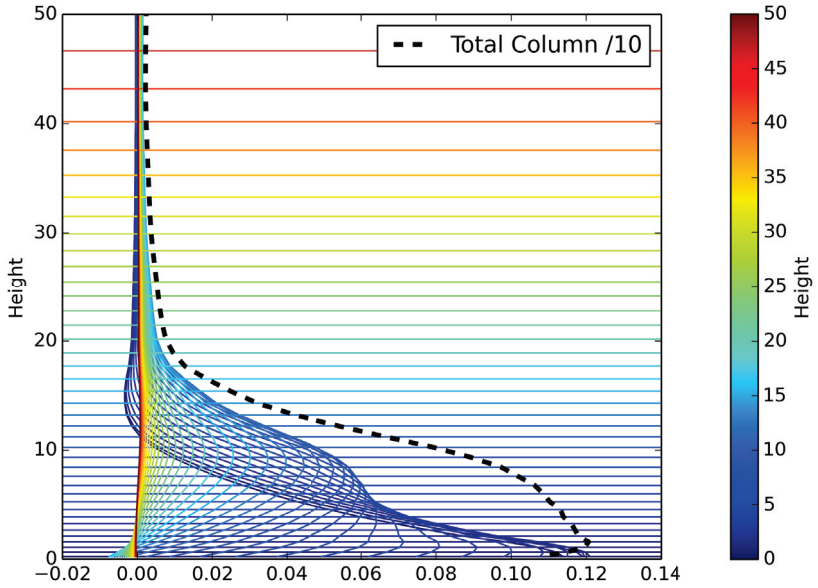

Figure 6.11: Typical layer VMR averaging kernels for DAO CO retrievals. Also shown is the total-column averaging kernel.

bottom panel of Fig. 6.12 where we can see the CO concentrations build during the winter months as chemical losses are reduced, only to decrease in the summer with the lengthening daylight hours. However, this expected pattern is interrupted in the DAO dataset by a strong second peak in late July and August. The strength of this summer enhancement varies from year to year with 2012 and 2014 showing sustained CO enhancements, while 2011 and 2013 only exhibit individual peaks of shorter duration. In §6.6 I will demonstrate that many of these enhancements are correlated with elevated abundances of fine-mode aerosols, and the airmasses can often be traced back to specific biomass burning events.

Comparison with PARIS CO columns

In §5.4 I quoted results of a comparison of total column CO values measured by PARIS and the DA8 during the 2011 BORTAS mission. This analysis was performed by Griffin et al. [45] using the SFIT2 retrieval software. The PARIS measurements from that campaign were recently processed using SFIT4 and in this section I will

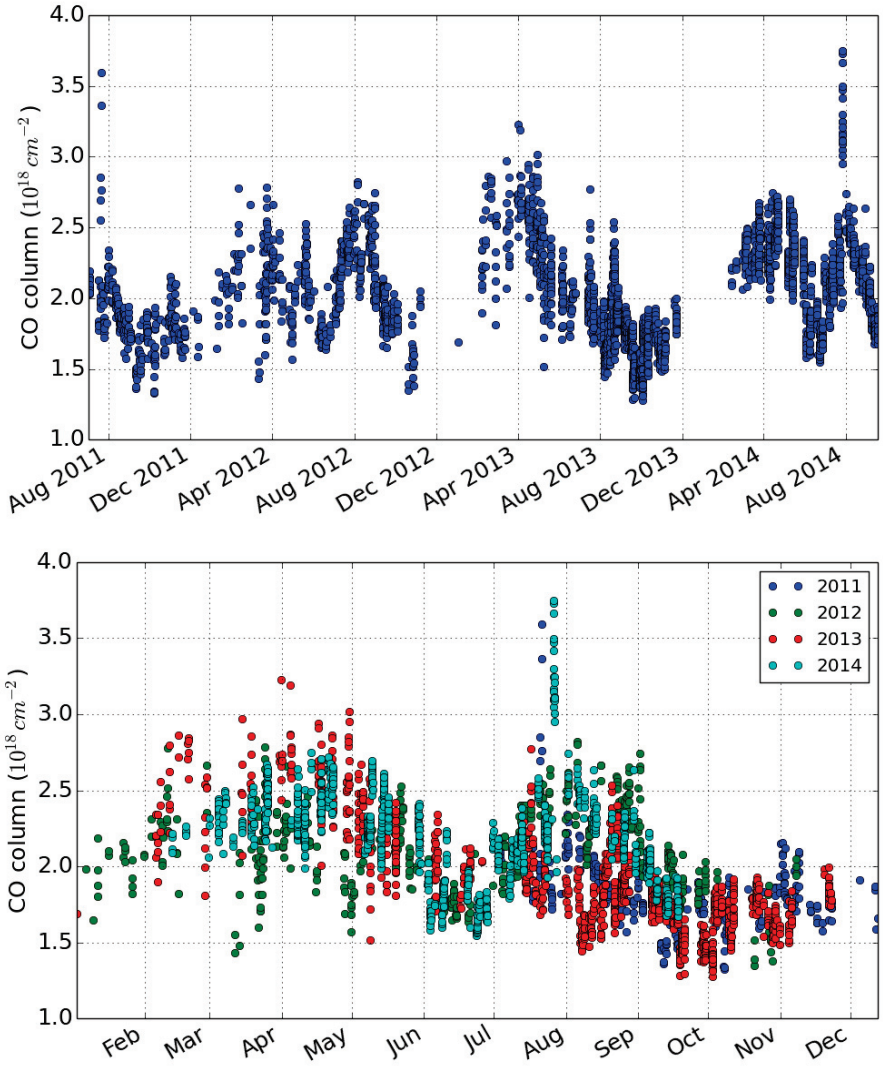

Figure 6.12: Top: Total column CO time series observed from the DAO from July 2011 to September 2014. Bottom: Seasonal cycle of total column CO observed from the DAO revealing significant summer time enhancements associated with long range transport.

revisit the comparison between the DAO-DA8 and PARIS retrievals during July and August 2011.

The lower spectral resolution of PARIS compared to the DAO-DA8 leads to differences in the CO averaging kernels of the two instruments. This difference must be considered when comparing the observed total columns. We begin by linearly interpolating the DAO-DA8 profile onto the lower resolution PARIS retrieval grid. The a priori CO profile is then subtracted from this interpolated DAO-DA8 profile before smoothing the result with the PARIS averaging kernel. In equation form this process can be written as:

$$\mathbf{x}_{\mathrm{sm}}^{\mathrm{DAO}} = \mathbf{x}_a + \mathbf{A}_{\mathrm{PARIS}} \cdot (\mathbf{x}_{\mathrm{intp}}^{\mathrm{DAO}} - \mathbf{x}_a). \tag{6.1}$$

A total of 103 pairs of coincident measurements were used (requiring $\Delta t < 10$ min) in our analysis. The mean relative difference between the two total-column CO values can be defined as [PARIS − DAO-DA8] / [0.5 · (PARIS + DAO-DA8)]. We calculate a relative difference of $1.1 \pm 3.5\%$ for the extended BORTAS campaign. Using SFIT2, Griffin et al. [45] found a mean relative difference of $-4.9 \pm 0.7\%$. These differences should be investigated further, but are within the uncertainty of the individual measurements. A correlation plot of the recent SFIT4 results is shown in Fig. 6.13.

6.5.2 Ethane

Ethane is retrieved at the DAO using relative uncertainties of 30% in the construction of $\mathbf{S}_a$. As with CO, we allow for correlations between different heights by assuming a Gaussian shaped covariance with a correlation length of 4 km. A typical averaging kernel plot for C_2H_6 is shown in Fig. 6.14. The total-column averaging kernel consists of a single broad peak centered on the upper troposphere, and we typically retrieve only 1.2 DOFS.

Figure 6.15 shows the full time series and seasonal cycle of total-column C_2H_6. Once again, a strong seasonal cycle is apparent, but additional enhancements are seen in the summer months that correspond to those seen in the CO time series. However, there is also additional scatter on many individual days that exceeds the ∼4% uncertainty listed in Table 6.2. This suggests the presence of additional

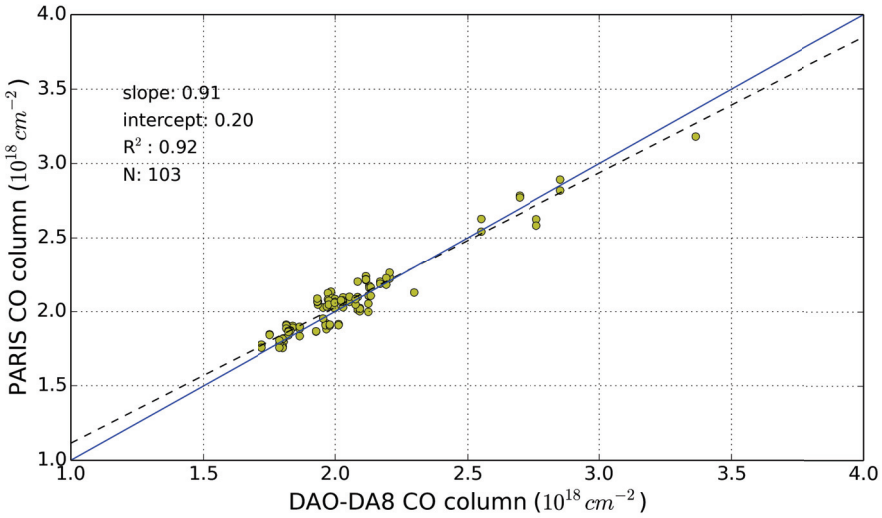

Figure 6.13: Comparision of SFIT4 total column CO retrievals by PARIS and DAO-DA8 during the extended BORTAS campaign during July and August 2011.

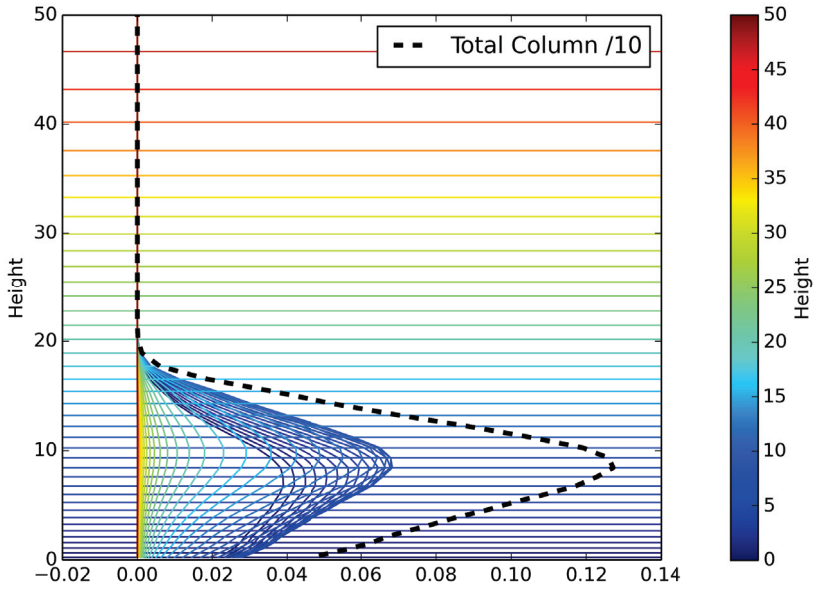

Figure 6.14: Typical layer VMR averaging kernels for DAO C_2H_6 retrievals. Also shown is the total-column averaging kernel.

systematic errors in the retrieval that are not currently being considered in our error analysis. A possible culprit is an additional airmass error caused by an offset between the CST and the DAO-DA8 as described in §4.5.

Three years of data is insufficient to quantify any long term trend in trace gas concentrations, but Fig. 6.15 appears to show a slight increase C_2H_6 over the limited data set. This trend has been recently reported by multiple members of the NDACC IRWG and a concerted effort to verify and quantify this trend was recently initiated at the 2015 annual IRWG meeting.

6.5.3 Methane

Our current retrievals of CH_4 are handled slightly differently than that of C_2H_6 and CO. The NDACC community recommends using a Tikhonov regularization method suggested by Sussmann et al. [87]. Tikhonov regularization differs from the ordinary least squares approach of OEM by adding a regularization term to the cost function being minimized:

$$||\mathbf{Fx} - \mathbf{y}||^2 + ||\mathbf{\Gamma x}||^2. \tag{6.2}$$

Here, $\mathbf{\Gamma}$ is the Tikhonov matrix that can be tuned to reduce the oscillations in the retrieved profiles [87].

At the DAO we attempted to use parameters already in use at the Toronto Atmospheric Observatory (TAO), and the results are shown in Fig. 6.16. The results are currently unsatisfactory and additional investigation is required to both minimize the channeling effects still present in the spectra and to continue systematically testing the retrieval parameters used. For example, our retrieval of CH_4 only produces $\sim$1.2 DOFS compared to 1.8 DOFS at TAO. It remains to be determined if the reduction in information content is caused by improper tuning parameters during the retrieval or are simply the result of systematic errors in the spectra.

6.5.4 Error analysis

A major advantage of SFIT4 over earlier versions of the retrieval software is the ability to easily perform the error analysis on a spectrum by spectrum basis. Different types of errors are considered in the SFIT4 analysis: measurement noise error, the smoothing error, and forward model parameter errors.

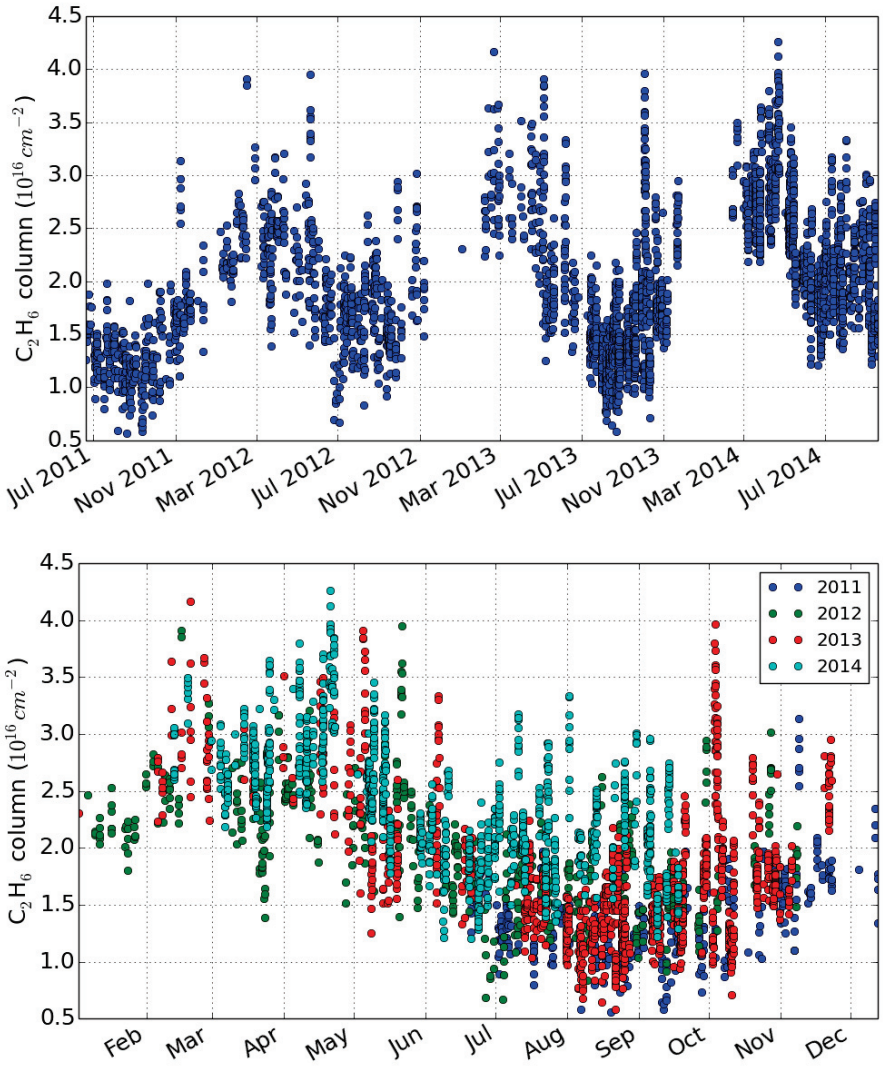

Figure 6.15: Top: Total column C_2H_6 time series observed from the DAO from July 2011 to September 2014. Bottom: Seasonal cycle of total column C_2H_6 observed from the DAO.

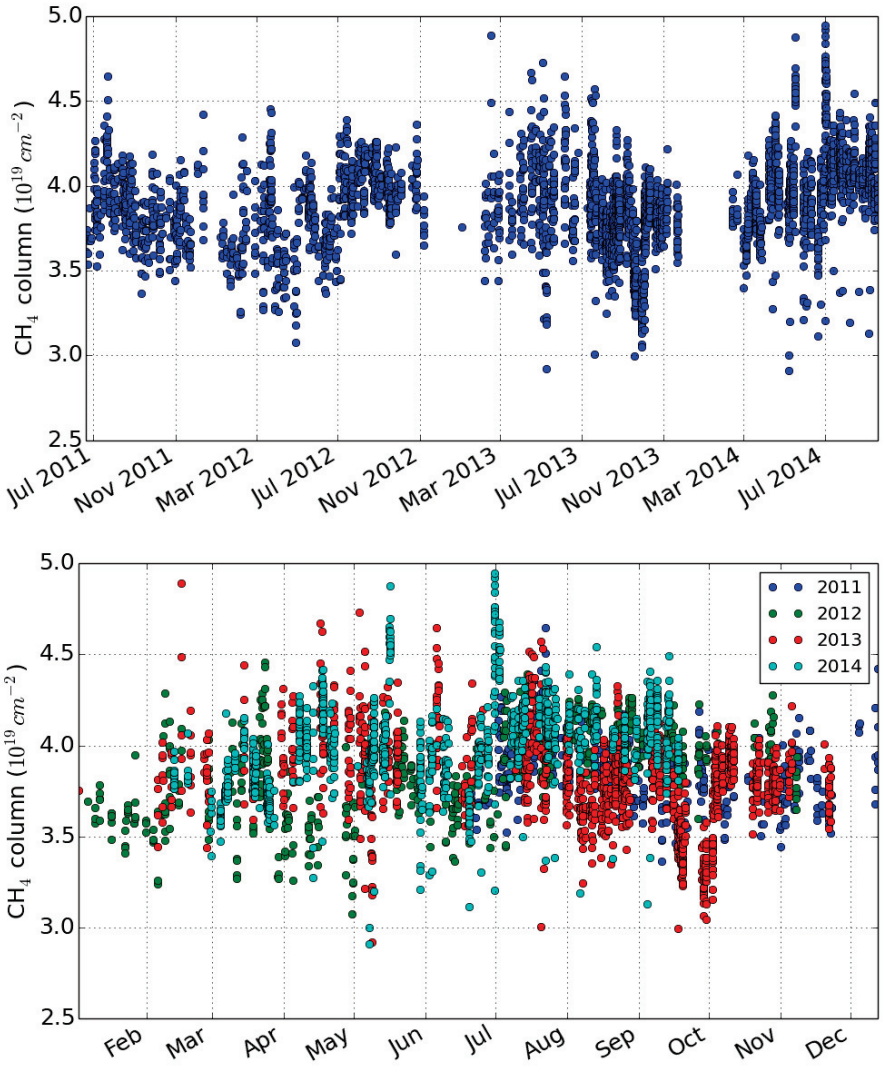

Figure 6.16: Top: Total column CH_4 time series observed from the DAO from July 2011 to September 2014. Bottom: Seasonal cycle of total column CH_4 observed from the DAO.

The measurement noise error is ideally a random error related to the SNR of the observed spectrum. The covariance in the measurement errors quantified by $\mathbf{S}_\varepsilon$ will propagate into the retrieval as

$$\mathbf{S}_m = \mathbf{G}\mathbf{S}_\varepsilon\mathbf{G}^{\mathrm{T}}, \tag{6.3}$$

where $\mathbf{G}$ is the gain matrix defined in Eq. 2.20. As SFIT4 calculates a SNR for each individual spectrum, this error may vary through a day of measurements and can become large when observing through large airmasses at high SZAs.

The smoothing error is caused by forcing the true continuous state of the atmosphere to a fixed retrieval grid. The covariance of this smoothing is given by

$$\mathbf{S}_s = (\mathbf{I} - \mathbf{A})\mathbf{S}_x(\mathbf{I} - \mathbf{A})^{\mathrm{T}}, \tag{6.4}$$

where $\mathbf{S}_x$ represents the variability of the target species. In our analysis we use the same values as for our a priori covariance matrix, $\mathbf{S}_a$.

The forward model parameter error can include contributions from any number of different parameters that are uncertain. Both systematic errors such as spectroscopic parameters, and random errors such as temperature profile uncertainties can be included in the covariance error matrix for model parameters, $\mathbf{S}_b$. We consider uncertainties related to spectroscopic line widths and strengths, temperature profiles, spectral interference from other species, and SZA values. These errors propagate to the final retrieval errors as

$$\mathbf{S}_f = (\mathbf{G}\mathbf{K}_b)\mathbf{S}_b(\mathbf{G}\mathbf{K}_b)^{\mathrm{T}}, \tag{6.5}$$

where $\mathbf{K}_b$ represents the sensitivity of the measurements to the various uncertain model parameters.

To produce the errors listed in Table 6.2 we averaged the values from a selection of different spectra representing measurements at different times of day and season. However, the example spectra were taken from measurements made during the final full year of measurements and likely underestimate the true errors from earlier in the dataset. A perturbation of 5% was used in the spectroscopic parameters, and a 0.2° uncertainty was added to the SZA. The temperature perturbation was determined by comparing NCEP temperatures to a year of radiosonde data from Yarmouth, NS. The total error listed in Table 6.2 is obtained by adding the individual errors in quadrature.

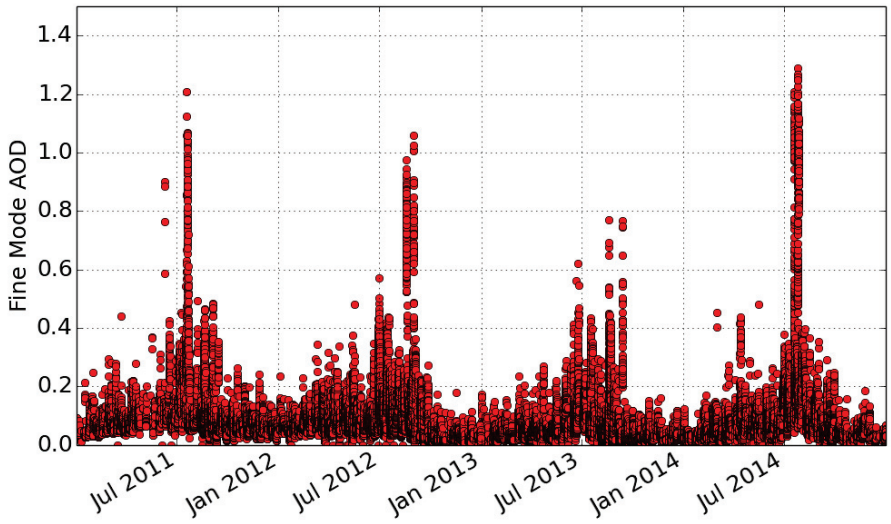

Figure 6.17: Fine mode AOD observed from the DAO from January 2011 through December 2014.

6.6 Discussion

The trace gas columns presented here represent only a preliminary analysis of the entire DAO-DA8 data set, but are sufficient to demonstrate that Halifax, NS, is well located to quantify the seasonal cycles of important trace gases. As the time series is expanded in coming years it will become possible to begin analyzing long term trends in trace gas concentrations. However, the current data set is sufficient to expand the long range transport investigation presented in Ch. 5. While a full analysis of every interesting airmass captured by the DAO is beyond the scope of this thesis, the broad summertime enhancements in CO (and sometimes C_2H_6) warrant further discussion.

With the exception of the precipitation-scavenged plume presented in Ch. 5, most enhancements in CO observed during the BORTAS mission were correlated with enhancements in fine mode aerosols [45]. The CIMEL sun photometer used in that study (and introduced in §5.3) has continued its observations of Aerosol Optical Depth (AOD) from the roof of the DAO as a part of the AEROCAN network [74]. In Fig. 6.17 I present the full time series of fine mode AOD observed during DAO-DA8 operations. These fine mode AOD values were derived from the post-calibrated level 1.0 AOD data set (at 500 nm) using the spectral deconvolution algorithm of O'Neill [6].

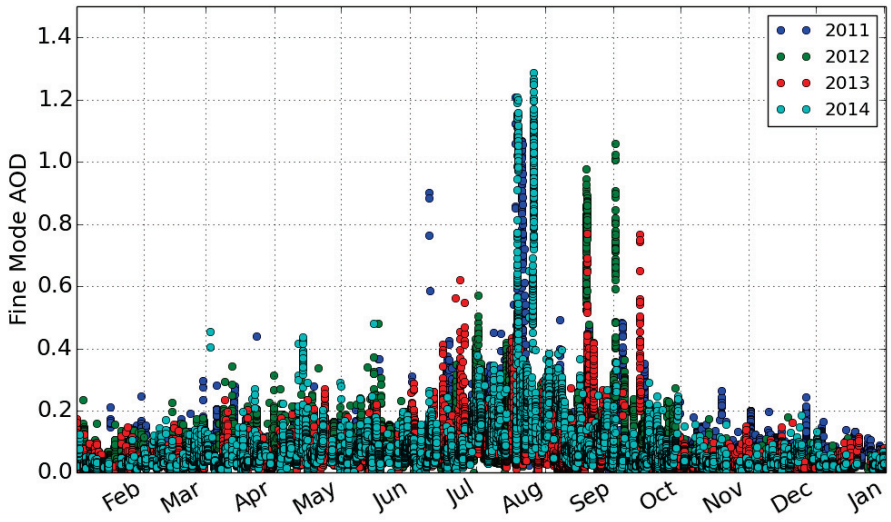

Figure 6.18: Seasonal plot of the fine mode AOD data shown in Fig. 6.17.

Most noticeable are the narrow sharp peaks associated with specific aerosol-heavy air masses, but there is also a broader seasonal enhancement that is more easily seen in Fig. 6.18. This seasonal pattern of fine mode AOD matches the pattern of summertime enhancements seen in the total-column CO measurements presented in Fig. 6.12.

The simultaneous enhancements of CO, C_2H_6, and fine mode aerosols strongly suggest that we are capturing the down stream effects of the powerful wildfires that seasonally ravage the northern boreal forest and western United States. This theory is supported by preliminary trajectory analyses performed on some of the largest enhancements. In the future our time series, once combined with data from other ground stations in eastern Canada, can help to further our understanding of the atmospheric impacts of these events.

Chapter 7

Conclusions

The primary objective of this work was to establish a high-resolution Fourier transform spectrometer at the Dalhousie Atmospheric Observatory to monitor trace gas concentrations above Halifax, Nova Scotia. This required the development of support instrumentation as well as the data processing software necessary to accurately gather and analyze solar absorption spectroscopic measurements. After undergoing an electronic upgrade, including the creation of new control software, the DAO-DA8 was installed during the spring of 2011 and achieved first light in June of that year. The new control software was developed with a focus on automation, and the resulting system requires only minimal user interaction to initiate a day of measurements. Regular solar measurements have continued since 2011 with only a few notable interruptions caused by temporary equipment failures. The initial years of measurements presented in this document will hopefully be the basis of future long-term studies of trace gas trends above the DAO.

Simultaneous with the spectrometer development we have created the Community Solar Tracker: a custom-built high-accuracy solar tracker used to provide the DAO-DA8 with a steady solar beam. The CST was designed as an open-source tracking platform that can be easily customized to suit the specific needs of other laboratories. The software for the CST blossomed during my involvement as I continued to add features, simplify its use, and improve its accuracy. The design is beginning to gain acceptance in the field and is already being actively used to support spectrometers in Toronto and as well as a station in the high Arctic where it will be used for lunar measurements during the polar winter. This has provided many opportunities for me to collaborate with the researchers in these labs and I continue to provide support for their use of the CST.

Through the process of developing and characterizing the CST we made the important discovery that the commonly used method of aligning the solar beam

entering a FTS by maximizing the signal at the detector does not necessarily result in perfect pointing. The remaining offset is a systematic issue that has likely been present for many years, but was hidden by the large scatter in previous tracking algorithms. Not only did we identify this issue, but we have demonstrated that the strong daily trend in solar line shifts resulting from this systematic offset in pointing can be used to quantify and correct the offset. We also presented a method to correct the data gathered prior to resolving the offset by identifying the true line of sight of the spectrometer through the atmosphere.

In an age when too many software packages are considered proprietary, we have developed a custom open-source data processing pipeline to convert our raw DAO-DA8 data into solar spectra that can be passed to the retrieval software SFIT4. Scans that pass an initial quality control check are phase corrected and Fourier transformed individually before being averaged. We showed that the processing software is sufficient to allow quality measurements of CO and C_2H_6. However, despite efforts to reduce the impact of channeling on the solar spectra, significant residual features have negatively impacted the CH_4 results presented. Future work is required to identify, and ideally remove, the source of the channeling, and further efforts are needed to correct the data previously gathered.

We have presented a preliminary analysis of the first three years of observations from the DAO. The switch of retrieval software (from SFIT2 to SFIT4) occurred in the final months of this work, and efforts to optimize the retrieval parameters with the new software will continue as this data is prepared for publication. While the Tikhonov regularization method of retrieving CH_4 has been adopted by many NDACC stations, our channeling difficulties may require the use of alternate microwindows and retrieval parameters.

The data set gathered at the DAO contains far more information than has been presented in this thesis, but even this initial exploration of the data set demonstrates that Halifax is a good site for the detection of long range transport events, including the seasonal biomass burning plumes from the boreal forest. We detected a broad summer time enhancement in CO columns that correlates with increased fine mode AOD, as well as a series of short-duration extreme events that will be studied in more detail.

Our work to support the BORTAS mission during the summer of 2011 demonstrated how we can use a variety of ground based observations to piece together the transport history of biomass burning plumes. The clustering of remote sensing instruments at the DAO enabled us to successfully identify a higher altitude plume of enhanced trace gases with low amounts of particulate matter that arrived prior to and overlapped with a lower altitude plume containing significant amounts of particles. The presence of this low-particulate concentration plume was verified by aircraft and satellite measurements; however, ground-based remote-sensing measurements were sufficient to detect this event. This work showed that, in order to adequately model the atmospheric impact of biomass burning events, it is critically important to understand the meteorological conditions along the trajectory and particularly in places where the plume changes altitude.

Having invested a significant amount of my time into this project I find it comforting to think of the legacy of this work. The data set to date is already being shared with researchers at the University of Toronto who are also investigating the influence of forest fires on the troposphere, and the data will be available to any other researchers investigating pollution transport. The tracking abilities of the CST will be expanded as we continue the process of replacing the older sun trackers at the Polar Environment Atmospheric Research Laboratory. And with the ongoing work to implement 24-bit uniform time sampling for the DAO-DA8, it is my hope that the three year data set presented in this thesis will be greatly extended and eventually become useful in quantifying long term trends in trace gas concentrations.

Bibliography

[1] P. Gonzalez, J. J. Battles, B. M. Collins, T. Robards, and D. S. Saah. Aboveground live carbon stock changes of California wildland ecosystems, 20012010. *Forest Ecology and Management*, 348:68 – 77, 2015. doi: 10.1016/j.foreco.2015.03.040.

[2] M. P. North, S. L. Stephens, B. M. Collins, J. K. Agee, G. Aplet, J. F. Franklin, and P. Z. Ful. Reform forest fire management. *Science*, 349(6254):1280–1281, 2015. doi: 10.1126/science.aab2356.

[3] A. Stohl and T. Trickl. A textbook example of long-range transport: Simultaneous observation of ozone maxima of stratospheric and North American origin in the free troposphere over Europe. *Journal of Geophysical Research*, 104 (D23):30445–30462, 1999. doi: 10.1029/1999JD900803.

[4] H. B. Singh, W. H. Brune, J. H. Crawford, D. J. Jacob, and P. B. Russell. Overview of the summer 2004 Intercontinental Chemical Transport ExperimentNorth America (INTEX-A). *Journal of Geophysical Research*, 111 (D24), December 2006. doi: 10.1029/2006JD007905.

[5] J. H. Seinfeld and S. N. Pandis. Atmospheric Chemistry and Physics: From Air Pollution to Climate Change. Second Edition. *Atmospheric Chemistry and Physics*, 2006.

[6] N. T. O'Neill. Spectral discrimination of coarse and fine mode optical depth. *Journal of Geophysical Research*, 108(D17):4559, 2003. doi: 10.1029/2002JD002975.

[7] D. M. Etheridge, L. P. Steele, R. J. Francey, and R. L. Langenfelds. Atmospheric methane between 1000 A.D. and present: Evidence of anthropogenic emissions and climatic variability. *Journal of Geophysical Research: Atmospheres*, 103 (D13):15979–15993, 1998. doi: 10.1029/98JD00923.

[8] E. J. Dlugokencky, E. G. Nisbet, R. Fisher, and D. Lowry. Global atmospheric methane: budget, changes and dangers. *Philosophical Transactions of the Royal Society of London A: Mathematical, Physical and Engineering Sciences*, 369 (1943):2058–2072, 2011. doi: 10.1098/rsta.2010.0341.

[9] M. Alexe, P. Bergamaschi, A. Segers, R. Detmers, A. Butz, O. Hasekamp, S. Guerlet, R. Parker, H. Boesch, C. Frankenberg, R. A. Scheepmaker, E. Dlugokencky, C. Sweeney, S. C. Wofsy, and E. A. Kort. Inverse modelling of CH_4 emissions for 2010 and 2011 using different satellite retrieval products from GOSAT and SCIAMACHY. *Atmospheric Chemistry and Physics*, 15(1): 113–133, 2015. doi: 10.5194/acp-15-113-2015.

[10] P. Ciais, C. Sabine, G. Bala, L. Bopp, V. Brovkin, J. Canadell, A. Chhabra, R. DeFries, J. Galloway, M. Heimann, C. Jones, C. LeQuere, R. B. Myneni, S. Piao, and P. Thornton. *Carbon and Other Biogeochemical Cycles*, book section 6. Cambridge University Press, Cambridge, United Kingdom and New York, NY, USA, 2013. ISBN 978-1-107-66182-0. doi: 10.1017/CBO9781107415324.015.

[11] M. J. Prather, C. D. Holmes, and J. Hsu. Reactive greenhouse gas scenarios: Systematic exploration of uncertainties and the role of atmospheric chemistry. *Geophysical Research Letters*, 39(9):L09803, 2012. doi: 10.1029/2012GL051440.

[12] J. Simpson, I, M. P. Sulbaek Andersen, S. Meinardi, L. Bruhwiler, N. J. Blake, D. Helmig, F. S. Rowland, and D. R. Blake. Long-term decline of global atmospheric ethane concentrations and implications for methane. *Nature*, 488 (7412):490–494, Aug 2012. doi: 10.1038/nature11342.

[13] Y. Xiao, J. A. Logan, D. J. Jacob, R. C. Hudman, R. Yantosca, and D. R. Blake. Global budget of ethane and regional constraints on U.S. sources. *Journal of Geophysical Research: Atmospheres*, 113(D21):D21306, 2008. doi: 10.1029/2007JD009415.

[14] J. Angelbratt, J. Mellqvist, D. Simpson, J. E. Jonson, T. Blumenstock, T. Borsdorff, P. Duchatelet, F. Forster, F. Hase, E. Mahieu, M. De Mazière, J. Notholt, A. K. Petersen, U. Raffalski, C. Servais, R. Sussmann, T. Warneke, and C. Vigouroux. Carbon monoxide (CO) and ethane (C_2H_6) trends from ground-based solar FTIR measurements at six European stations, comparison and sensitivity analysis with the EMEP model. *Atmospheric Chemistry and Physics*, 11(17):9253–9269, 2011. doi: 10.5194/acp-11-9253-2011.

[15] D. Ehhalt, M. Prather, F. Dentener, R. Derwent, E. Dlugokencky, E. Holland, I. Isaksen, J. Katima, V. Kirchhoff, P. Matson, P. Midgley, and M. Wang. *Atmospheric Chemistry and Greenhouse Gases*, book section 4, page 881pp. Cambridge University Press, Cambridge, United Kingdom and New York, NY, USA, 2001. ISBN 0521807670.

[16] M.O. Andreae and P. Merlet. Emission of trace gases and aerosols from biomass burning. *Global Biogeochemical Cycles*, 15(4):955–966, 2001.

[17] P. J. Crutzen and M. O. Andreae. Biomass burning in the tropics: impact on atmospheric chemistry and biogeochemical cycles. *Science (New York, N.Y.)*, 250(4988):1669–1678, December 1990. doi: 10.1126/science.250.4988.1669.

[18] H. Bremer, J. Kar, and J. R. Drummond. Spatial and temporal variation of MOPITT CO in Africa and South America: A comparison with SHADOZ ozone and MODIS aerosol. *Journal of Geophysical*, 109, 2004. doi: 10.1029/2003JD004234.

[19] F. T. Leung, J. A. Logan, R. Park, E. Hyer, E. Kasischke, D. Streets, and L. Yurganov. Impacts of enhanced biomass burning in the boreal forests in 1998 on tropospheric chemistry and the sensitivity of model results to the injection height of emissions. *Journal of Geophysical Research*, 112(D10):1–15, May 2007. doi: 10.1029/2006JD008132.

[20] G. Wotawa, P. C. Novelli, M. Trainer, and C. Granier. Inter-annual variability of summertime CO concentrations in the Northern Hemisphere explained by boreal forest fires in North America and Russia. *Geophysical Research Letters*, 28(24): 4575–4578, 2001.

[21] H. Huntrieser. Intercontinental air pollution transport from North America to Europe: Experimental evidence from airborne measurements and surface observations. *Journal of Geophysical Research*, 110(D1):1–22, 2005. doi: 10.1029/2004JD005045.

[22] D. Jaffe. Long-range transport of Siberian biomass burning emissions and impact on surface ozone in western North America. *Geophysical Research Letters*, 31(16), 2004. doi: 10.1029/2004GL020093.

[23] C. Forster, U. Wandinger, G. Wotawa, P. James, I. Mattis, D. Althausen, P. Simmonds, S. O'Doherty, S. G. Jennings, C. Kleefeld, J. Schneider, T. Trickl, S. Kreipl, H. Jäger, and A. Stohl. Transport of boreal forest fire emissions from Canada to Europe. *Journal of Geophysical Research*, 106(D19):22887–22906, 2001. doi: 10.1029/2001JD900115.

[24] D. J. Jacob, J. H. Crawford, H. Maring, A. D. Clarke, J. E. Dibb, L. K. Emmons, R. A. Ferrare, C. A. Hostetler, P. B. Russell, H. B. Singh, A. M. Thompson, G. E. Shaw, E. McCauley, J. R. Pederson, and J. A. Fisher. The Arctic Research of the Composition of the Troposphere from Aircraft and Satellites (ARCTAS) mission: design, execution, and first results. *Atmospheric Chemistry and Physics*, 10(11): 5191–5212, June 2010. doi: 10.5194/acp-10-5191-2010.

[25] M. Parrington, P. I. Palmer, D. K. Henze, D. W. Tarasick, E. J. Hyer, R. C. Owen, D. Helmig, C. Clerbaux, K. W. Bowman, M. N. Deeter, E. M. Barratt, P.-F. Coheur, D. Hurtmans, Z. Jiang, M. George, and J. R. Worden. The influence of boreal biomass burning emissions on the distribution of tropospheric ozone over North America and the North Atlantic during 2010. *Atmospheric Chemistry and Physics*, 12(4):2077–2098, 2012. doi: 10.5194/acp-12-2077-2012.

[26] P. I. Palmer, M. Parrington, J. D. Lee, A. C. Lewis, A. R. Rickard, P. F. Bernath, T. J. Duck, D. L. Waugh, D. W. Tarasick, S. Andrews, E. Aruffo, L. J. Bailey, E. Barrett, S. J.-B. Bauguitte, K. R. Curry, P. Di Carlo, L. Chisholm, L. Dan, G. Forster, J. E. Franklin, M. D. Gibson, D. Griffin, D. Helmig, J. R. Hopkins, J. T. Hopper, M. E. Jenkin, D. Kindred, J. Kliever, M. Le Breton, S. Matthiesen, M. Maurice, S. Moller, D. P. Moore, D. E. Oram, S. J. O'Shea, R. C. Owen, C. M. L. S. Pagniello, S. Pawson, C. J. Percival, J. R. Pierce, S. Punjabi, R. M. Purvis, J. J. Remedios, K. M. Rotermund, K. M. Sakamoto, A. M. da Silva, K. B. Strawbridge, K. Strong, J. Taylor, R. Trigwell, K. A. Tereszchuk, K. A. Walker, D. Weaver, C. Whaley, and J. C. Young. Quantifying the impact of BOReal forest fires on Tropospheric oxidants over the Atlantic using Aircraft and Satellites (BORTAS) experiment: design, execution and science overview. *Atmospheric Chemistry and Physics*, 13(13):6239–6261, 2013. doi: 10.5194/acp-13-6239-2013.

[27] M. D. Gibson, J. R. Pierce, D. Waugh, J. S. Kuchta, L. Chisholm, T. J. Duck, J. T. Hopper, S. Beauchamp, G. H. King, J. E. Franklin, W. R. Leaitch, a. J. Wheeler, Z. Li, G. a. Gagnon, and P. I. Palmer. Identifying the sources driving observed PM2.5 variability over Halifax, Nova Scotia, during BORTAS-B. *Atmospheric Chemistry and Physics Discussions*, 13(2):4491–4533, February 2013. doi: 10.5194/acpd-13-4491-2013.

[28] K. McKain, S. C. Wofsy, T. Nehrkorn, J. Eluszkiewicz, J. R. Ehleringer, and B. B. Stephens. Assessment of ground-based atmospheric observations for verification of greenhouse gas emissions from an urban region. *Proceedings of the National Academy of Sciences*, 109(22):8423–8428, 2012. doi: 10.1073/pnas.1116645109.

[29] K. N. Liou. *An Introduction to Atmospheric Radiation*. International Geophysics. Elsevier Science, 2002. ISBN 9780080491677.

[30] C. D. Rodgers. Retrieval of atmospheric temperature and composition from remote measurements of thermal radiation. *Reviews of Geophysics*, 14(4):609, 1976. doi: 10.1029/RG014i004p00609.

[31] C. D. Rodgers. *Inverse Methods for Atmospheric Sounding: Theory and Practice*. World Scientific Publishing Company, Incorporated, 2000. ISBN 981022740X.

[32] B. Barret, M. De Maziére, and P. Demoulin. Retrieval and characterization of ozone profiles from solar infrared spectra at the Jungfraujoch. *Journal of Geophysical Research: Atmospheres*, 107(D24):4788, 2002. doi: 10.1029/2001JD001298.

[33] P. Fellgett. A propos de la theorie du spectrometre interferential multiplex. *Journal of Physics Radium*, 19:187, 1958.

[34] R. J. Bell. *Introductory Fourier Transform Spectroscopy* . Academic Press ; New York, 1972. ISBN 0124314090.

[35] J. Chamberlain, G. W. Chantry, and N. W. B. Stone. *The principles of interferometric spectroscopy / John Chamberlain ; completed, collated, and edited by G. W. Chantry and N. W. B. Stone* . Wiley, Chichester [Eng.] ; New York, 1979. ISBN 0471997196.

[36] G. Keppel-Aleks, G. C. Toon, P. O. Wennberg, and N. M. Deutscher. Reducing the impact of source brightness fluctuations on spectra obtained by Fourier-transform spectrometry. *Applied Optics*, 46(21):4774–4779, Jul 2007. doi: 10.1364/AO.46.004774.

[37] M. L. Forman, W. H. Steel, and G. A. Vanasse. Correction of Asymmetric Interferograms Obtained in Fourier Spectroscopy. *J. Opt. Soc. Am.*, 56(1):59–61, Jan 1966. doi: 10.1364/JOSA.56.000059.

[38] F. Hase, T. Blumenstock, and C. Paton-Walsh. Analysis of the instrumental line shape of high-resolution Fourier transform IR spectrometers with gas cell measurements and new retrieval software. *Applied Optics*, 38(15):3417–3422, May 1999. doi: 10.1364/AO.38.003417.

[39] M. T. Coffey, A. Goldman, J. W. Hannigan, W.G. Mankin, W. G. Schoenfeld, C. P. Rinsland, C. Bernado, and D.W.T." Griffith. Improved vibration-rotation (0-1) HBr line parameters for validating high resolution infrared atmospheric spectra measurements. *Journal of Quantitative Spectroscopy and Radiative Transfer*, 60(5):863 – 867, 1998. doi: 10.1016/S0022-4073(98)00088-0.

[40] F. Kasten and A. T. Young. Revised optical air mass tables and approximation formula. *Applied Optics*, 28(22):4735–4738, Nov 1989. doi: 10.1364/AO.28.004735.

[41] D. Wunch, G. C. Toon, J.-F. L. Blavier, R. A. Washenfelder, J. Notholt, B. J. Connor, D. W. T. Griffith, V. Sherlock, and P. O. Wennberg. The Total Carbon Column Observing Network. *Philosophical Transactions of the Royal Society of London A: Mathematical, Physical and Engineering Sciences*, 369 (1943):2087–2112, 2011. doi: 10.1098/rsta.2010.0240.

[42] G. Toon, J.-F. Blavier, R. Washenfelder, D. Wunch, G. Keppel-Aleks, P. Wennberg, B. Connor, V. Sherlock, D. Griffith, N. Deutscher, and J. Notholt. Total Column Carbon Observing Network (TCCON). In *Advances in Imaging*, page JMA3. Optical Society of America, 2009. doi: 10.1364/FTS.2009.JMA3.

[43] A. Merlaud, M. De Maziére, C. Hermans, and A. Cornet. Equations for Solar Tracking. *Sensors*, 12(4):4074–4090, March 2012. doi: 10.3390/s120404074.

[44] M. Gisi, F. Hase, S. Dohe, and T. Blumenstock. Camtracker: a new camera controlled high precision solar tracker system for FTIR-spectrometers. *Atmospheric Measurement Techniques*, 4(1):47–54, 2011. doi: 10.5194/amt-4-47-2011.

[45] D. Griffin, K. A. Walker, J. E. Franklin, M. Parrington, C. Whaley, J. Hopper, J. R. Drummond, P. I. Palmer, K. Strong, T. J. Duck, I. Abboud, P. F. Bernath, C. Clerbaux, P.-F. Coheur, K. R. Curry, L. Dan, E. Hyer, J. Kliever, G. Lesins, M. Maurice, A. Saha, K. Tereszchuk, and D. Weaver. Investigation of CO, C_2H_6 and aerosols in a boreal fire plume over eastern Canada during BORTAS 2011 using ground- and satellite-based observations and model simulations. *Atmospheric Chemistry and Physics*, 13(20):10227–10241, 2013. doi: 10.5194/acp-13-10227-2013.

[46] J. E. Franklin, J. R. Drummond, D. Griffin, J. R. Pierce, D. L. Waugh, P. I. Palmer, M. Parrington, J. D. Lee, A. C. Lewis, A. R. Rickard, J. W. Taylor, J. D. Allan, H. Coe, K. A. Walker, L. Chisholm, T. J. Duck, J. T. Hopper, Y. Blanchard, M. D. Gibson, K. R. Curry, K. M. Sakamoto, G. Lesins, L. Dan, J. Kliever, and A. Saha. A case study of aerosol scavenging in a biomass burning plume over eastern Canada during the 2011 BORTAS field experiment. *Atmospheric Chemistry and Physics*, 14(16):8449–8460, 2014. doi: 10.5194/acp-14-8449-2014.

[47] P. Fogal, L. LeBlanc, and J. R. Drummond. The Polar Environment Atmospheric Research Laboratory (PEARL): Sounding the Atmosphere at 80 North. *ARCTIC*, 66(3), 2013.

[48] R. L. Batchelor, K. Strong, R. Lindenmaier, R. L. Mittermeier, H. Fast, J. R. Drummond, and P. F. Fogal. A New Bruker IFS 125HR FTIR Spectrometer for the Polar Environment Atmospheric Research Laboratory at Eureka, Nunavut, Canada: Measurements and Comparison with the Existing Bomem DA8 Spectrometer. *Journal of Atmospheric and Oceanic Technology*, 26(7):1328–1340, July 2009. doi: 10.1175/2009JTECHA1215.1.

[49] C. Viatte, K. Strong, C. Paton-Walsh, J. Mendonca, N. T. O'Neill, and J. R. Drummond. Measurements of CO, HCN, and C_2H_6 Total Columns in Smoke Plumes Transported from the 2010 Russian Boreal Forest Fires to the Canadian High Arctic. *Atmosphere-Ocean*, 51(5):522–531, 2013. doi: 10.1080/07055900.2013.823373.

[50] C. Viatte, K. Strong, K. A. Walker, and J. R. Drummond. Five years of CO, HCN, C_2H_6, C_2H_2, CH_3OH, HCOOH and H_2CO total columns measured in the Canadian high Arctic. *Atmospheric Measurement Techniques*, 7(6):1547–1570, 2014. doi: 10.5194/amt-7-1547-2014.

[51] G. Hönninger, C. von Friedeburg, and U. Platt. Multi axis differential optical absorption spectroscopy (MAX-DOAS). *Atmospheric Chemistry and Physics*, 4 (1):231–254, 2004. doi: 10.5194/acp-4-231-2004.

[52] A. Fraser, C. Adams, J. R. Drummond, F. Goutail, G. Manney, and K. Strong. The Polar Environment Atmospheric Research Laboratory UV-visible Ground-Based Spectrometer: First measurements of O_3, NO_2, BrO, and OClO columns. *Journal of Quantitative Spectroscopy and Radiative Transfer*, 110: 986–1004, August 2009. doi: 10.1016/j.jqsrt.2009.02.034.

[53] H. K. Roscoe, M. Van Roozendael, C. Fayt, A. du Piesanie, N. Abuhassan, C. Adams, M. Akrami, A. Cede, J. Chong, K. Clémer, U. Friess, M. Gil Ojeda, F. Goutail, R. Graves, A. Griesfeller, K. Grossmann, G. Hemerijckx, F. Hendrick, J. Herman, C. Hermans, H. Irie, P. V. Johnston, Y. Kanaya, K. Kreher, R. Leigh, A. Merlaud, G. H. Mount, M. Navarro, H. Oetjen, A. Pazmino, M. Perez-Camacho, E. Peters, G. Pinardi, O. Puentedura, A. Richter, A. Schönhardt, R. Shaiganfar, E. Spinei, K. Strong, H. Takashima, T. Vlemmix, M. Vrekoussis, T. Wagner, F. Wittrock, M. Yela, S. Yilmaz, F. Boersma, J. Hains, M. Kroon, A. Piters, and Y. J. Kim. Intercomparison of slant column measurements of NO_2 and O_4 by MAX-DOAS and zenith-sky UV and visible spectrometers. *Atmospheric Measurement Techniques*, 3(6):1629–1646, 2010. doi: 10.5194/amt-3-1629-2010.

[54] G. Pinardi, M. Van Roozendael, N. Abuhassan, C. Adams, A. Cede, K. Clémer, C. Fayt, U. Frieß, M. Gil, J. Herman, C. Hermans, F. Hendrick, H. Irie, A. Merlaud, M. Navarro Comas, E. Peters, A. J. M. Piters, O. Puentedura, A. Richter, A. Schönhardt, R. Shaiganfar, E. Spinei, K. Strong, H. Takashima, M. Vrekoussis, T. Wagner, F. Wittrock, and S. Yilmaz. MAX-DOAS formaldehyde slant column measurements during CINDI: intercomparison and analysis improvement. *Atmospheric Measurement Techniques*, 6(1):167–185, 2013. doi: 10.5194/amt-6-167-2013.

[55] C. Adams. *Measurements of Atmospheric Ozone, NO_2, OClO, and BrO at* 80° *N using UV-Visible Spectroscopy.* PhD thesis, University of Toronto, Toronto, Ontario, Canada, 2012.

[56] X. Zhao, K. Stong, C. Adams, R. Schofield, X. Yang, A. Richter, U. Friess, A. M. Blechschmidt, and J. H. Koo. A Case Study of a Transported Bromine Explosion Event in the Canadian High Arctic. *Journal of Geophysical Research, submitted.*, 2015.

[57] Toufic Hawat, Claude Camy-Peyret, and Roger Torguet. Suntracker for atmospheric remote sensing. *Optical Engineering*, 37(5):1633–1642, 1998. doi: 10.1117/1.601676.

[58] O. R. Cooper, J. L. Moody, D. D. Parrish, M. Trainer, J. S. Holloway, G. Hubler, F. C. Fehsenfeld, and A. Stohl. Trace gas composition of midlatitude cyclones over the western North Atlantic Ocean: A seasonal comparison of O_3 and CO. *Journal of Geophysical Research*, 107(D7):4057, 2002. doi: 10.1029/2001JD000902.

[59] R. G. Derwent, D. S. Stevenson, W. J. Collins, and C. E. Johnson. Intercontinental transport and the origins of the ozone observed at surface sites in Europe. *Atmospheric Environment*, 38(13):1891–1901, April 2004. doi: 10.1016/j.atmosenv.2004.01.008.

[60] N. Moteki, Y. Kondo, N. Oshima, N. Takegawa, M. Koike, K. Kita, H. Matsui, and M. Kajino. Size dependence of wet removal of black carbon aerosols during transport from the boundary layer to the free troposphere. *Geophysical Research Letters*, 39(13):L13802, July 2012. doi: 10.1029/2012GL052034.

[61] B. Croft, J. R. Pierce, R. V. Martin, C. Hoose, and U. Lohmann. Uncertainty associated with convective wet removal of entrained aerosols in a global climate model. *Atmospheric Chemistry and Physics*, 12(22):10725–10748, November 2012. doi: 10.5194/acp-12-10725-2012.

[62] J. Browse, K. S. Carslaw, S. R. Arnold, K. Pringle, and O. Boucher. The scavenging processes controlling the seasonal cycle in Arctic sulphate and black carbon aerosol. *Atmospheric Chemistry and Physics*, 12(15):6775–6798, August 2012. doi: 10.5194/acp-12-6775-2012.

[63] H. Matsui, Y. Kondo, N. Moteki, N. Takegawa, L. K. Sahu, Y. Zhao, H. E. Fuelberg, W. R. Sessions, G. Diskin, D. R. Blake, A. Wisthaler, and M. Koike. Seasonal variation of the transport of black carbon aerosol from the Asian continent to the Arctic during the ARCTAS aircraft campaign. *Journal of Geophysical Research*, 116(D5):D05202, March 2011. doi: 10.1029/2010JD015067.

[64] N. Oshima, Y. Kondo, N. Moteki, N. Takegawa, M. Koike, K. Kita, H. Matsui, M. Kajino, H. Nakamura, J. S. Jung, and Y. J. Kim. Wet removal of black carbon in Asian outflow: Aerosol Radiative Forcing in East Asia (A-FORCE) aircraft campaign. *Journal of Geophysical Research*, 117(D3):D03204, February 2012. doi: 10.1029/2011JD016552.

[65] M. O. Andreae, D. Rosenfeld, P. Artaxo, A. A. Costa, G. P. Frank, K. M. Longo, and M. A. F. Silva-Dias. Smoking Rain Clouds over the Amazon. *Science*, 303 (5662):1337–1342, 2004. doi: 10.1126/science.1092779.

[66] D. K. Davies, S. Ilavajhala, and C. O. Justice. Fire Information for Resource Management System: Archiving and Distributing MODIS Active Fire Data. *IEEE Transactions on Geoscience and Remote Sensing*, 47(1):72–79, January 2009. doi: 10.1109/TGRS.2008.2002076.

[67] L. Giglio, J. Descloitres, C. O. Justice, and Y. J. Kaufman. An Enhanced Contextual Fire Detection Algorithm for MODIS. *Remote Sensing of Environment*, 87(2):273–282, 2003.

[68] D. Fu, K. A. Walker, K. Sung, C. D. Boone, M. Soucy, and P. F. Bernath. The portable atmospheric research interferometric spectrometer for the infrared, PARIS-IR. *Journal of Quantitative Spectroscopy and Radiative Transfer*, 103(2): 362–370, January 2007. doi: 10.1016/j.jqsrt.2006.05.006.

[69] P. F. Bernath, C. T. McElroy, M. C. Abrams, C. D. Boone, M. Butler, C. Camy-Peyret, M. Carleer, C. Clerbaux, P.-F. Coheur, R. Colin, P. DeCola, M. DeMazire, J. R. Drummond, D. Dufour, W. F. J. Evans, H. Fast, D. Fussen, K. Gilbert, D. E. Jennings, E. J. Llewellyn, R. P. Lowe, E. Mahieu, J. C. McConnell, M. McHugh, S. D. McLeod, R. Michaud, C. Midwinter, R. Nassar, F. Nichitiu, C. Nowlan, C. P. Rinsland, Y. J. Rochon, N. Rowlands, K. Semeniuk, P. Simon, R. Skelton, J. J. Sloan, M.-A. Soucy, K. Strong, P. Tremblay, D. Turnbull, K. A. Walker, I. Walkty, D. A. Wardle, V. Wehrle, R. Zander, and J. Zou. Atmospheric Chemistry Experiment (ACE): Mission overview. *Geophysical Research Letters*, 32(15), 2005. doi: 10.1029/2005GL022386.

[70] N. S. Pougatchev, B. J. Connor, and C. P. Rinsland. Infrared measurements of the ozone vertical distribution above Kitt Peak. *Journal of Geophysical Research*, 100(D8):16689, 1995. doi: 10.1029/95JD01296.

[71] N. S. Pougatchev, B. J. Connor, N. B. Jones, and C. P. Rinsland. Validation of ozone profile retrievals from infrared ground-based solar spectra. *Geophysical Research Letters*, 23(13):1637–1640, June 1996. doi: 10.1029/96GL01501.

[72] L. S. Rothman, L. R. Brown, J. V. Auwera, L. S. Rothman, I. E. Gordon, A. Barbe, D. C. Benner, P. F. Bernath, M. Birk, V. Boudon, L. R. Brown, A. Campargue, J. P. Champion, K. Chance, L. H. Coudert, V. Dana, V. M. Devi, S. Fally, J. M. Flaud, R. R. Gamache, A. Goldman, D. Jacquemart, I. Kleiner, N. Lacome, W. J. Lafferty, J. Y. Mandin, S. T. Massie, S. N. Mikhailenko, C. E. Miller, N. Moazzen-Ahmadi, O. V. Naumenko, A. V. Nikitin, J. Orphal, V. I. Perevalov, A. Perrin, A. Predoi-Cross, C. P. Rinsland, M. Rotger, M. Šimečková, M. A. H. Smith, K. Sung, S. A. Tashkun, J. Tennyson, R. A. Toth, A. C. Vandaele, and J. Vander Auwera. The HITRAN 2008 molecular spectroscopic database. *Journal of Quantitative Spectroscopy and Radiative Transfer*, 110(9): 533–572, 2009.

[73] V. Eyring, D. W. Waugh, G. E. Bodeker, E. Cordero, H. Akiyoshi, J. Austin, S. R. Beagley, B. a. Boville, P. Braesicke, C. Brühl, N. Butchart, M. P. Chipperfield, M. Dameris, R. Deckert, M. Deushi, S. M. Frith, R. R. Garcia, a. Gettelman, M. a. Giorgetta, D. E. Kinnison, E. Mancini, E. Manzini, D. R. Marsh, S. Matthes, T. Nagashima, P. a. Newman, J. E. Nielsen, S. Pawson, G. Pitari, D. a. Plummer, E. Rozanov, M. Schraner, J. F. Scinocca, K. Semeniuk, T. G. Shepherd, K. Shibata, B. Steil, R. S. Stolarski, W. Tian, and M. Yoshiki. Multimodel projections of stratospheric ozone in the 21st century. *Journal of Geophysical Research*, 112(D16):D16303, August 2007. doi: 10.1029/2006JD008332.

[74] B. N. Holben, T. F. Eck, I. Slutsker, D. Tanre, J. P. Buis, A. Setzer, E. Vermote, J. A. Reagan, Y. J. Kaufman, T. Nakajima, F. Lavenu, I. Jankowiak, and A. Smirnov. AERONETA federated instrument network and data archive for aerosol characterization. *Remote sensing of Environment*, 66(1):1 – 16, 1998.

[75] A. Herber. Continuous day and night aerosol optical depth observations in the Arctic between 1991 and 1999. *Journal of Geophysical Research*, 107(D10):4097, 2002. doi: 10.1029/2001JD000536.

[76] L. Bitar, T. J. Duck, N. I. Kristiansen, A. Stohl, and S. Beauchamp. Lidar observations of Kasatochi volcano aerosols in the troposphere and stratosphere. *Journal of Geophysical Research*, 115:D00L13, October 2010. doi: 10.1029/2009JD013650.

[77] J. T. Jayne, D. C. Leard, X. Zhang, P. Davidovits, K. A. Smith, C. E. Kolb, and D. R. Worsnop. Development of an Aerosol Mass Spectrometer for Size and Composition Analysis of Submicron Particles. *Aerosol Science and Technology*, 33(1-2):49–70, July 2000. doi: 10.1080/027868200410840.

[78] C. Gerbig, S. Schmitgen, D. Kley, A. Volz-Thomas, K. Dewey, and D. Haaks. An improved fast-response vacuum-UV resonance fluorescence CO instrument. *Journal of Geophysical Research*, 104(D1):1699, January 1999. doi: 10.1029/1998JD100031.

[79] J. W. Taylor, J. D. Allan, G. Allen, H. Coe, P. I. Williams, M. J. Flynn, M. Le Breton, J. B. A. Muller, C. J. Percival, D. Oram, G. Forster, J. D. Lee, A. R. Rickard, M. Parrington, and P. I. Palmer. Size-dependent wet removal of black carbon in Canadian biomass burning plumes. *Atmospheric Chemistry and Physics*, 14(24):13755–13771, 2014. doi: 10.5194/acp-14-13755-2014.

[80] R. R. Draxler and G. D. Rolph. HYSPLIT (HYbrid Single-Particle Lagrangian Integrated Trajectory) Model access via NOAA ARL READY Website (http://ready.arl.noaa.gov/HYSPLIT.php). NOAA Air Resources Laboratory, Silver Spring, MD., 2013.

[81] G. D. Rolph. Real-time Environmental Applications and Display sYstem (READY) Website (http://ready.arl.noaa.gov). NOAA Air Resources Laboratory, Silver Spring, MD., 2013.

[82] A. Stohl, C. Forster, A. Frank, P. Seibert, and G. Wotawa. Technical note: The Lagrangian particle dispersion model FLEXPART version 6.2. *Atmospheric Chemistry and Physics*, 5(9):2461–2474, September 2005. doi: 10.5194/acp-5-2461-2005.

[83] W. W. McMillan, J. X. Warner, M. McCourt Comer, E. Maddy, A. Chu, L. Sparling, E. Eloranta, R. Hoff, G. Sachse, C. Barnet, I. Razenkov, and W. Wolf. AIRS views transport from 12 to 22 July 2004 Alaskan/Canadian fires: Correlation of AIRS CO and MODIS AOD with forward trajectories and comparison of AIRS CO retrievals with DC-8 in situ measurements during INTEX-A/ICARTT. *Journal of Geophysical Research*, 113(D20):D20301, October 2008. doi: 10.1029/2007JD009711.

[84] W. R. Burrows, P. King, P. J. Lewis, B. Kochtubajda, B. Snyder, and V. Turcotte. Lightning occurrence patterns over Canada and adjacent United States from lightning detection network observations. *Atmosphere-Ocean*, 40(1): 59–80, March 2002. doi: 10.3137/ao.400104.

[85] F. Hase, J. W. Hannigan, M. T. Coffey, A. Goldman, M. Höpfner, N. B. Jones, C. P. Rinsland, and S. W. Wood. Intercomparison of retrieval codes used for the analysis of high-resolution, ground-based FTIR measurements. *Journal of Quantitative Spectroscopy and Radiative Transfer*, 87(1):25 – 52, 2004. doi: 10.1016/j.jqsrt.2003.12.008.

[86] C. Clerbaux, M. George, S. Turquety, K. A. Walker, B. Barret, P. Bernath, C. Boone, T. Borsdorff, J. P. Cammas, V. Catoire, M. Coffey, P.-F. Coheur, M. Deeter, M. De Mazière, J. Drummond, P. Duchatelet, E. Dupuy, R. de Zafra, F. Eddounia, D. P. Edwards, L. Emmons, B. Funke, J. Gille, D. W. T. Griffith, J. Hannigan, F. Hase, M. Höpfner, N. Jones, A. Kagawa, Y. Kasai, I. Kramer, E. Le Flochmoën, N. J. Livesey, M. López-Puertas, M. Luo, E. Mahieu, D. Murtagh, P. Nédélec, A. Pazmino, H. Pumphrey, P. Ricaud, C. P. Rinsland, C. Robert, M. Schneider, C. Senten, G. Stiller, A. Strandberg, K. Strong, R. Sussmann, V. Thouret, J. Urban, and A. Wiacek. CO measurements from the ACE-FTS satellite instrument: data analysis and validation using ground-based, airborne and spaceborne observations. *Atmospheric Chemistry and Physics*, 8 (9):2569–2594, 2008. doi: 10.5194/acp-8-2569-2008.

[87] R. Sussmann, F. Forster, M. Rettinger, and N. Jones. Strategy for high-accuracy-and-precision retrieval of atmospheric methane from the mid-infrared FTIR network. *Atmospheric Measurement Techniques*, 4(9): 1943–1964, 2011. doi: 10.5194/amt-4-1943-2011.

Appendix A

Copyright Information

Chapter 5 of this thesis contains an article published in the Journal of Atmospheric Chemistry and Physics. The author retains the copyright for this publication. Further information can be found at `http://www.atmospheric-chemistry-and-physics.net/about/licence_and_copyright.html`, which states:

License and Copyright Agreement

The following licence and copyright agreement is valid for any article published by Copernicus Publications on behalf of the European Geosciences Union (EGU) in the journal Atmospheric Chemistry and Physics and its discussion forum Atmospheric Chemistry and Physics Discussions.

Author's Certification

By submitting the manuscript, the authors certify the following:

- They are authorized by their co-authors to enter into these arrangements.
- The work described has not been published before (except in the form of an abstract or proceedings-type publication including discussion papers or as part of a published lecture or thesis); it is not under consideration for publication elsewhere; and its publication has been approved by all the author(s) and by the responsible authorities tacitly or explicitly of the institutes where the work was carried out.
- They have secured the right to reproduce any material that has already been published or copyrighted elsewhere.
- They have agreed to the licence and copyright agreement mentioned above.

Copyright

- The copyright of any article is retained by the author(s). More information on the transfer of copyright can be found below.

- Authors grant Copernicus Publications a licence to publish the article and identify itself as the original publisher.
- Authors grant Copernicus Publications commercial rights to produce hardcopy volumes of the journal for purchase by libraries and individuals.
- Authors grant any third party the right to use the article freely under the stipulation that the original authors are given credit and the appropriate citation details are mentioned.
- The article is distributed under the Creative Commons Attribution 3.0 License. Unless otherwise stated, associated published material is distributed under the same licence.

Copyright Transfers

Many authors have strict regulations in their employment contract regarding their publications. A transfer of copyright to the institution or company is common as well as the reservation of specific usage rights. In open-access publications in combination with the Creative Commons License, a transfer of the copyright to the institution is possible as it belongs to the author anyway.

Any usage rights are regulated through the Creative Commons License. As Copernicus Publications uses the Creative Commons Attribution 3.0 License, anyone (the author, his/her institution/company, the publisher, as well as the public) is free to copy, distribute, transmit, and adapt the work as long as the original author is given credit (see above). Therefore, specific usage rights cannot be reserved by the author or his/her institution/company, and the publisher cannot include the statement "all rights reserved" in any published paper.

A copyright transfer from the author to his/her institution/company can be expressed in a special "copyright statement" at the end of the publication. Authors are asked to include the following sentence: "The author's copyright for this publication has been transferred to institution/company".